Novel Components for Integrated Millimeter-Wave Front-Ends

by

Abbas Abbaspour-Tamijani

A dissertation submitted in partial fulfillment
of the requirements for the degree of
Doctor of Philosophy
(Electrical Engineering)
in The University of Michigan
2004

Doctoral Committee:
  Professor Gabriel M. Rebeiz, Chair
  Professor Kamal Sarabandi, Co-Chair
  Associate Professor Brian Gilchrist
  Associate Professor Amir Mortazawi
  Associate Professor Kim Winick

To my father Mohammad-Hossein,

and in the loving memory of my mother Nassrin.

ACKNOWLEDGEMENTS

For a real student, education never ends. At least that is the hope. Nevertheless, after nearly a quarter of a century of being “in school”, now I finally find myself at the end of my formal course of education. Although it is too soon to feel the relief, I have already started to feel the void. So my acknowledgement, which is naturally my last stage of thesis writing, is filled with an air of nostalgia. The acknowledgement for a Ph.D. thesis, I believe, must be an acknowledgement to ones entire career of studentship. However, the endless number of people who have been involved in my education during the years makes it impossible to carry out a fair task. So I limit my list to those who have been directly engaged in the last part, namely my years at the University of Michigan.

Among all who have contributed to my post graduate education, my greatest appreciation surely belongs to Professors Gabriel M. Rebeiz and Kamal Sarabandi, who guided me through the Ph.D. program. I especially would like to thank Professor Rebeiz, because of whom I decided to come to Michigan in the first place, a decision that I never regret. During the years of working with him, I learnt a great deal both about technical issues and about the ethics of research. His dedication to quality is one thing that I hope I never forget. Also his trust and support which let me work and learn in my own unconventional ways and yet his help to make me a better researcher was highly precious in my education. I also would like to thank Professor Sarabandi for his infinite support during the past years. He has been a true friend and an outstanding teacher. His broad knowledge and inexhaustible research ideas have inspired many parts of my doctoral work. Working with these two men, made my last years a priceless experience.

There is a long list of colleagues who helped me in different stages of my work. Most of all, I would like to thank my very good friend, Dr. Laurent Dussopt, whose help was crucial to parts of my research. I enjoyed working with him and learnt many hands-on skills from him. My dependence on his assistance was so profound that it was only after he left that I finally came to learn the magic of microfabrication. For this matter, two other friends of mine, Mr. Bernhard Schoenlinner and Tauno Vaha-Heikkila, are to be recognized for their magnificent job of mentorship. What a demonstration of will and resilience it must have been to train an old-school electromagnetician to perform complicated microfabrication routines! In a similar context, I should to thank my friends Mr. Timothy Hancock and Michael Chang for their round the clock support when I was helpless against the monstrosities of my desktop computer.

I also would like to thank all my friends with whom my relationship expands beyond the circle of professional acquaintances. Specially thanks to my very good friend, Dr. Jose Cabanillas, with whom I spent numerous coffee hours and yet we never ran out of conversation topics. My special thanks also to my other good friend Dr. Jad Rizk who was the third and recently the remote corner of our coffee-talk triangle[1]. I also would like to thank my old friend Mr. Farshid Aryanfar, with whom my memories date back to the years before coming to Michigan. Also my gratitude to all my other friends in the Radiation Laboratory and EECS department, my friends in the ballroom dance club, and my Iranian friends in Ann Arbor, who made my stay in Michigan enjoyable.

My acknowledgement will not be complete without mentioning the staff members of the Radiation Laboratory and EECS department for their dedication and for their

---

[1] For future reference, it would not be entirely irrelevant if I also mentioned the names of two most popular Ann Arbor coffee-shops: Sweetwaters and Starbucks in the State Street, for their excellent ambience!

assistance through the past years. My special thanks go to Mrs. Susan Charnley and Ms. Karla Johnson.

Finally, I would like to thank those who have provided me with emotional support during the past years. This includes Miss Frederique de Lame, whose lovely presence was my most precious asset in the final and hardest year of my Ph.D., and my family in Iran, whose unconditional love and support has lit my way through the life. Specially, I thank my father Mohammd-Hossein and my late mother Nassrin, who were my first teachers and their love and encouragement inspired my passion for learning. It is to commemorate their love that I dedicate this thesis to them.

A. Abbaspour-Tamijani
Ann Arbor, Michigan
December 4 2003

TABLE OF CONTENTS

DEDICATION ii

ACKNOWLEDGEMENTS iii

LIST OF TABLES ix

LIST OF FIGURES xi

LIST OF APPENDICES xv

CHAPTERS

1 Introduction 1
  1.1 Thesis Overview 3

2 Interleaved-Subarray Antennas for Millimeter-Wave Applications . . 7
  2.1 Introduction 7
  2.2 Grouping and Two-fold Array Theory 9
  2.3 Overlapping Condition and Interleaved Subarrays 11
  2.4 Array Design 15
  2.5 Implementation Challenges 16
  2.6 A Planar Implementation of The Interleaved Subarrays . . . 19
  2.7 Offset Subarray Constellation 21
  2.8 Resonant Feed Networks 23
  2.9 Experimental Results 27
  2.10 Conclusion 30

3 MEMS Tunable Filters 33
  3.1 Introduction 33
  3.2 Tapped and Distributed Loading of Transmission-Line Resonators 34
  3.3 Design Equations for the Loaded Resonators 37
    3.3.1 Open-Ended Resonator with Tapped Loading 38
    3.3.2 Short-Ended Resonator with Tapped Loading 39
    3.3.3 Short-Ended Resonator with Distributed Loading . . 39

3.4 Bandpass Filters and Inverter Design 40
3.5 MEMS Tunable Filters with Tapped Varactor Loading 43
  3.5.1 Filters with Capacitive Inverters 43
  3.5.2 Filters with Inductive Inverters 51
3.6 Distributed Designs 55
  3.6.1 Slow-Wave MEMS Resonator 55
  3.6.2 MEMS Miniature Filter 57
  3.6.3 Miniature-Tunable K-Band Filter 61
3.7 Nonlinear Characterization 67

67

  3.7.2 Miniature-Tunable Filter 69
3.8 Conclusion 71

4 Antenna-Filter-Antenna Arrays As A Class of Bandpass Frequency-Selective-Surfaces 73
  4.1 Introduction 73
  4.2 Antenna-Filter-Antenna Concept 74
  4.3 Design of AFA Modules 76
    4.3.1 Basic Design Concerns 77
    4.3.2 Type-I AFA: 3-Pole Chebyshev Bandpass 78
    4.3.3 Type-II AFA: 3-Pole Bandpass with Transmission Zeroes 81
    4.3.4 Type-III AFA: 4-Pole Chebyshev Bandpass 84
  4.4 AFA-Based Frequency-Selective Surfaces 86
    4.4.1 Effect of The Cell Size on Frequency Response 86
    4.4.2 Surface-Waves and Operation at Oblique Incidence . . 88
  4.5 Finite Element Simulation 90
  4.6 Fabrication 92
  4.7 Measurement Method 94
  4.8 Experimental Results 96
  4.9 Conclusion 99

5 Filter-Lens Arrays 101
  5.1 Introduction 101
  5.2 Wave Transformation Using An Array of Scaled AFA's 102
  5.3 Phase Response of The Type-I and Type-II AFA's 104
  5.4 FLA Design 107
  5.5 Analysis 111
  5.6 Measurement Method 115
    5.6.1 Pattern 115
    5.6.2 Gain 117
    5.6.3 Gain-Response 119
  5.7 Results 120
  5.8 Conclusion 128

6 Conclusion 130

APPENDICES 135

BIBLIOGRAPHY 156

LIST OF TABLES

Table

2.1 Parameters of the primary and secondary arrays. 16
2.2 Measured Data for the Primary Array. 28
2.3 Measured Data for the Primary Array. 32
3.1 Chebyshev filter coefficients for a 3-pole response with 0.05 dB pass-band ripple. 44
3.2 Model parameters for the 21.7-24.0 GHz 3-pole tunable filter. 46
3.3 Measured parameters of the capacitively-coupled tunable 3-pole filter. . . 50
3.4 Model parameters for the 22.9-25.1 GHz 3-pole filter with a tunable bandwidth of 1.3 GHz. 53
3.5 Simulated parameters of the inductively-coupled 3-pole filter with a 1.3 GHz tunable bandwidth using ideal varactors and a transmission-line Q of 90 at 24 GHz. 53
3.6 Measured parameters of the standard and loaded transmission-line resonators. No bias lines presnt in this structure. 57
3.7 Model parameters for the 21 GHz miniature 8% 3-pole filter with 6-bridge loading per resonator. 59
3.8 Measured parameters of the MEMS miniature filters. 60
3.9 Simulated pass-band parameters of the MEMS miniature filter for different bridge heights. 61
3.10 Measured parameters of The MEMS Slow-Wave Resonator for different bias voltages. 63
3.11 Measured parameters of the miniature tunable filter for different values of bias voltage. 66
4.1 Model parameters for the Type-I AFA at 35 GHz. 80
4.2 Model parameters for the Type-II AFA at 35 GHz. 83
4.3 Model parameters for the Type-III AFA at 35 GHz. 85
5.1 Measured pass-band parameters of the Type-I and Type-II AFA's. 107
5.2 Radiation performance data for the FLA at 35 GHz. 124
5.3 Filtering performance data of the FLA. 124
5.4 Scanning performance data of the FLA at 35 GHz. 129

A-1 Iterative design of an example resonant section. 137
B-1 Simulated and measured inductance for two test structures. 142
C-1 Model parameters for the capacitively-loaded switched-band filter at 35 GHz. 145
C-2 Model parameters for the inductively-loaded switched-band filter at 36.4 GHz. 148

LIST OF FIGURES

Figure

2.1 Grouping of the elements in a phased array. 9

2.2 Array factor multiplication in the grouped arrays. Horizontal axes represents the angle variable u (see equation .2.5): (a) primary array factor, (b) secondary array factor, (c) overall array factor before scanning, and (d) overall array factor after scanning. All array factors are assumed ideal. . . 10

2.3 Partially-overlapped subarrays in a linear arrangement. 14

2.4 Interleaved subarrays in a linear arrangement. 15

2.5 Synthesized array factors vs. the array polar angle γ; a) primary, b) secondary. 17

2.6 Radiation pattern of the combined array vs. the array polar angle γ; a) without scanning, b) with +7 degs. scanning. 18

2.7 Simplified layout of the 80 element array; different subarrays are shown in different gray levels. 20

2.8 Subarray layout; (a) antenna layer, (b) feed layer. 21

2.9 Layout of the two-layer phased array; (a) antenna layer, (b) feed layer. . . 22

2.10 Mutual coupling between two adjacent patch antennas vs. vertical offset. . 23

2.11 Patch elements connected using a two-part transmission-line feed section. . 25

2.12 The X-band prototype of the 80-element array. 28

2.13 Measured and simulated radiation patterns for a subarray; a) horizontal plane, b) vertical plane. 29

2.14 Measured and simulated radiation patterns of the full array in the horizontal plane; top: boresight beam position, bottom: squint beam position. 31

2.15 Measured S_{11} vs. frequency in the boresight and squint beam positions. . . 32

3.1 MEMS varactor over a CPW line; (a) photograph: dashed lines show the reference planes, (b) circuit model. 35

3.2 Taped loading of the open-ended half-wave resonators; (a) layout, (b) circuit model. 36

3.3 Taped loading of the short-ended half-wave resonator; (a) layout, (b) circuit model. 36

3.4 MEMS slow-wave resonator; (a) short-ended half-wave resonator with $n = 6$ bridges, (b) circuit model. 36

3.5 3-pole end-coupled transmission-line filter using (a) series-type resonators and inductive inverters, (b) parallel-type resonators and capacitive inverters. 41
3.6 Circuit realization of inverters; (a) K-inverter using shunt inductor, (b) J-inverter using series capacitor. 41
3.7 The complete circuit model for the tunable filter with capacitive inverters (only one half of the circuit is shown). 45
3.8 Simulated S-parameters of the capacitively-coupled tunable 3-pole filter. . 47
3.9 Photograph of the fabricated CPW tunable filter on a quartz substrate. . . 48
3.10 S-parameters of the capacitively-coupled tunable 3-pole filter. Solid lines show measured values for $V_b = 0$ and 15 V, and dashed lines show the simulations based on the fitted values of C and R. 49
3.11 The complete circuit model for the tunable filter with inductive inverters (only one half of the circuit is shown). 52
3.12 Simulated S-parameters for the inductively-coupled tunable 3-pole filter. . 54
3.13 The complete circuit model for the miniature 3-pole filter (only one half of the circuit is shown). 58
3.14 Photograph of the fabricated MEMS miniature filter (Design # 1 in Table 3.8). 59
3.15 Measured and simulated S-parameters of the miniature 3-pole filter (Design # 1 in Table 3.8). 60
3.16 The fabricate miniature-tunable filter on a glass wafer: (a) photograph, (b) tunable slow-wave section, (c) MEMS bridge profile. 62
3.17 The measured $|S_{21}|$ of the tunable resonator for different values of the bias voltage. 63
3.18 Measured and simulated S-parameters of the miniature tunable filter for $V_b = 0$ and 80 Volts; (a) S_{21}, (b) S_{11}. 65
3.19 Measured pass-band response of the miniature tunable filter for different values of V_b. 66
3.20 A CAD-based nonlinear model for the MEMS bridge capacitor. 68
3.21 Experimental setup for intermodulation measurements. 68
3.22 The third-order intermodulation product measured at $V_b = 0$ V for the capacitively-coupled tunable filter; a) the two-tone IM_3 vs. the beat frequency, b) the fundamental and intermodulation components vs. the input power. 70
3.23 The third-order intermodulation product measured at $V_b = 0$ V for the miniature-tunable filter; a) the two-tone IM_3 vs. the beat frequency, b) the fundamental and intermodulation components vs. the input power. 72
4.1 An array of antenna-filter-antenna modules as a bandpass FSS. 75
4.2 An AFA array composed of patch antennas and CPW resonators. 76
4.3 AFA as a bandpass filter between two radiative ports. 76
4.4 The layer structure used in the AFA designs. 78
4.5 Type-I AFA: a) layout, b) circuit model. 79
4.6 The simulated S-parameters of the Type-I AFA using the circuit model in Fig. 4.5b. 80

4.7 Type-II AFA: a) layout, b) circuit model. 82
4.8 The simulated S-parameters of the Type-II AFA using the circuit model in Fig. 4.7b. 83
4.9 Type-III AFA: a) layout, b) circuit model. 85
4.10 The simulated S-parameters of the Type-III AFA using the circuit model in Fig. 4.9b. 86
4.11 Representation of 4 unit cells in a periodic array of impedance panels: a) $A_r = A_c$, b) $A_r < A_c$, and c) $A_r > A_c$. Cell boundaries are shown in dashed lines. $A_c \equiv$ cell area; $A_r \equiv$ effective radiative aperture. 88
4.12 FEM simulation of the Type-I FSS: a) FEM (sloid) versus AFA circuit simulation (dashed), b) FEM simulations for different values of l_c. 91
4.13 FEM simulations of reflection and transmission coefficients a) Type-II FSS, b) Type-III FSS. Dashed lines show the AFA circuit simulation. 92
4.14 The detailed description of the physical layers in a laboratory fabricated prototype. 93
4.15 The free-space measurement system using hard horns. 96
4.16 The measured and simulated frequency response of the Type-I FSS for normal incidence with the principal polarization. 98
4.17 The measured and simulated frequency response of the Type-II FSS for normal incidence with the principal polarization. 99
4.18 Measured transmission coefficient of the Type-I FSS for 3 different values of the angle of incidence. 100
5.1 Wave transformation using a planar AFA array. 103
5.2 Filter-Lens Array using scaled AFA elements: a) a convex FLA using Type-I AFA cells, b) the amplitude response of the scaled AFA's, c) phase response. 105
5.3 Measured magnitude and phase of S_{21} in two types of AFA elements: a) Type-I element, b) Type-II element. 106
5.4 A 3-inch FLA using Type-I and Type-II elements: a) array grid geometry, b) type and scaling factor of the AFA elements. 110
5.5 Top view of the pattern measurement setup consisting the signal source, open-ended waveguide feed, FLA, box, receive horn, spectrum analyzer, and computer controlled positioner. 116
5.6 The measured radiated power (at 35 GHz) for OEWG, OEWG and FLA, and OEWG and FLA inside the box. 117
5.7 The measurement setup for the FLA gain-response. 120
5.8 The simulated aperture distribution at the output of the FLA. 121
5.9 Measured gain pattern of the FLA at 35 GHz: a) E-plane, and b) H-planes patterns. 122
5.10 Gain response of the FLA. 125
5.11 A focal plane scanning system using FLA. 126
5.12 The gain pattern of FLA in the E-plane ($\varphi = 0$) for different values of scan angle, a) $\vartheta_{scan} = -10°$, b) $\vartheta_{scan} = 10°$, c) $\vartheta_{scan} = -20°$, d) $\vartheta_{scan} = 20°$, e) $\vartheta_{scan} = -30°$, and f) $\vartheta_{scan} = 30°$. 127

5.13 The gain pattern of FLA in the H-plane ($\varphi = 90°$) for different values of scan angle, a) $\vartheta_{scan} = -10°$, b) $\vartheta_{scan} = 10°$, c) $\vartheta_{scan} = -20°$, d) $\vartheta_{scan} = 20°$, e) $\vartheta_{scan} = -30°$, and f) $\vartheta_{scan} = 30°$. 128
B-1 Interdigital capacitors as series components: a,b) symmetrical capacitor in a CPW line and its circuit model, and c,d) asymmetrical capacitor and its circuit model. 139
B-2 A series MAM capacitor: a) layout, b) circuit model. 140
B-3 Shunt inductors and their circuit model: a,b) symmetrical configuration, and c,d) asymmetrical configuration. 141
C-1 A MEMS switch-capacitor in shunt configuration: a) layout, and b) circuit model. 144
C-2 Layout of the 3-pole switched-band filter using shunt MEMS switch-capacitors. 145
C-3 Simulated S-parameters of the bandpass filter with shunt MEMS switch-capacitors. 145
C-4 A MEMS switch-inductor in series configuration: a) layout, and b) circuit model. 146
C-5 3-pole switched-band filter using series MEMS switch-inductors: a) layout, and b) circuit model. 147
C-6 Simulated S-parameters of the bandpass filter with series MEMS switch-inductors. 148
D-1 Calculated gain values vs. n. 150
D-2 Different efficiency factors vs. n. 151
E-1 FLA in a Gaussian optics measurement system. 153
E-2 Measured values of the output radiation intensity along the FLA axis. . . 153

LIST OF APPENDICES

APPENDIX

A Design of Resonant Feed Sections 136
B Modelling of In-Line Components 138
C MEMS Switched-Band Filters 143
D FLA Operation With Cosine-Type Feed Patterns 149
E Gaussian Optics Characterization of FLA 152

CHAPTER 1

Introduction

Electronic beam-steerable antennas are the ideal solution for a variety of system applications, including traffic control and collision-avoidance radars, smart base station antennas for WLAN and cellular communication, as well as beam-locked ground-satellite stations. Beam-steering is most commonly achieved through using *phased arrays*, or the so-called *focal-plane scanning* (FPS) systems. In phased arrays, the key components are phase shifters, which are used to control the relative phase of excitation between the array elements, and hence, the direction of the main-beam. In spite of the remarkable progress in developing high-performance phase-shifters in recent years [1][2][3][4], complexity, size, and assembly costs remain the unsolved issues to be addressed before the phased arrays can be used in commercial systems. Focal-plane scanning systems use a focusing device (such as a dielectric lens or a Rotman lens [5]) and a switchable array of feed antennas in the focal plane. Depending on which feed is being used, the focusing device creates a beam in different angles. The key elements here are the input switch network and the lens. While switch technology is maturing steadily for the frequencies up to W-band [6][7], lack of compact, high-performance lens structures poses major challenges in such systems. An impressive body of research can be found in recent literature concerning new array-based focusing concepts [8][9][10] and their applications for focal plane scanning and adaptive beam-forming [11][12][13].

Besides the antennas, RF filters are generally the bulkiest parts of most communication and radar systems. For a variety of reasons, bandpass filters are used at the interface of the RF front-end and the antenna in both receive and transmit paths. In some elaborate beam-steering architectures, such as active arrays or digital beam-forming systems, where an amplifier or an entire transceiver is integrated with each antenna element in the array, bandpass pre-filters are the inseparable parts of the beam-steering apparatus. In such applications, from the system integration point of view, it is desirable to combine the antenna (beam steering) and RF filters in an integrated module. The ensemble of all passive RF components, including the antenna array, phase-shifters, bandpass filters, and switches, can be referred to as the *passive RF front-end*.

A possible scenario, which is pursued enthusiastically in the context of systems on package (SoP) [14][15][16][17] for wireless communication, suggests that all of the passive components which use a similar technology are fabricated and packaged in a single process [18][19][20]. The process of choice for wireless applications (generally operating at 2-5 GHz) is based on low-temperature co-fired ceramic (LTCC) technology [21][22][23]. Given the superior performance of the RF-MEMS components at millimeter-wave frequencies [24], a similar concept may be proposed for integration of the millimeter-wave passive front-end based on the micro-fabrication technology. While, integrating the antenna with the rest of the passives is difficult to achieve at lower frequencies unless new antenna miniaturization methods are found, the millimeter-wave arrays for most applications can be easily fitted in the area of a 3-5 inch wafer, which can be used as the substrate for the rest of the MEMS devices. The main challenge in a wafer-level integration of this type, however, would be developing a low-cost high-yield MEMS fabrication process, which is far from available at this time. A more realistic approach, which also offers the flexibility of accommodating semiconductor devices, can be envisioned based on multi-chip integration of the passive components on a base wafer which carries the antenna array and possibly functions as part of the package.

Disregarding the technological challenges in realizing an integrated passive front-end, the concept proves useful in creating a research outlook in the context of millimeter-wave beam-steering systems. From this point of view, the research topics can be divided into three categories: 1) component design, 2) system architecture, and 3) combinations of 1 and 2. Besides the performance requirements such as high efficiency (for antennas), low insertion loss, good matching, high linearity (for phase-shifters, filters and switches), and good isolation (for switches), which are generally sought for at the component level, system integration requirements define an additional set of physical specifications. Small size, low weight, ease of assembly (in case of multi-chip systems), and low complexity (biasing and control circuitry), for example, are crucial in phased array applications with small cell size and large numbers of elements. At the system architecture level, developing simple beam-steering methods that require fewer number of components becomes highly desirable. Overlapped-subarrays and focal plane scanning antennas, for example, are more favorable for integration purposes, than the conventional phased arrays. Combined topics, which are in some senses the most interesting, involve developing novel multi-function modules which can replace several conventional components. Topics in this group are essentially component design problems, which result in system-level simplifications. Examples of such multi-function modules are the integrated antenna-filters [25][26], and tunable/switachable filters [27][28][29].

1.1 Thesis Overview

In this thesis, the objective is to develop hardware solutions for millimeter-wave beam-steering systems. This includes antenna and filter designs for applications in simplified architectures, based on or compatible with MEMS technology. For the most part, the topics that are addressed fall in the last of the three aforementioned categories, namely the multi-function components. The exception is design of a simple beam-steerable antenna array based on overlapped-subarrays [30]. This part, which appears in Chapter 2, examines different aspects of implementing overlapped-subarrays at millimeter-wave frequencies. The concept that was originally developed by the pioneering works of [31][32], presents a technique to reduce the number of phase shifters in a scanning array. Although overlapped-subarray antennas are easy to implement using the constrained or free-space feed networks at lower frequencies [33][34], planar implementation of these antennas at millimeter-wave bands is a rather difficult problem for a number of reasons. The chapter starts with a short theoretical account of the overlapping concept and continues to describe a planar architecture that implements the overlapped subarrays and their feed networks in a simple manner. This is an important step if such antennas are to be fabricated using planar MEMS-compatible technologies. Also, a number of new techniques are introduced and utilized to reduce or control the mutual coupling effects, which can have a detrimental impact on the functionality of the subarraying-overlapping techniques.

Chapter 3 is dedicated to MEMS tunable filters. Tunable/switched-band filters are the first examples of multi-function modules that are studied in this thesis, and can be considered for application in many communication systems. For example, they can replace the transmit and receive path bandpass filters in the half-duplex systems with different transmit and receive bands or be used as band-select filters in multi-band communication transceivers. In all of these applications, sufficient tuning range, low insertion-loss, high linearity, and compactness are the driving design criteria for such filters. Most of these requirements can be addressed by using MEMS technology. At millimeter-wave frequencies, where the semiconductor tuning devices generally have poor performance, MEMS tuning devices such as varactors, switch-capacitors, and switch-inductors show much greater promise in realizing tunable and switched-band designs. New techniques are developed in this chapter, to accommodate MEMS tuning elements in the structure of the bandpass filters. Several tunable filter topologies are derived and compared from the point of view of compactness and tuning performance. MEMS switched-band filters are briefly considered in an appendix.

Multi-function modules which combine the antenna elements and bandpass filters have been demonstrated in the past [25][26]. The antenna-filter modules can have considerable impact on reducing the complexity of the passive front-end, in the applications where each array cell contains a bandpass filter. A similar concept may be developed for the focal-plane scanning system, by integrating the focusing and filtering functions in a so-called Filter-Lens Array (FLA). In such systems, as mentioned earlier, the scanning method is very simple, but the lens is generally a bulky and heavy dielectric structure. FLA is a planar array of the antenna-filter-antenna elements (a direct extension of antenna-filters), which is fabricated using a simple MEMS-compatible thin-film process, and can replace the dielectric or Rotman lenses in the FPS systems. Besides its light weight and ease of fabrication, the basic advantage of the FLA over the other lens solutions is its dual function which allows for the elimination of the bandpass filters. For this reason, an FLA-based front-end can achieve higher efficiencies than the standard combination of antennas and bandpass filters. Two chapters of this thesis are dedicated to this topic. Chapter 4 introduces the basic concepts and design methods for the antenna-filter-antenna (AFA) elements and arrays. Several types of AFA's are designed and fabricated, and their performance is evaluated in a periodic array. In the subsequent chapter, these AFA elements are used to design an FLA. The design procedure and analysis method are described, and measurement techniques are developed. The chapter ends with extensive examination of the performance of a sample Ka-band FLA in an FPS system.

Although the hardware developments in this thesis are primarily aimed at beam-steering applications, the methods and design concepts are applicable in a more general context. Therefore, an effort has been made to structure each chapter as an independent self-consistent body of work. The best example of this effort can be found in Chapter 4, where the AFA concept is developed in the context of frequency-selective surfaces. With the same goal in mind, the thesis concludes with outlining some future research ideas, which are related but not limited to beam-steering applications.

CHAPTER 2

Interleaved-Subarray Antennas for Millimeter-Wave Applications

2.1 Introduction

Since the advent of the array theory and development of the early beam-steerable phased arrays in 1960's [35], phase-shifters have been widely recognized as the most complex, sensitive, and perhaps expensive parts of the phased array systems. In recent years, advancements in MMIC and the emerging RF-MEMS technologies has provided the designers with compact and more reliable phase-shifters [2][4]. Yet, due to the complexities in the corporate feed and biasing networks and their interactions with the radiating elements, implementation of the large phase arrays with large number of phase-shifters remains a challenging engineering problem.

In military and space applications, tolerances are usually very tight due to the stringent requirements on the antenna sidelobe-level and the fact that narrow beams and wide scan angles are often sought for. In recent years on the other hand, phased arrays are being considered for new applications such as commercial millimeter-wave automotive radars and robotic sensors. Typically, in such applications, a very precise pattern control and a wide scan angle are not required. Instead, other commercial engineering measures such as low cost, low complexity, integrability, and ease of manufacturing are the driving criteria. For these applications, switched-beam phased arrays with a reduced number of phase shifters may provide a simple and affordable alternative. Although such simplified arrays generally fail to retain a low sidelobe level for large values of scan angle, they can meet the system requirements for some of these new commercial systems, such as the forward-looking collision avoidance radars, radar sensors monitoring traffic at intersections, and sensors used for navigation.

A basic approach for reducing the number of phase shifters is based on grouping the elements of the phased array into "subarrays", and using one phase shifters per subarray. In spite of being conceptually simple, subarraying poses a number of new challenges, both in the design and in the implementation levels. Although the theoretical aspects of subarraying have been addressed extensively in the existing literature, the physical implementation generally requires ad hoc approaches which very much depend on the application, the type of elements and the available technology. In particular, a planar implementation that suits the requirements of the newly emerging applications, has not been addressed.

This chapter starts with a review of the theoretical bases of the subarrying technique and addressing the related issues. During the design of a typical array, we will show how this technique may be used to obtain a one-dimensional scanning array with a reduced number of phase shifters and a reasonably low sidelobe level. Design of the array coefficients, array architecture, and feed network are discussed and practical aspects of a fully planar implementation are investigated. We also introduce a new feeding technique which mitigates the effects of mutual coupling. This chapter is concluded with presenting the experimental results obtained for a scaled prototype in X-Band.

2.2 Grouping and Two-fold Array Theory

In the basic array theory, a symmetrical broadside array factor is achieved using an in-phase current distribution (pure real array coefficients). This array factor is made to scan by adding a linear-progressive phase factor to the array coefficients along the array axis. Varying this progressive phase results in a scanning beam. Such a scanning scheme requires one phase shifter per array element.

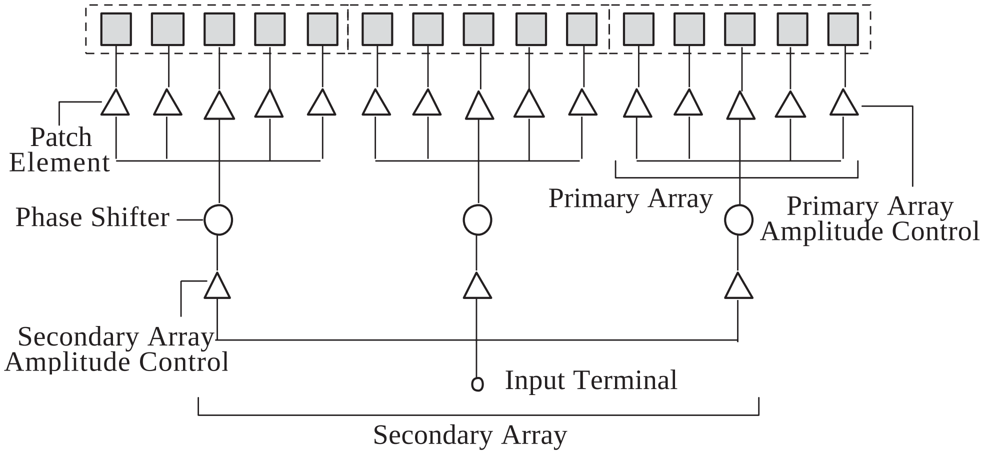

Figure 2.1: Grouping of the elements in a phased array.

The idea of reducing the number of phase shifters by dividing a large array into a large number of in-phase subarrays and using a single phase shifter for each subarray has been proposed by a number of researchers in the past [31][30]. This concept has been illustrated in Fig. 2.1. The underlying concept is to replace the linear-phase profile of the array excitation by its coarse staircase approximation. The array elements are divided into the groups of in-phase elements, or subarrays, and each subarray is fed through a single phase shifter. These subarrays can be viewed as the elements of a second phased array. In this work we assume that all subarrays are identical and refer to each one as a *primary array*. The array of the primary arrays is called the *secondary array*. The corresponding array factors are referred to as primary and secondary array factors, and designated by AF_1 and AF_2, respectively. The overall array factor is expressed as the product of the two independently synthesized array factors, AF_1 and AF_2:

$$AF(\gamma) = AF_1(\gamma) \times AF_2(\gamma) \tag{2.1}$$

where γ indicates the polar angle with respect to the array axis. The overall radiation pattern is resulted from multiplying this array factor by the element radiation pattern, F_e. When a progressive phase shift is applied to the subarrays, AF_2 starts scanning, while AF_1 remains unchanged. This concept has been illustrated in Fig. 2.2.

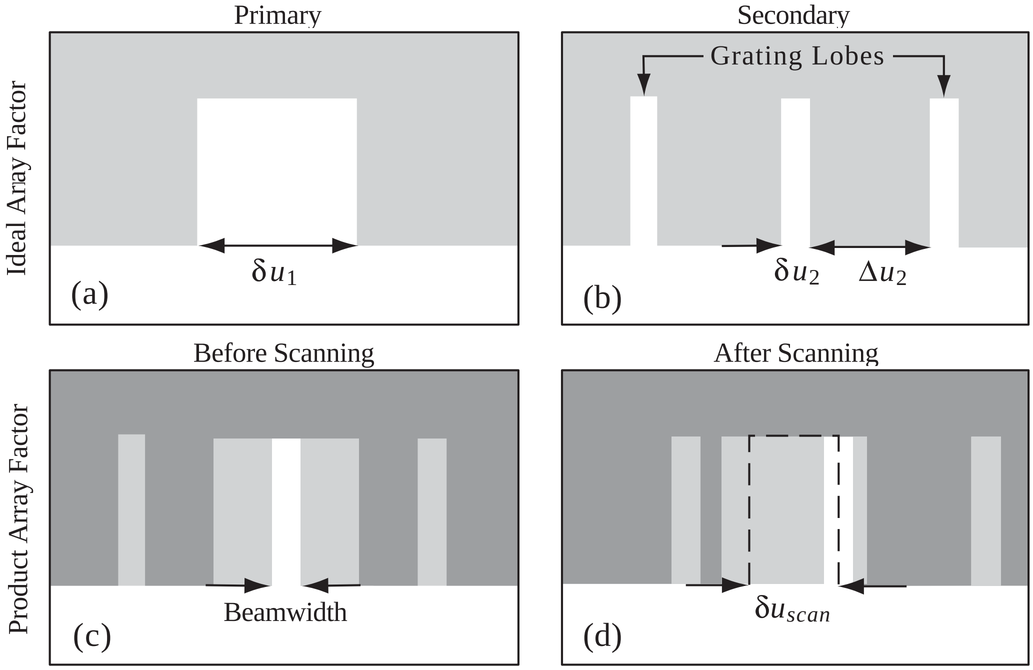

Figure 2.2: Array factor multiplication in the grouped arrays. Horizontal axes represents the angle variable u (see equation .2.5): (a) primary array factor, (b) secondary array factor, (c) overall array factor before scanning, and (d) overall array factor after scanning. All array factors are assumed ideal.

If the spacing between the subarrays exceeds a maximum value (nearly one wavelength in the broadside case), the secondary array is sparse, and AF_2 will contain a number of grating lobes in the visible region ($0 \leq \gamma \leq \pi$). Even after multiplying by the element factor, presence of these grating lobes can drastically increase the sidelobe level in the overall radiation pattern. This is generally undesirable, as it degrades the beam efficiency. A high sidelobe level can also increase the false alarm rate in the imaging and tracking systems.

As it has been proposed in [32], the sidelobe level may be controlled by a proper choice of the primary array coefficients, so that AF_1 suppresses the unwanted grating lobes of AF_2 in the overall array factor. However, it turns out that in the contiguous configuration [1], which is simply obtained by grouping the elements of an equally-spaced array into non-overlapping subarrays, no set of primary array coefficients can be found to provide sufficient attenuation at the grating lobes of AF_2, for the entire scanning range. An additional condition, which is generally referred to as "overlapping", has to be satisfied in order to resolve this problem [36].

2.3 Overlapping Condition and Interleaved Subarrays

It can be shown that in a conventional non-overlapping placement of the primary arrays, once the main beam of AF_2 scans off the boresight, its grating lobes enter to the main lobe of AF_1, where they are not subject to a substantial attenuation. In a rather instructive course, we will try to investigate the conditions under which the grating lobes of AF_2 receive enough attenuation even after scanning.

For simplicity let us assume that both the primary and secondary array factors are uniform arrays with the array factors given by [37]:

---

[1] A contiguous configuration is by definition such an arrangement in which: a) subarrays do not overlap, b) the total array length is equal to the sum of the subarray lengths.

$$AF_i(\gamma) = \frac{\sin\left(\pi\dfrac{L_i}{\lambda}\cos\gamma\right)}{N_i\sin\left(\pi\dfrac{L_i}{N_i\lambda}\cos\gamma\right)}; \quad i = 1,2 \tag{2.2}$$

where λ is the operating wavelength, and N_i represents the number of elements in the primary ($i = 1$) and the secondary ($i = 2$) arrays. L_i is the length of the ith array is defined as:

$$L_i = N_i \times D_i \tag{2.3}$$

in which D_i represents the inter-element spacing. The actual array factors (1) may be replaced with the idealized gate functions defined by:

$$AF_i(\gamma) = \begin{cases} 1, & \pi(qN_i - 1) \leq \pi\dfrac{L_i}{\lambda}\cos\gamma \leq \pi(qN_i + 1)\ ; q = 0, \pm1, \pm2, ... \\ 0, & \text{elsewhere} \end{cases} \tag{2.4}$$

Both (2.2) and (2.4) are periodic functions with a limited portion in the visible region, $0 \leq \gamma \leq \pi$. This periodic behavior is responsible for the existence of the grating lobes. If we define the array angle variable u as:

$$u = \frac{2\pi}{\lambda}\cos\gamma \tag{2.5}$$

the periodicity of the secondary array factor AF_2 as a function of u is given by $\Delta u_2 = 2\pi N_2/L_2$, while the beamwidth of the primary array factor AF_1 is corresponding to $\delta u_1 = 4\pi/L_1$. Let us define the scan-width δu_{scan}, as the separation between the beam centers at the two ends of the scanning range. If we assume that a grating lobe of AF_2 receives enough attenuation. As long as at least half of its beamwidth falls outside the main beam of AF_1, referring to Fig. 2.2d, this condition can be expressed as:

$$\Delta u_2 \geq \frac{1}{2}(\delta u_1 + \delta u_{scan}). \tag{2.6}$$

The scan-width δu_{scan}, on the other hand, cannot be greater than δu_1, and may be written as:

$$\delta u_{scan} = \alpha \delta u_1; \quad 0 \leq \alpha < 1. \tag{2.7}$$

Using (2.7), (2.6) is simplified to the following form:

$$\Delta u_2 \geq (1+\alpha)\frac{\delta u_1}{2} \tag{2.8}$$

which in terms of array parameters, this may be written as:

$$L_1 \geq (1+\alpha)\frac{L_2}{N_2} = (1+\alpha)D_2. \tag{2.9}$$

Equation 2.9 represents the condition on the subarray length and spacing to avoid grating lobes in the overall array factor.

Considering that D_2 is in fact the distance which is allocated to each subarray in the secondary array configuration, it is useful to define an *overlapping factor*:

$$OF = \frac{L_1}{D_2} - 1 \tag{2.10}$$

which basically represents the fraction of the length of a subarray which overlaps with each of its neighboring subarrays. For the non-overlapping subarrays $OF \leq 0$ (the equality referring to the contiguous subarrays), while for the overlapped subarrays OF is a positive number.

In terms of the overlapping factor, (2.9) may be rewritten as:

$$OF \geq \alpha = \frac{\delta u_{scan}}{\delta u_1}. \tag{2.11}$$

This states that for non-zero scan-width ($\alpha > 0$), the subarrays must be arranged in an overlapping fashion to avoid grating lobes. The minimum required amount of overlapping is equal to α.

Although this proof is based on the idealized array factors given by (2.4), the result is generally true for the actual array factors, except that the beam-widths are replaced with half-power beam-widths. However, the overlapping condition may be less stringent in the actual cases ($OF < \alpha$), as will be seen in the design example presented in next section. For narrow scan angles, subarray overlapping may be used to achieve very low sidelobe levels. For moderate scan angles, this technique allows for the sidelobe levels of down to -20 dB [34].

There are at least two ways to realize overlapped subarrays. One way is to share one or more of the end elements of the adjacent subarrays, as shown in Fig. 2.3. In this arrangement, each shared elements can be considered as two superimposed elements that to two different subarrays, and its excitation coefficient is obtained from adding the two partial excitation coefficients. This results in an equally-spaced array constellation, which is commonly known as *partially-overlapped subarrays*.

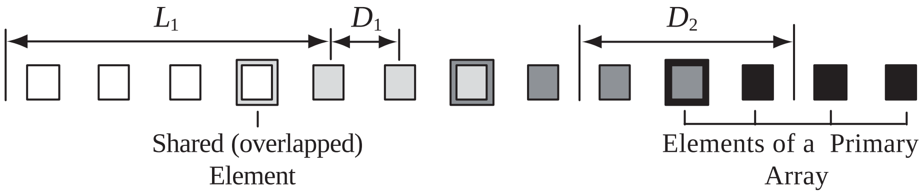

Figure 2.3: Partially-overlapped subarrays in a linear arrangement.

The second approach is to interleave some of the end elements of the neighboring subarrays (Fig. 2.4). Each element belongs to only one subarray in this case, and has a simple excitation coefficient. This constellation may be referred to as *interleaved subarrays*. Even if the the elements are equally-spaced in the constituent subarrays, the interleaving results in a non-uniformly-spaced constellation. Maybe for this reason, the first approach has gained more popularity among the previous researchers. In this work, however, for the reasons that will become clear, we choose the interleaved subarrays to realize overlapping.

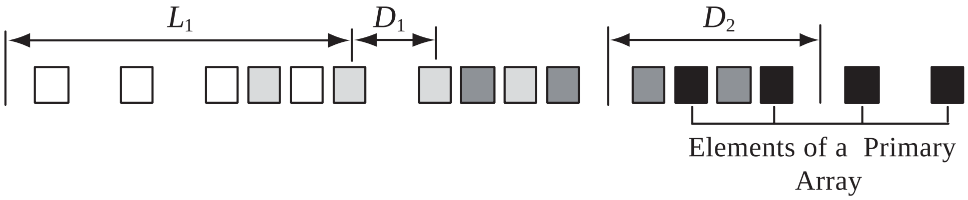

Figure 2.4: Interleaved subarrays in a linear arrangement.

2.4 Array Design

Overlapped subarrays may be designed for a given beamwidth, sidelobe level, and scanning range. The lengths of the primary and secondary arrays (L_1 and L_2) are calculated from the required values of scanning range and beamwidth, respectively. The primary array is designed to provide the required beamwidth and sidelobe level with a miniaml number of elements, N_1. The number of elements in the secondary array, N_2, is then set to the minimum for which the grating lobes of AF_2 receive enough suppression from AF_1, under the maximal scanning condition (always $> L_2/L_1$ due to the overlapping). N_2 determines the required number of phase shifters. As the sidelobe level is a primary concern, Dolph-Chebyshev array coefficients [37] are used for both the primary and secondary arrays.

The aforementioned procedure has been used for designing a phased array with a sidelobe level of < -20 dB, a half-power beamwidth ($HPBW$) of 7 degrees, and a scanning range of ±10.5 degrees (corresponding to a scan-width of ±7 degrees). This array is considered for a radar system mounted on a tower for monitoring the railroad crossing intersections. The number of elements in the primary and secondary arrays were found as $N_1 = N_2 = 4$ in this case, resulting in a 16 element array constellation. The values of L_1, L_2, as well as the excitation coefficients for the primary and the secondary arrays are given in Table 2.1. The overlapping factor in this case is 0.6, which is slightly lower than the theoretical minimal value of 0.64, calculated using (2.11). The primary array factor is designed for a -20 dB sidelobe level. Assuming a cosine type element factor that provides an extra attenuation of approximately -1 dB at the first sidelobe of AF_2, we design the secondary array factor for a sidelobe level of -19 dB, which is slightly higher than the design requirement. This allows for more flexibility in the design. The corresponding array factors are shown in Fig. 2.5. Using a cosine type element factor, the overall radiation pattern can be calculated for the boresight and squint beam positions, as presented in Fig. 2.6.

	Primary Array	Secondary Array
Array Length	2.73λ	6.83λ
Inter-Element Spacing	0.68λ	1.71λ
HPBW	22 degs.	8.5 degs.
Sidelobe Level	-20 dB	-19 dB
Array Coefficients	1,1.74,1.74,1	1, 1.66, 1.66, 1

Table 2.1: Parameters of the primary and secondary arrays.

2.5 Implementation Challenges

Overlapped subarrays may be easily implemented in applications such as radio astronomy and deep space communication, where large arrays of high gain antennas with very large inter-element spacing are used to form extremely narrow beams. However, a planar implementation of the overlapped subarrays proves rather difficult [33], especially when the array is composed of closely spaced low-directivity elements. In such circumstances the mutual coupling between the antenna elements becomes a major obstacle for realizing the desired array coefficients. Another difficulty in the planar implementation of the interleaved subarrays (and also the partially-overlapped subarrays with more than one shared element) is implementing the crossovers in the intersecting subarray feed networks. A commonly used approach for feeding the overlapped subarrays is based on a combination of hybrid couplers, which allow

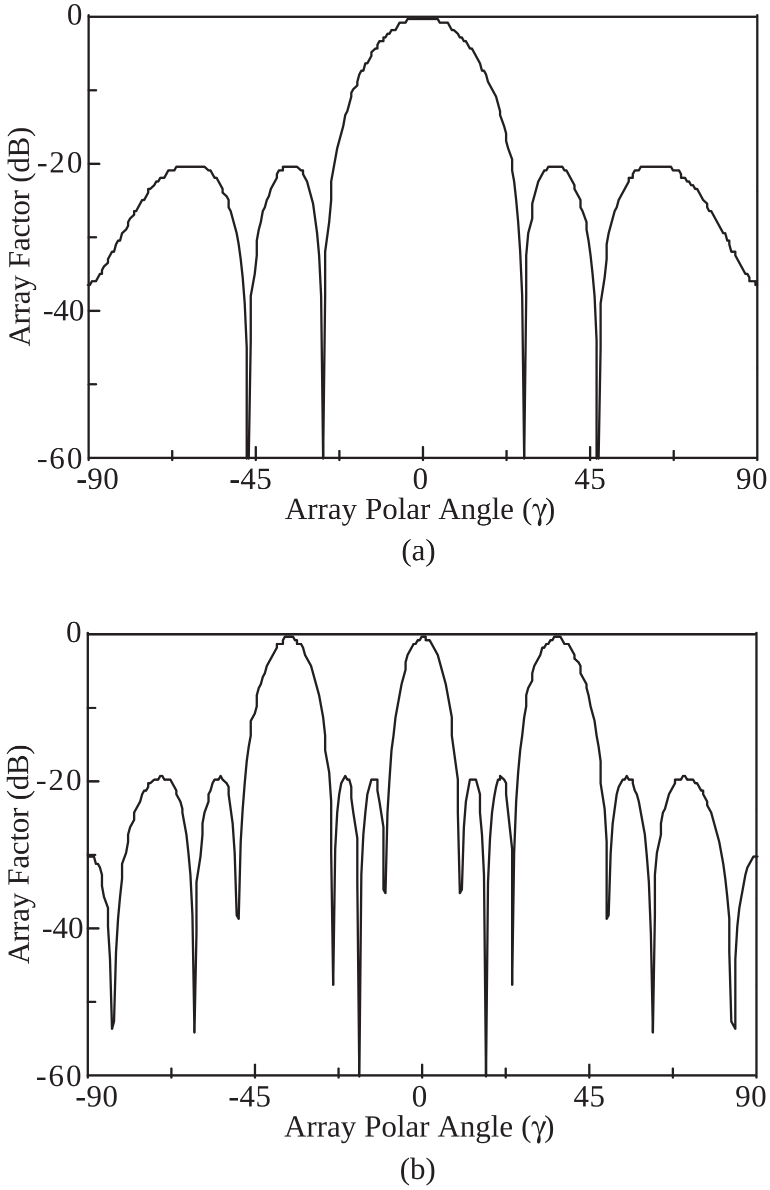

Figure 2.5: Synthesized array factors vs. the array polar angle γ; a) primary, b) secondary.

cross-feeding by successive formation of sums and differences of the input signals [33]. Such feed networks are relatively complicated, need significant real estate, and their accuracy is limited by the performance of the hybrid couplers. In addition, due to the size of the feed network, this feeding scheme and its variations are lossy in the millimeter-wave frequencies.

As mentioned before, the mutual coupling between the elements of the overlapped

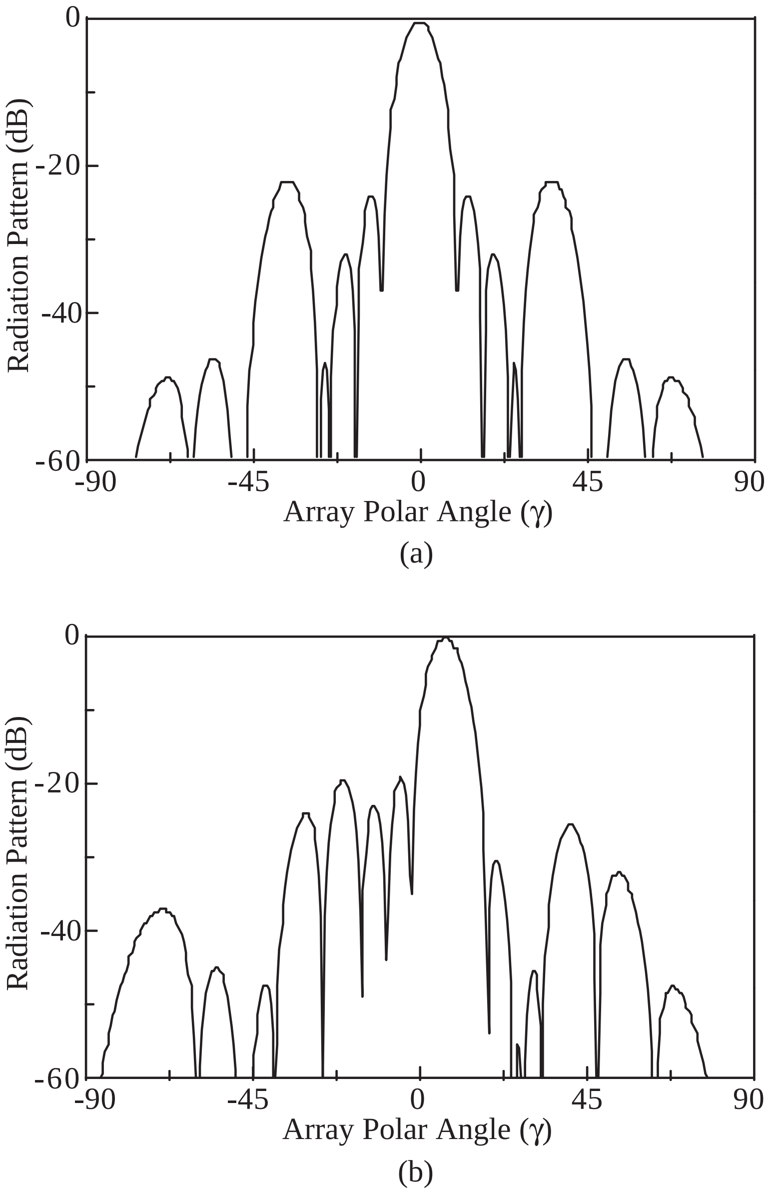

(a)

(b)

Figure 2.6: Radiation pattern of the combined array vs. the array polar angle γ; a) without scanning, b) with +7 degs. scanning.

subarrays complicates the design task. The difficulty is exacerbated when the array is made to scan. This is due to the fact that changing the relative phase of the array coefficients varies the mutual coupling between the elements. Therefore it is very difficult, if not impossible, to design an array which is impedance matched and properly excited in all states of operation, unless these mutual effects are minimized.

Apart from mutual coupling minimization, it is also important to design the feed network so that the subarray excitation coefficients remain insensitive to the mutual coupling. Techniques to address these two tasks, along with a simple implementation of cross-feeding are discussed in the rest of this chapter.

2.6 A Planar Implementation of The Interleaved Subarrays

The array coefficients calculated in the previous section may be used to design a two dimensional array of 16×5 elements with the capability of scanning in the horizontal plane. This array which is shown in Fig. 2.7, is composed of 16 identical rows, each including five series-fed rectangular microstrip patch antennas. With the Dolph-Chebyshev array coefficients of 1:1.61:1.93:1.61:1, each vertical row has a narrow-beam pattern with a side lobe level of -20 dB in the vertical plane, and a broad-beam cosine type pattern in the horizontal plane. These rows act as the elements of the subarrays, with the excitation coefficients given in Table 2.1. The subarrays are, as a result, two-dimensional arrays of 4×5 elements, as shown in Fig. 2.7.

In each row, the array coefficients are implemented through a series of resonant microstrip line sections [2], which connect the patch elements in the antenna layer. The horizontal array coefficients in each subarray are set to the designed values, using a corporate network of such resonant feed sections. This corporate feed network is fabricated on a second microstrip layer (feed layer) which is isolated from the antenna layer by a common ground plane. Coupling between the corporate feed and the microstrip antennas is achieved through subresonant slots in the ground plane, which are placed underneath the central element of each row. Layouts of the antenna and

---

[2] See Section 2.8

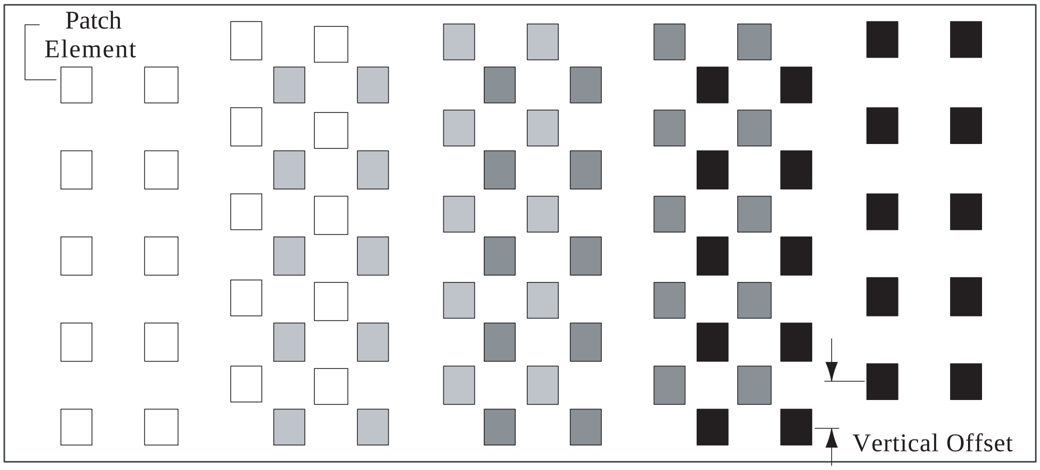

Figure 2.7: Simplified layout of the 80 element array; different subarrays are shown in different gray levels.

the feed layers are shown in Fig. 2.8 for a single subarray. The resonant sections used in this design are simply two-port microwave networks that provide a fixed voltage ratio between the input and output, independent of the loading conditions. Principle of operation and design procedure for the resonant feed sections will be described in section 2.8.

Each subarray is connected to the secondary array feed network at the input terminal of the corporate feed. Assuming that the subarrays are properly matched at these terminals, a conventional 1-to-4 tree power divider along with phase shifters at its output terminals may be used to realize the desired excitation coefficients for the secondary array (as given in Table 2.1). The power divider and phase shifters are also fabricated on the feed layer. Phase shifters may be realized as the integrated parts of the feed network, or they can be fabricated separately and assembled on the feed network using wire-bonding, or flip-chip techniques. Design of the planar phase shifters using MEMS technologies is beyond the scope of this work and will not be discussed here. Interested readers are referred to [1] and [24] for a more comprehensive account of this subject.

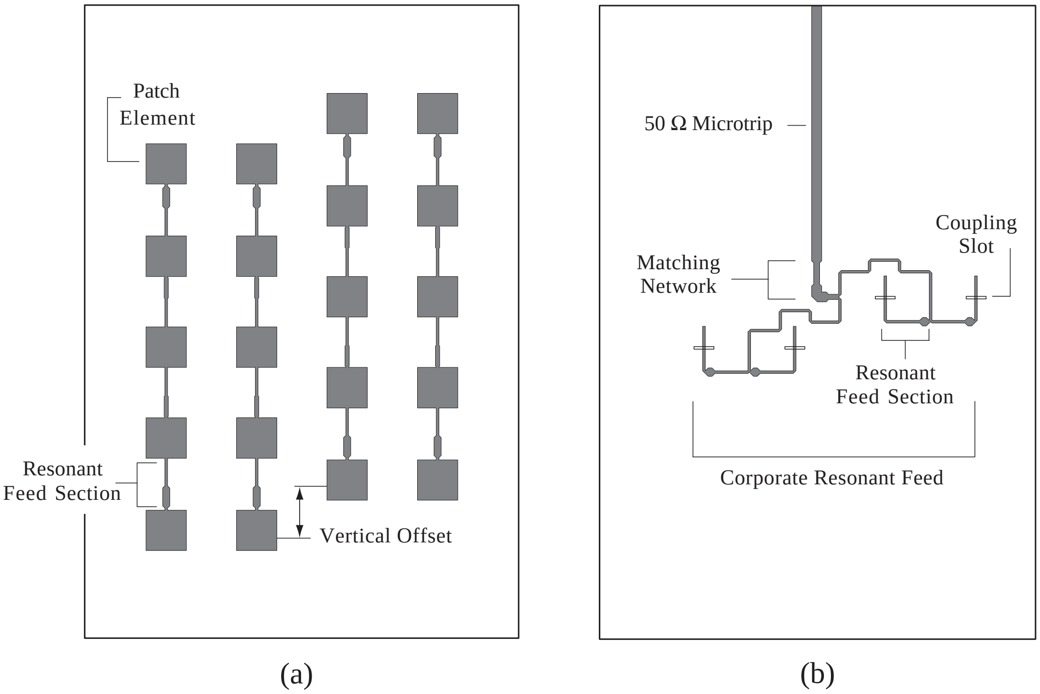

Figure 2.8: Subarray layout; (a) antenna layer, (b) feed layer.

2.7 Offset Subarray Constellation

Layouts of the antenna and feed layers are shown in Fig. 2.9, for the full array. Subarray overlapping is achieved by interleaving the rows of the neighboring subarrays in the overlapping region. As it has been shown in Fig. 2.9a, the interleaved rows are positioned with a vertical offset. Such a vertical displacement does not affect the radiation pattern in the horizontal plane, and since the offset length is small as compared to the length of the rows, its effect on the vertical plane pattern is negligible. The advantage of the offset arrangement of the adjacent rows, on the other hand, is two-fold: 1) it allows the interleaved subarrays to be fed through non-intersecting feed networks, and 2) it reduces the mutual coupling between the closely spaced rows of the interleaved subarrays. Figure 2.8b shows a subarray corporate feed which has been modified to conform with the offset geometry of the subarray. As shown in Fig. 2.9b, such corporate feeds may be used to feed the overlapped subarrays in a non-intersecting fashion.

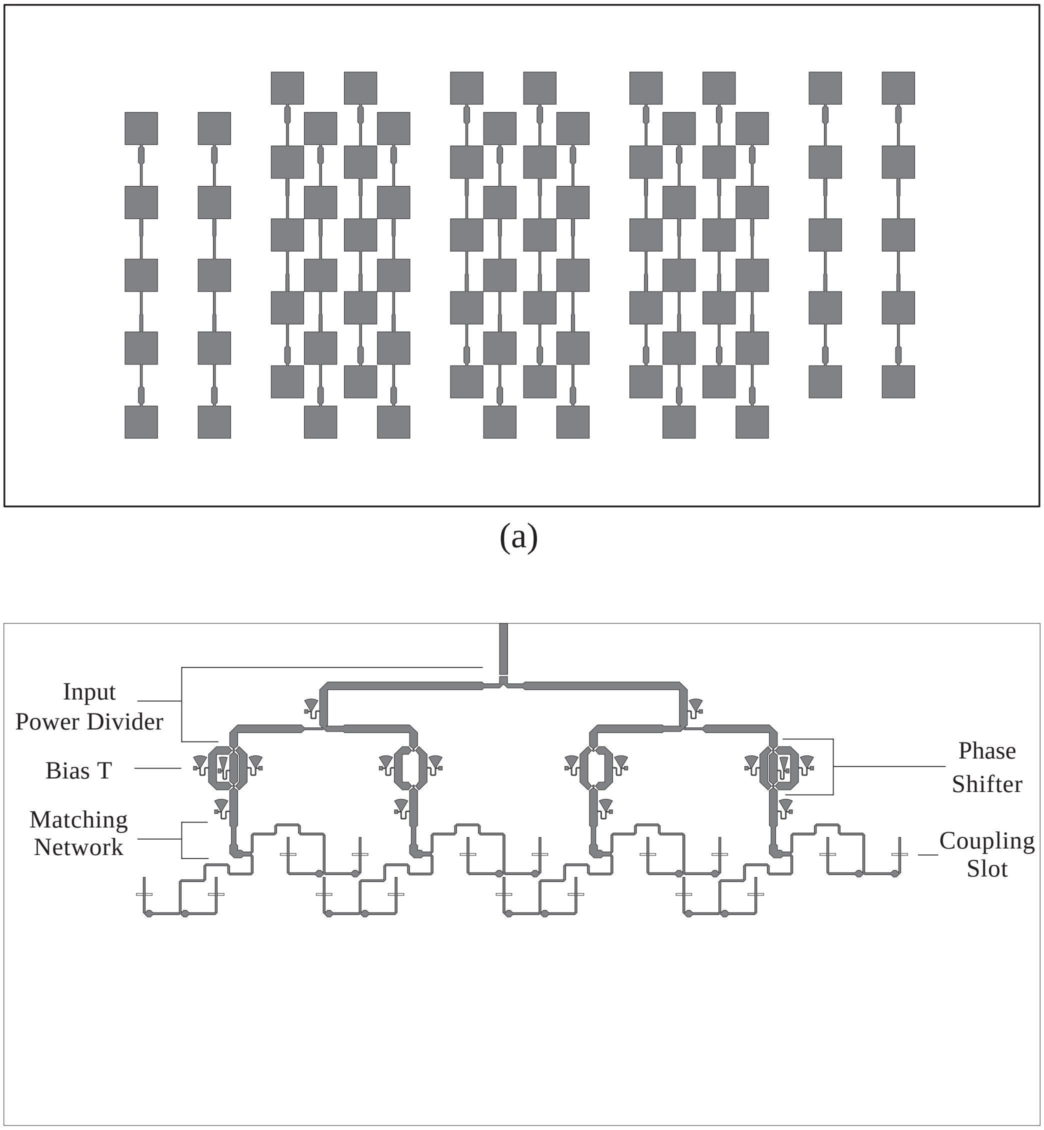

(a)

(b)

Figure 2.9: Layout of the two-layer phased array; (a) antenna layer, (b) feed layer.

The effect of vertical offsetting in reducing the mutual coupling between closely spaced elements can be studied using a simple numerical experiment. Fig. 2.10 shows the simulated value of $|S_{21}|$ between the input terminals of two adjacent rectangular microstrip antennas, as a function of the vertical offset h. The patch antennas are optimized for operation at 60 GHz, similar to those used in the array, and are positioned with a horizontal center-to-center distance of $d_{min} = D_1/2$ which is equal to the shortest horizontal separation occurring between the interleaved elements of two neighboring subarrays. It is observed that the value of $|S_{21}|$, which indicates mutual coupling, is reduced with increasing the vertical offset, and reaches a minimum for $h = \lambda/4$.

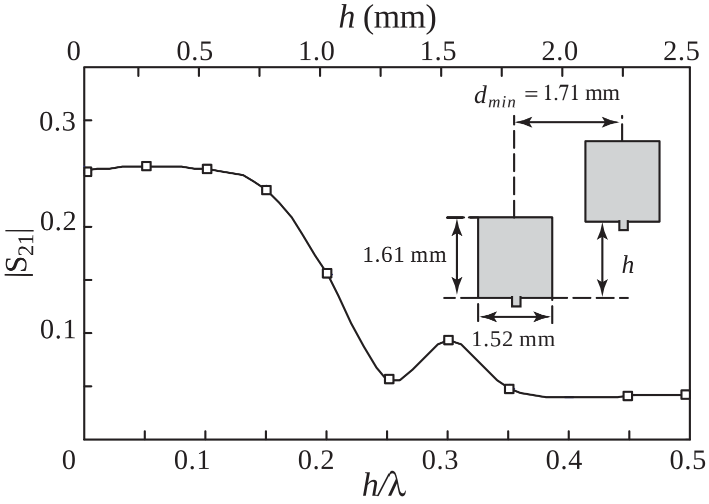

Figure 2.10: Mutual coupling between two adjacent patch antennas vs. vertical offset.

As mentioned earlier, since in a scanning array the amount of mutual loadings are not constant and depend on the state of the beam, in principle it is impossible to account for the mutual coupling in the design of the feed network, and therefore it is important to minimize such effects as much as possible. On this context, the importance of the offsetting of the adjacent elements becomes evident. To further minimize the effect of mutual coupling on the excitation coefficients in a subarray, we introduce the concept of resonant feed network in the next chapter.

2.8 Resonant Feed Networks

To enforce a nodal voltage distribution which is independent of loading, a class of standing-wave feed sections can be designed and placed between the elements of the microstrip array. Assuming that the form of the current distribution over each patch is fixed and the proximity of the other elements only changes the amplitude of this distribution, the input currents $\{I_j\}$ and the edge voltages $\{V_j\}$ of the array elements are related through an admittance matrix $[Y_{j,i}]$. The total input current to the j'th patch is given by:

$$I_j = Y_{j,j} V_j + \sum_{i \neq j} Y_{j,i} V_i = (Y_j^{rad} + \sum_{i \neq j} Y_{j,i} \frac{V_i}{V_j}) \times V_j, \tag{2.12}$$

where $Y_j^{rad} = Y_{j,j}$ represents the edge radiative admittance of the element, and $Y_{j,i}$ is the mutual admittance between j'th and i'th elements. For the given edge voltage ratios V_i/V_j, the coupled network may be replaced by an array of uncoupled admittance loads Y_j^a (usually referred to as the *active admittance* [37]), given by (8):

$$Y_j^a = \frac{I_j}{V_j} = Y_j^{rad} + \sum_{i \neq j} Y_{j,i} \frac{V_i}{V_j} = Y_j^{rad} + Y_j^{ext}, \tag{2.13}$$

where Y_j^{ext} represents the effect of mutual coupling from the other elements in the array.

Assuming that the feed network establishes the desired edge voltage ratios between the patch elements, the active admittances Y_j^a generally can be calculated from (2.13) and used for designing the feed network. In our case, however, the voltage distribution over each subarray can also be affected by the coupling from the neighboring subarrays, which varies with the change of their relative phase of excitation. To eliminate the dependence of the voltage distribution on this variable mutual coupling, the subarry feed network must be designed so that its relative terminal voltages are independent of the loading. In the rest of this section, we will describe a procedure for designing such a feed network.

Assume that the edges of two neighboring patch antennas in the array are con-

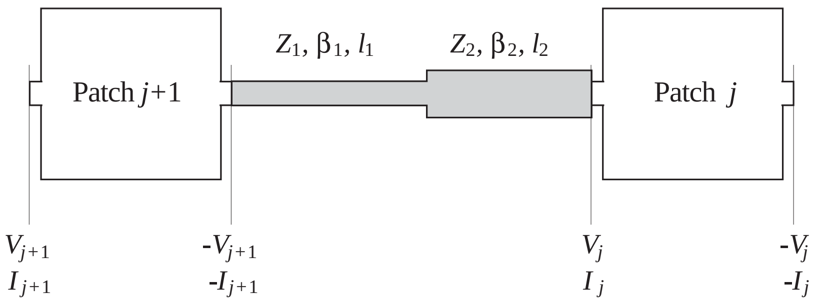

Figure 2.11: Patch elements connected using a two-part transmission-line feed section.

nected through a two-segment transmission-line with electrical lengths $\beta_1 l_1$ and $\beta_2 l_2$ and characteristic impedances Z_1 and Z_2, as shown in Fig. 2.11. Neglecting the losses, the $ABCD$ matrix of the two-part transmission-line is obtained by multiplying the $ABCD$ matrices of the individual sections:

$$\begin{pmatrix} a & b \\ c & d \end{pmatrix} = \begin{pmatrix} \cos\beta_1 l_1 & jZ_1 \sin\beta_1 l_1 \\ \dfrac{j}{Z_1}\sin\beta_1 l_1 & \cos\beta_1 l_1 \end{pmatrix} \times \begin{pmatrix} \cos\beta_2 l_2 & jZ_2 \sin\beta_2 l_2 \\ \dfrac{j}{Z_2}\sin\beta_2 l_2 & \cos\beta_2 l_2 \end{pmatrix}. \tag{2.14}$$

As for a resonant patch the voltages between the two opposite edges are only related by a factor of -1, the left edge voltage of the $j+1$th patch, V_{j+1}, is related to the left terminal voltage and current of the j'th patch, V_j and I_j, as:

$$\begin{aligned} -V_{j+1} &= aV_j + bI_j \\ &= (\cos\beta_1 l_1 \cos\beta_2 l_2 - \frac{Z_1}{Z_2}\sin\beta_1 l_1 \sin\beta_2 l_2)V_j \\ &+j(Z_2 \cos\beta_1 l_1 \sin\beta_2 l_2 + Z_1 \sin\beta_1 l_1 \cos\beta_2 l_2)I_j. \end{aligned} \tag{2.15}$$

To Establish a terminal voltage ratio $V_{j+1}/V_j = K$ which is independent of the terminal currents, (10) requires that $a = -K$ and $b = 0$. Another constraint which is imposed by the array inter-element spacing, on the other hand, fixes the total length $l_1 + l_2$ to a given value, l. These conditions may be combined to result in the following set of equations:

$$
\begin{aligned}
&l_1 + l_2 = l && \text{(a)} \\
&\cos\beta_1 l_1 = -K\cos\beta_2 l_2 && \text{(b)} \\
&Z_1/Z_2 = -\tan\beta_2 l_2/\tan\beta_1 l_1 && \text{(c)}
\end{aligned}
\tag{2.16}
$$

Noting that on a given substrate β_1, β_2, Z_1, and Z_2 are functions of the line widths W_1 and W_2, one can solve (2.16) for l_1, l_2, W_1 and W_2 to achieve the desired voltage ratio K. As the number of unknowns is larger than the number of equations, an extra constraint may be applied, for example by setting the smaller of W_1 and W_2 to the minimum realizable width (here 100 μm). Not for all values of K and l, however, do these equations have a solution which results in a realizable admittance ratio. Yet, for typical values of K between 1/3 and 3, and $\beta_1 l_1 + \beta_2 l_2$ between $\pi/2$ and $3\pi/2$, one can normally find a solution with feasible values for Z_1 and Z_2.

It can be shown that the two-segment transmission line obtained in this way has a singular impedance matrix. Hence, we refer to such a structure as a *resonant feed section.* The relative terminal voltages of all patch elements in a subarray may be fixed by successively locking the terminal voltages of the adjacent elements using such resonant feed sections. The combination of these resonant feed sections is called the *resonant feed network*, and has the property that its terminal voltage distribution is independent of the loading. The procedure for designing a resonant feed section has been described in Appendix A, for an example design case.

Although the resonant feed network enforces the desired voltage distribution, it does not provide a straightforward relation between the reactive parts of the input admittance and the terminal loadings. Therefore, it is not possible to design a resonant feed network which simultaneously provides the desired voltage distribution and the input matching. A practical approach is to design the feed network for the voltage distribution, and then calculate or simulate the input impedance of the entire structure. Once the input impedance is known, one can easily use a simple matching network to match the synthesized array. In our case, we use matching networks at the input of each subarray. Aside from the mismatch losses, the impedance matching of the subarrays is essential for proper operation of the phase shifters and the input power divider. A simple matching network can be obtained by cascading two or three transmission line sections. As patch antennas are inherently narrow-band elements, the bandwidth of the matching and resonant feed networks are not of particular importance in the design procedure.

2.9 Experimental Results

The 5×4×4-element array described in Section 2.6 is considered for a millimeter-wave traffic control radar operating at 60 GHz. This simple radar system is intended for monitoring a railroad crossing to inform an approaching high speed train of the vehicles and objects that might be on the track. A scaled prototype of this array was fabricated and measured in X-band. A photograph of the fabricated prototype is shown in Fig. 2.12. This array is fabricated on a 0.79 mm-thick Teflon substrate, with a relative permittivity of $\varepsilon_r = 2.2$. As the original design was for the same substrate with 0.13 mm thickness, the layout is scaled by a factor of 6.2 to maintain the design properties. The nominal frequency of operation, therefore, is scaled down to 9.68 GHz.

First, a single subarray is fabricated and measured. Figure 2.13 shows the measured and simulated radiation patterns in the vertical and horizontal planes. Simulations are performed by the commercial moment-method simulators IE3D [38] and Momentum [39]. In both principal planes, a good agreement between the measurement and simulation is observed. Moreover, if the element factor is extracted (approximately $\cos\varphi$ in the horizontal plane and unity in the vertical plane), these patterns reduce to nearly equi-sidelobe Chebychev array factors, for which the array coefficients were designed. This indicates that the resonant feed network has successfully

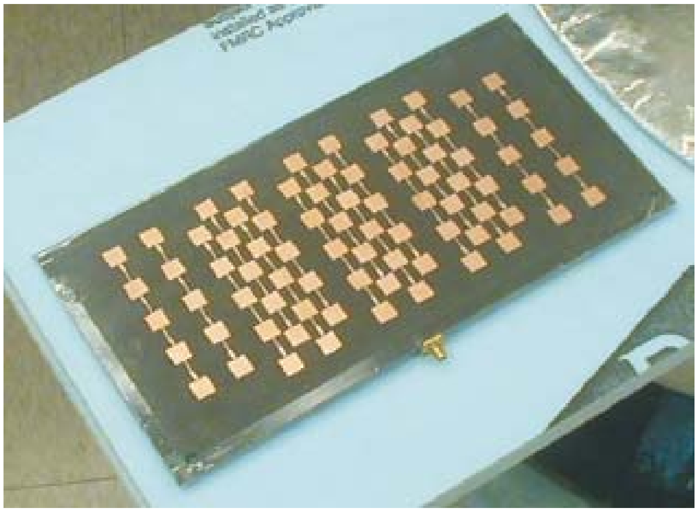

Figure 2.12: The X-band prototype of the 80-element array.

set the excitation coefficients to the targeted values. The measured sidelobe level is less than −20 dB in both planes. A return loss of better than 10 dB was measured over a 4% bandwidth for this subarray. These results and some other subarray parameters are summarized in Table 2.2.

Resonance Frequency	9.68 GHz
-10 dB Bandwidth	4%
HPBW (H†)	22 degs.
HPBW (V‡)	16 degs.
Sidelobe Level (H†)	< -22 dB
Sidelobe Level (V‡)	< -20 dB
Directivity	20.6 dB
Cross-Polarization	< -22 dB

†In horizontal plane ‡In vertical plane

Table 2.2: Measured Data for the Primary Array.

To form the 80-element array, four subarrays are combined through a corporate feed network. The corporate feed is a two-stage input-matched power divider that

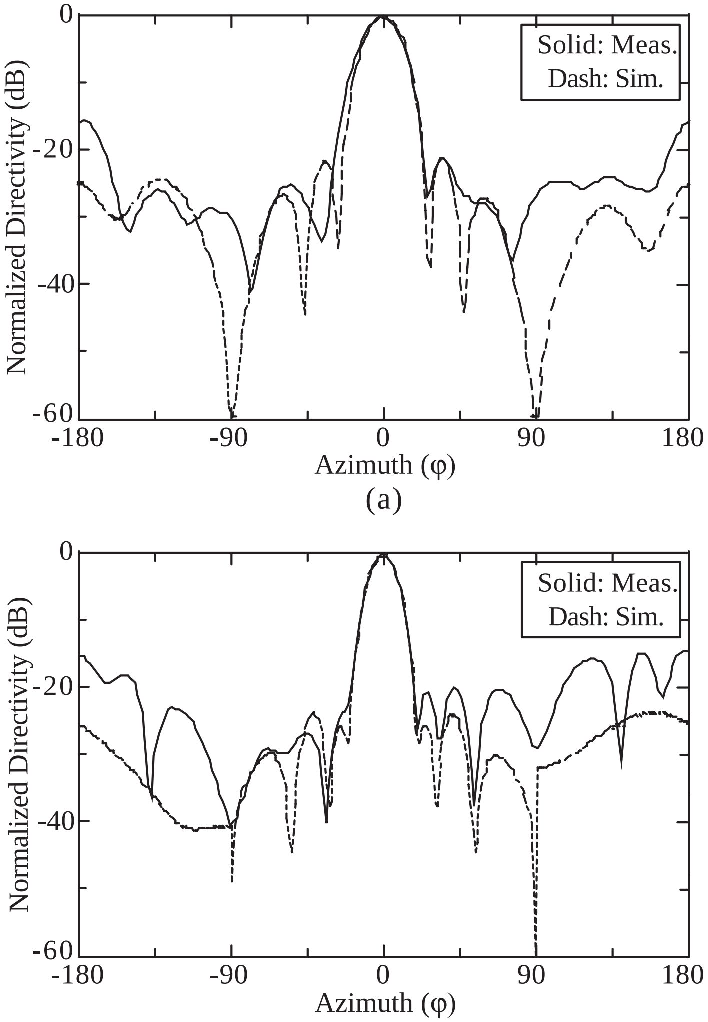

(a)

(b)

Figure 2.13: Measured and simulated radiation patterns for a subarray; a) horizontal plane, b) vertical plane.

is designed to provide the required excitation coefficients for the secondary array, as given in the last column of Table 2.1. Resistors are not used in the design of this power divider, expecting a balanced operation. Two different prototypes were fabricated for the boresight and squint-beam arrays. The phase shifters were replaced by fixed delay lines in these prototypes. Figure 2.14 shows the measured and simulated radiation patterns of the 80-element phased array for boresight and squint-beam modes of operation. Only the horizontal plane patterns are shown, as the pattern in the vertical plane is identical to that of the subarrays. Sidelobe levels of −20 dB and −19 dB are measured for the boresight and squint-beam cases, respectively. With a measured beamwidth of 8 and 16 degrees in the horizontal and vertical planes, the estimated directivity of the array is 25 dB. The measured gain with the beam at the boresight is 20.6 dB, which corresponds to an efficiency of 36%. The power dissipation can be attributed to the Ohmic and surface wave losses in the patch elements as well as the feed network. Similarly, in the squint beam position the calculated directivity and measured gain are 24.8 dB and 20 dB, respectively, which results in an efficiency of 33% in this case.

The measured return loss of the full array is presented in Fig. 2.15. The 10-dB bandwidth of the array is observed to be 6.3% and 8.5% for the beam at boresight and squint positions, respectively. In both cases a broader bandwidth is observed as compared to the subarray case, which is believed to be due to the presence of the power divider which along with the subarray matching networks forms a higher order input matching. Although these bandwidths are not symmetrically spanned around the design frequency of 9.68 GHz, a pseudo-resonance is observed near this frequency. The bandwidth enhancement in the squint beam position is believed to be result of the out-of-phase interference of the partial reflected signals from different subarrays, which reduces the net reflected power. The measured performance data for the 80-element array are listed in Table 2.3.

2.10 Conclusion

In this chapter, we demonstrated that the fabrication complexity of the beam-steerable phased array systems can be drastically reduced by using subarraying techniques. The fundamental concepts and practical issues were explored, and a design procedure was developed. It was shown that low sidelobe levels may be achieved for a

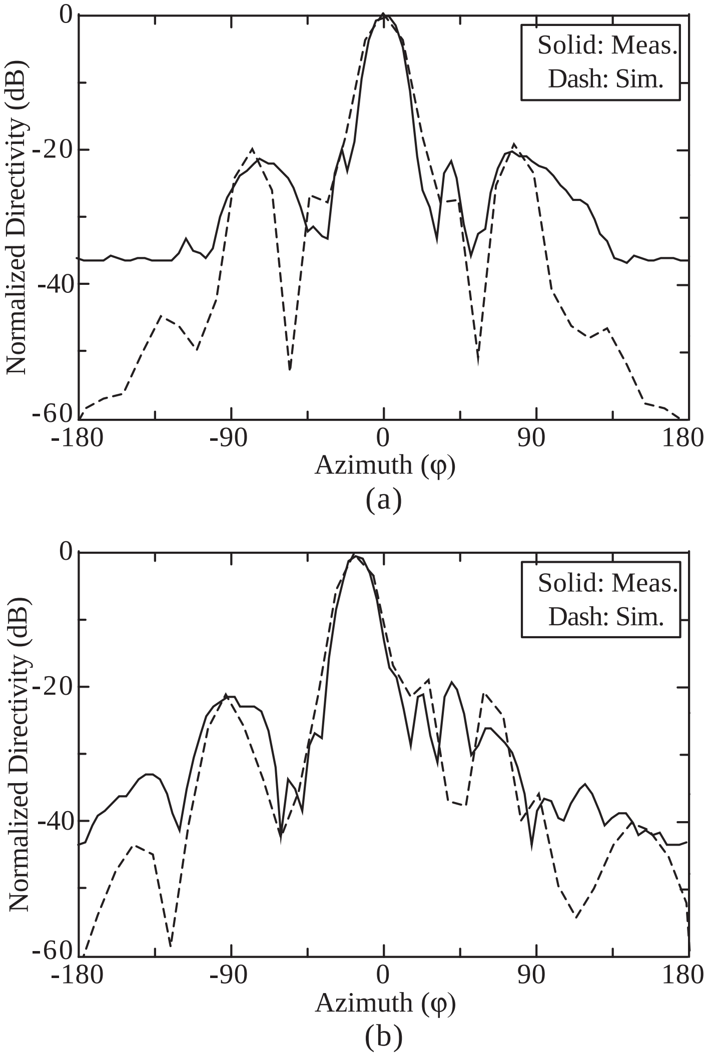

Figure 2.14: Measured and simulated radiation patterns of the full array in the horizontal plane; top: boresight beam position, bottom: squint beam position.

relatively narrow scan angle. The effectiveness of this method becomes evident when a scanning array with high angular resolution and a large number of beam states is required.

A planar implementation of partially-overlapped subarrays, suitable for millimeter-wave applications was demonstrated. Using a multitude of innovative approaches, a simple two-layer realization is obtained, which eliminates many problems in both design and fabrication stages. Issues involved in the design of the feed network, as

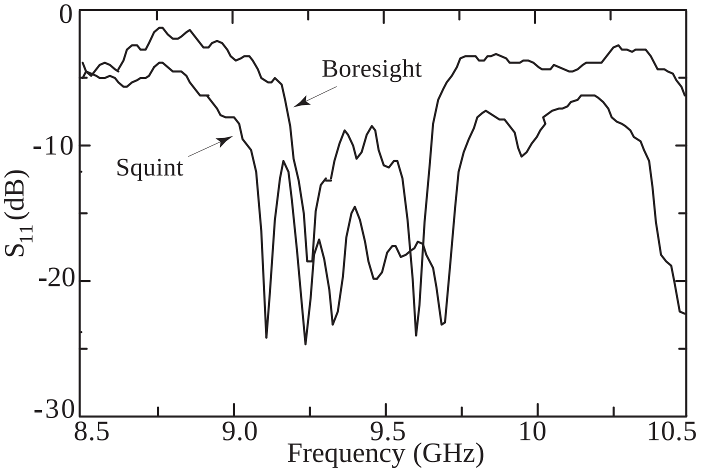

Figure 2.15: Measured S_{11} vs. frequency in the boresight and squint beam positions.

	Boresight	Squint
Center Frequency	9.45 GHz	9.40 GHz
-10 dB Bandwidth	6.3%	8.5%
HPBW ($H^\dagger$)	8.0 degs.	8.5 degs
Sidelobe Level ($H^\dagger$)	< -20 dB	< -19 dB
Directivity	25.0 dB	24.8 dB
Gain	20.6 dB	20.0 dB
Efficiency	36 %	33 %

†In horizontal plane.

Table 2.3: Measured Data for the Primary Array.

well as the mutual coupling concerns in the layout design were addressed. The concept of resonant feeding developed in this chapter, can be used as a basis for the robust control of the phased array excitation coefficients in heavy mutual coupling environments. In the applications where a narrow scanning range is required, these techniques may be combined to provide a cost-effective solution. The proposed planar design is conducive for integration of the phased array with the rest of the RF front-end.

CHAPTER 3

MEMS Tunable Filters

3.1 Introduction

Low-loss bandpass filters are the basic components of transceivers, either as band-select or image-reject units. In highly integrated systems, however, design of the bandpass filters is generally subject to serious size constraints. For example, in active phased arrays, one filter is required per antenna element, and the filter size cannot exceed a fraction of the free-space wavelength which is the typical cell size in the array. In multi-band receivers, a single fixed-band filter cannot fulfill the filtering requirements for all receive bands, and filter-banks are generally used in most communication systems. An interesting approach which is particularly useful in the active array example, is to integrate the bandpass filters with the antenna elements, as has been proposed in [26], [25]. A more general approach is based on the miniaturization of the bandpass filters. In the case of multi-band receivers, an ideal solution is replacing the filter-bank by a tunable filter that covers the entire frequency range. In very wideband applications, a small bank of tunable filters can be used to replace huge filter banks.

The existing work in the area of filter miniaturization includes loading of the transmission line resonators with lumped elements [40][41], novel compact geometry resonators [42][43][44][45], dual-mode resonators [46][47][48][49], and using new materials and artificial dielectrics [50][44][51][52]. Among these, the designs with integrated lumped components are suitable for tunable filters, but they generally suffer from high insertion loss due to the low Q of the conventional tuning elements, MIM (metal-insulator-metal) capacitors and planar inductors.

RF MEMS capacitors are high-Q elements (up to > 300 at 21 GHz) and when used for loading the resonators of a CPW (co-Planar Waveguide) filter, they do not degrade the resonator Q significantly and therefore add little to the mid-band insertion loss. A number of researchers have successfully used MEMS capacitors to implement low-loss tunable filters [27][28][53][29]. The reported MEMS filters typically show a lower insertion loss compared to their semiconductor-based counterparts [54][55][56], but they are relatively poor in terms of the tunability. On the other hand, filter miniaturization using MEMS elements has not yet been addressed in the literature.

In this chapter, we investigate the possibility of integrating MEMS capacitors in microwave bandpass filter structures, to achieve both miniaturization *and* tunability. Two different methods are used to place MEMS capacitors in transmission-line resonators. The MEMS loaded resonators are then used in different topologies to design miniature and tunable filters, and the performance of these topologies will be discussed in detail. The chapter concludes by a brief study of nonlinearities in the developed MEMS tunable filters. Switched-band filters are briefly discussed in Appendix C.

3.2 Tapped and Distributed Loading of Transmission-Line Resonators

Fig. 3.1a shows a MEMS bridge over a CPW transmission-line. The equivalent T-circuit of this bridge between the two reference planes (dashed lines) is shown in

Fig. 3.1b [57]. The finite width of the bridge (w) and the current path over the bridge result in a phase delay which is taken into account by adding certain line lengths $(w + \Delta l)/2$ to the model. The bridge inductance (L) is around 10 pH, and when the frequency of operation is far below the self resonance of the bridge one may absorb its reactive effects in C. A simple MEMS varactor may be obtained by applying a bias voltage V_b between the bridge and the center conductor of the CPW line. The minimum value of C will correspond to $V_b = 0$ and is referred to as the up-state capacitance (C_{up}). For flat bridges, the theoretical maximum value of C is equal to $1.5C_{up}$ which is reached at the boundary of the mechanical instability under an electrostatic force [58].

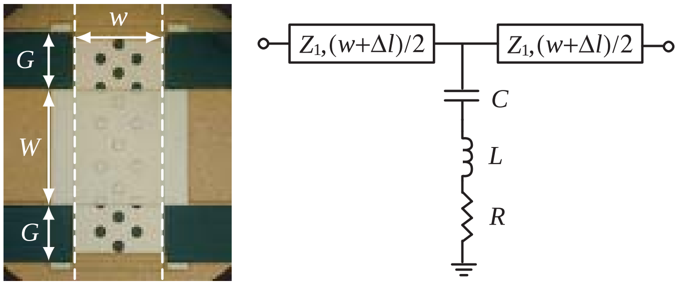

(a) (b)

Figure 3.1: MEMS varactor over a CPW line; (a) photograph: dashed lines show the reference planes, (b) circuit model.

At least two approaches may be imagined for loading CPW resonators using MEMS varactors. In the first approach, MEMS varactors are simply added to the transmission line resonators as localized shunt loads. Figs. 3.2 and 3.3 show how the shunt MEMS bridges can be used to load open- and short-ended half-wave transmission line resonators, respectively. To retain a symmetrical voltage distribution over the resonators, the shunt bridges are used in symmetrical pairs. The amount of loading is determined by the bridge capacitance as well as the loading location. The effect of loading is maximum at the peaks of the voltage distribution, and is zero at the nulls of the voltage distribution. In the open-ended resonator, therefore, loading is the most effective at the end points, while in the short-ended resonator it is more effective in the middle.

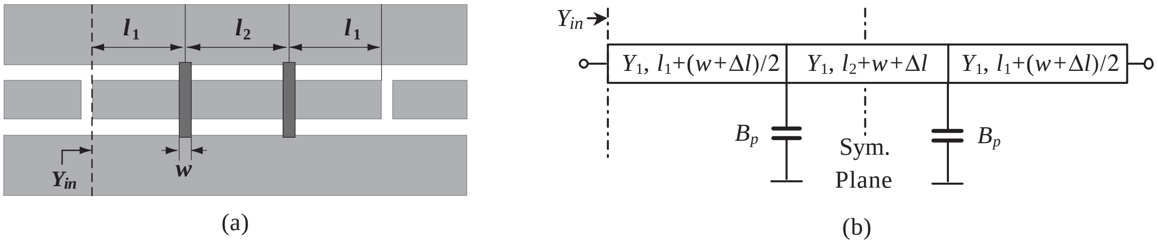

(a)

(b)

Figure 3.2: Taped loading of the open-ended half-wave resonators; (a) layout, (b) circuit model.

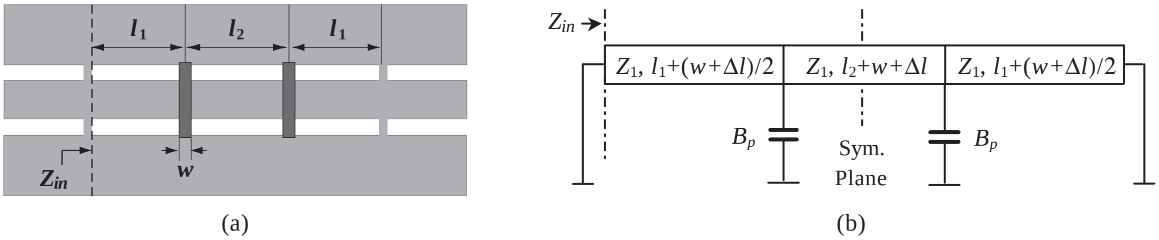

(a)

(b)

Figure 3.3: Taped loading of the short-ended half-wave resonator; (a) layout, (b) circuit model.

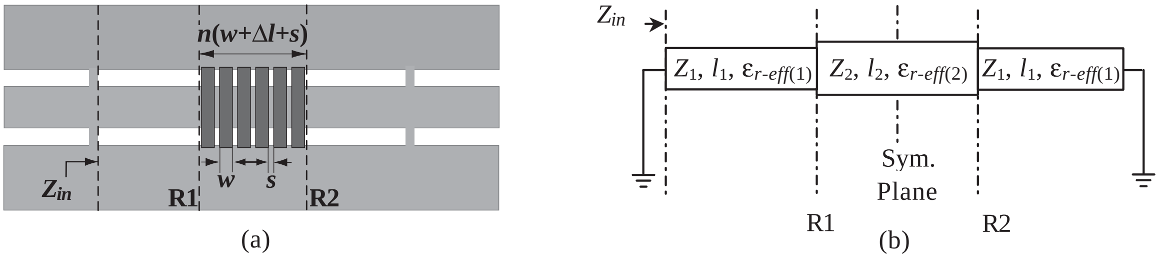

(a)

(b)

Figure 3.4: MEMS slow-wave resonator; (a) short-ended half-wave resonator with $n = 6$ bridges, (b) circuit model.

In the second approach, the MEMS bridges are used to modify the transmission line structure in a distributed fashion. An array of MEMS capacitive bridges is used to periodically load a portion of a CPW resonator and form a slow-wave structure with a high effective dielectric constant and a low characteristic impedance. A short-ended half-wave CPW resonator with this kind of loading is shown in Fig. 3.4a. The loaded section may be modeled by cascading the T-equivalent networks of the bridges and the intermittent line segments, or by using a simple loaded line model as proposed in [59]. In the latter case, the circuit model is presented in Fig. 3.4b, which is much simpler for design purposes. In this model, Z_1 and $\varepsilon_{r-eff(1)}$ are the characteristic impedance and effective dielectric constant of the unloaded CPW line. If C is the bridge capacitance, n is the number of bridges, and s is the edge-to-edge separation between the bridges, then l_2, Z_2 and $\varepsilon_{r-eff(2)}$ of the loaded section are given by:

$$\begin{aligned} l_2 &= n\left(s + w + \Delta\, l\right), \\ Z_2 &= Z_1/\sqrt{K}, \\ \varepsilon_{r-eff(2)} &= K\ \varepsilon_{r-eff(1)}; \end{aligned} \tag{3.1}$$

where:

$$K = 1 + \frac{cZ_1C}{(s+w+\Delta l)\sqrt{\varepsilon_{r-eff(1)}}}, \qquad c = 3\times 10^8 \text{ m/sec.} \tag{3.2}$$

One should notice that the loading period is defined to include the equivalent bridge widths $w + \Delta l$, as well as the edge-to-edge separation between adjacent bridges, s. In a practical design K can be quite large (20-50).

Open-ended slow-wave MEMS resonators are not considered here as their loading at the center portion is less effective due to the voltage null. Also they cannot be loaded in the end portions due to practical access concerns.

3.3 Design Equations for the Loaded Resonators

In this section, we obtain the design equations for the open- and short-ended resonators. These include the resonance condition and the slope parameters.

3.3.1 Open-Ended Resonator with Tapped Loading

The circuit model for the open-ended resonator with tapped loading is shown in Fig. 3.2b. Due to the symmetry of the structure and the fact that the first resonance has a voltage null at the center, one can use half of this model to obtain the resonance condition. If B_p represents the total equivalent shunt susceptance (in this case that of the MEMS bridge), neglecting the losses in the transmission line and the bridge, the input admittance of the half circuit is given by:

$$\overline{Y}'_{in} = j\overline{B}'_{in} = j\frac{\overline{B}_p - \cot\theta_2 + \tan\theta_1}{1 - \tan\theta_1(\overline{B}_p - \cot\theta_2)} \tag{3.3}$$

where θ_1 and θ_2 are the electrical lengths corresponding to $l'_1 = l_1 + (w + \Delta l)/2$ and $l'_2 = (l_2 + w + \Delta l)/2$, respectively, the bar sign indicates normalization to the CPW line characteristic admittance Y_1, and the prime sign refers to the half circuit. Recognizing that the first resonance mode is a parallel-type resonance at the input, the resonance condition then may be obtained by forcing $\overline{B}_{in}$ to zero:

$$\overline{B}_p - \cot\theta_2 + \tan\theta_1 = 0. \tag{3.4}$$

This equation may be used to determine the required value of the bridge capacitance at a given position that produces a resonance at a given frequency ω_0. Another quantity of interest for a filter designer is the susceptance slope parameter of the resonator, $\overline{b}_{in}$, which for resonance at ω_0 is defined as [60]:

$$\overline{b} = \frac{\omega_0}{2}\frac{\partial\overline{B}_{in}}{\partial\omega}\Bigg|_{\omega=\omega_0} . \tag{3.5}$$

The susceptance slope may be calculated using the half circuit input susceptance in (3.3) and the resonance condition in (3.4) to give the following expression:

$$\overline{b} = 2\overline{b}' = \omega_0\frac{\partial\overline{B}'_{in}}{\partial\omega}\Bigg|_{\omega=\omega_0} = \theta_1 + \cos^2\theta_1\left(\overline{B}_p + \theta_2\csc^2\theta_2\right). \tag{3.6}$$

In this derivation, we assumed that B_p is predominantly capacitive and ignored the dispersion effects in the transmission line.

3.3.2 Short-Ended Resonator with Tapped Loading

Similarly, one can derive expressions for the resonance condition and reactance slope when the bridges are used in a short-ended half-wave resonator. In this case, the half circuit is obtained by defining a magnetic wall at the symmetry plane in the model of Fig. 3.3b. The normalized input impedance of the half circuit is given by:

$$\overline{Z}'_{in} = j\overline{X}'_{in} = j\frac{\overline{B}_p + \tan\theta_2 - \cot\theta_1}{1 + \cot\theta_1(\overline{B}_p + \tan\theta_2)} \tag{3.7}$$

where θ_1 and θ_2 are defined similar to the case of the open-ended resonator. The short-ended resonator forms a series resonance at the input and the corresponding resonance condition is obtained by forcing $\overline{X}_{in} = 0$:

$$\overline{B}_p + \tan\theta_2 - \cot\theta_1 = 0. \tag{3.8}$$

The slope parameter of interest for this type of resonator is the reactance slope, which is defined similar to (3.5), and may be expressed as:

$$\overline{x} = 2\overline{x}' = \omega_0 \frac{\partial \overline{X}'_{in}}{\partial\omega}\Bigg|_{\omega = \omega_0} = \theta_1 + \sin^2\theta_1 \left(\overline{B}_p + \theta_2 \sec^2\theta_2\right). \tag{3.9}$$

3.3.3 Short-Ended Resonator with Distributed Loading

The design equations for the short-ended slow-wave MEMS resonator in Fig. 3.4 are derived by replacing the symmetry plane with a magnetic wall in the circuit model. For the resulting half circuit we obtain:

$$\overline{Z}'_{in} = j\overline{X}'_{in} = j\frac{\tan\theta_1 - \overline{Z}_2\cot\theta_2}{1 + \overline{Z}_2\tan\theta_1\cot\theta_2} \tag{3.10}$$

where θ_1 and θ_2 are the electrical lengths corresponding to l_1 and $l_2/2$, respectively. As before, the prime sign refers to the half circuit and the bar sign indicates normalization to the characteristic impedance of the unloaded transmission line, Z_1. The corresponding resonance condition is expressed by:

$$\tan\theta_1 - \overline{Z}_2 \cot\theta_2 = 0 \tag{3.11}$$

and the reactance slope of this resonator is given by:

$$\overline{x} = 2\overline{x}' = \omega_0 \frac{\partial \overline{X}'_{in}}{\partial \omega}\Bigg|_{\omega\,=\,\omega_0} = \theta_1 + \overline{Z}_2\ \theta_2\ \cos^2\theta_1\ \csc^2\theta_2. \tag{3.12}$$

Equations (3.11) and (3.12) form the basis for design of filters using slow-wave MEMS resonators.

3.4 Bandpass Filters and Inverter Design

Bandpass filters may be obtained through a ladder combination of series and parallel resonators. Alternatively, they may be obtained by combining only one type of resonators through impedance inverters [60]. Impedance inverters are the circuit representation of the coupling as a two-port network, and have the property that transform a series resonance in their input to a parallel resonance in the output and vise versa. The two possible 3-pole bandpass filter topologies based on series or parallel resonators and inverters are shown in Fig. 3.5, where $K_{i,i+1}$ and $J_{i,i+1}$ are the impedance and admittance inversion ratios, respectively.

Although the K- and J-inverters are principally similar in terms of their circuit function, their physical implementation is usually different. The series resonators are generally coupled through the magnetic field, while for the parallel resonators, the most effective way of coupling is through the electric field. These different coupling mechanisms lead to the design of inductive and capacitive impedance inverters.

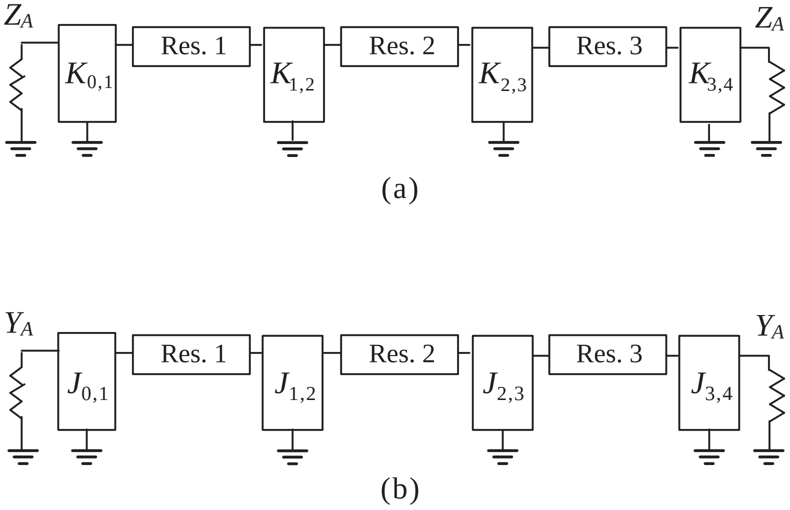

Figure 3.5: 3-pole end-coupled transmission-line filter using (a) series-type resonators and inductive inverters, (b) parallel-type resonators and capacitive inverters.

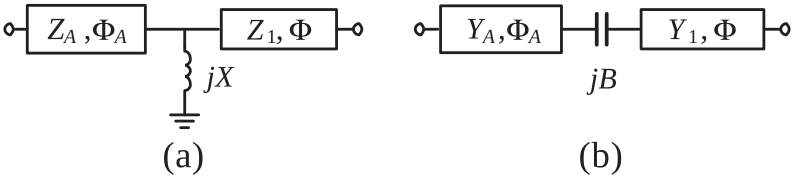

Figure 3.6: Circuit realization of inverters; (a) K-inverter using shunt inductor, (b) J-inverter using series capacitor.

Inductive and capacitive inverters are also referred to as $K-$ and $J-$inverters, respectively. Simple realizations of the inductive and capacitive couplings, that are suitable for use with the transmission line resonators, are shown in Fig. 3.6. The circuits presented in Fig. 3.6 have asymmetrical input-output arms and are more general than the symmetrical types commonly encountered in the filter design textbooks [60][61]. Design equations for the inductive inverter of Fig. 3.6a may be obtained as follows:

$$\begin{aligned}
&\overline{X} = \left[\left(\overline{K}^2 - 1\right)\overline{Z}_A^{-2} + \left(\overline{K}^{-2} - 1\right)\right]^{-\frac{1}{2}} \\
&\Phi_A = (p+q)/2 \\
&\Phi = (p-q)/2; \\
&p = -\tan^{-1}\left(\left(\overline{Z}_A^{-1} + 1\right)\overline{X}\right) \\
&q = -\tan^{-1}\left(\left(\overline{Z}_A^{-1} - 1\right)\overline{X}\right)
\end{aligned} \tag{3.13}$$

where $\overline{Z}_A$ is the characteristic impedance of the input/output transmission line and the bar sign indicates normalization to the unloaded CPW line, Z_1. For $\overline{Z}_A = 1$, these equations reduce to the standard formulas in [60]. The inverse formula for K versus the physical parameters of the inductive inverter can be written as:

$$\overline{K} = -\frac{\overline{Z}_A}{2\overline{X}}\left[\frac{1}{\cos p} - \frac{1}{\cos q}\right]. \tag{3.14}$$

As the capacitive inverter in Figs. 3.6a and 3.6b are dual of each other, the design equations for $J-$inverter can simply be obtained from those of the $K-$inverter by using duality:

$$\begin{aligned}
&\overline{B} = \left[\left(\overline{J}^2 - 1\right)\overline{Y}_A^{-2} + \left(\overline{J}^{-2} - 1\right)\right]^{-\frac{1}{2}} \\
&\Phi_A = (p+q)/2 \\
&\Phi = (p-q)/2; \\
&p = -\tan^{-1}\left(\left(\overline{Y}_A^{-1} + 1\right)\overline{B}\right) \\
&q = -\tan^{-1}\left(\left(\overline{Y}_A^{-1} - 1\right)\overline{B}\right).
\end{aligned} \tag{3.15}$$

Also:

$$\overline{J} = -\frac{\overline{Y}_A}{2\overline{B}}\left[\frac{1}{\cos p} - \frac{1}{\cos q}\right]. \tag{3.16}$$

3.5 MEMS Tunable Filters with Tapped Varactor Loading

To tune a bandpass filter, one needs to tune all the resonators by changing the loading capacitance. However, this should not affect the coupling mechanism in an uncontrolled way. The best scenario is to use a topology which implements the couplings in a localized form instead of a topology with a distributed coupling. A suitable choice is the end-coupled half-wave resonator filter. The end-coupled topology has two advantages: (i) unlike the more compact topologies such as combline or interdigital, it provides easy access to each resonator and enough room to integrate the MEMS bridges and their associated pull-down electrodes and bias lines, and (ii) the inter-resonator as well as input/ouput couplings are achieved through capacitive or inductive inverters, and not directly affected by the tuning of the resonators. In this section, we present two basic types of such tunable filters based on open- and short-ended resonators with tapped capacitive loading.

3.5.1 Filters with Capacitive Inverters

The first tunable filter design studied in this chapter is a 3-pole topology based on the open-ended CPW resonator and capacitive inverters. The resonators are of the type shown in Fig. 3.2, and are fabricated using 3 μm thick electroplated gold CPW lines with dimensions of 80/160/80 μm ($G/W/G$) on a 500 μm-thick quartz substrate with $\varepsilon_r = 3.8$ and $\tan\delta = 0.0002$. The dimensions of the CPW line are chosen to minimize the conductor losses, as per reference [62]. The measured CPW line parameters are $Z_1 = 77\ \Omega$, $\varepsilon_{r-eff(1)} = 2.37$, and the attenuation constant is $\alpha_1 = 0.34 - 0.37$ dB/cm in the 20-24 GHz range. The corresponding transmission-line Q is 80-90 at this frequency range.

At the upper band center frequency ($f = f_{0,up}$), the length of the resonators and the location and up-state capacitance of the loading MEMS bridges are related through (3.4). To maximize the tuning range, it is desirable to maximize the absolute capacitance change $\Delta C = C_{max} - C_{up}$, by increasing the bridge width, w. However, due to the practical fabrication limitations, the bridges width is limited to $120 - 140$ μm, which presents a major constraint. The tuning range may be somewhat enhanced by moving the loading varactors towards the open ends of the resonator. But the location of the bridges also cannot be chosen arbitrarily close to the end points, since θ_1 should be large enough to present a positive length after subtracting the negative lengths of the inverter arms (see Fig. 3.7). As the required values of the input/output coupling are generally larger than the inter-resonator couplings, the input/outout inverters have larger inverter ratios and longer negative arms, resulting in a more severe limitation for the first and last resonators. Therefore, it proves to be difficult to obtain a considerable tuning by using simple MEMS varactors in tapped resonators.

g_0	g_1	g_2	g_3	g_4
1	0.879	1.113	0.879	1

Table 3.1: Chebyshev filter coefficients for a 3-pole response with 0.05 dB pass-band ripple.

In the next step, three of such tunable resonators are combined to form a tunable filter. The normalized Chebyshev filter coefficients for a pass-band ripple of 0.05 dB are given in Table 3.1. For the terminating source and load resistances of $Z_A = 1/Y_A = 50\ \Omega$ and a factional bandwidth of $w = 9\%$, the required values of inverter ratios are calculated using the standard formulas given in [60]:

$$\begin{aligned} \overline{J}_{0,1} = \overline{J}_{3,4} &= \sqrt{\frac{w\overline{Y}_A\overline{b}}{g_1}} \\ \overline{J}_{1,2} = \overline{J}_{2,3} &= \frac{w\overline{b}}{g_2} \end{aligned} \tag{3.17}$$

in which $\overline{b}$ represents the normalized susceptance slope of the resonators and is calculated using (3.6). The J-inverters are realized as shown in Fig. 3.6b, with the parameters obtained from (3.15).

The complete circuit model of the 3-pole filter is obtained by combing those of the resonators and the J-inverters, as shown in Fig. 3.7. Based on this model, the filter is designed for the center frequency of $f_{0,up}$. A design algorithm may be outlined as the following steps:

1. Choose the width of the MEMS bridges and calculate C_{up} for the varactors (using simple formulas or by simulation) and the corresponding loading susceptance B_p (the series bridge resistance R is neglected in the design stage).
2. Choose the distance between the loading varactors and calculate θ_2.
3. Using the values of B_p and θ_2, calculate θ_1 from (3.4).
4. Calculate the slope parameter $\overline{b}$ from (3.6), the required values of J-inverters from (3.17), and the physical parameters of the capacitive inverters from (3.15).
5. If the resulting $\theta_1 + \Phi_{0,1}$ is negative or too small to be physically implemented, go back to step 2, reduce the loading separation, and repeat the steps.

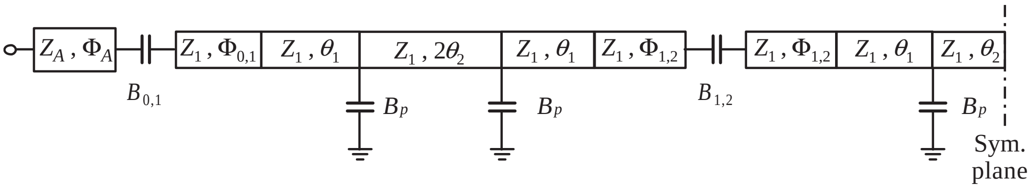

Figure 3.7: The complete circuit model for the tunable filter with capacitive inverters (only one half of the circuit is shown).

This algorithm has been used to design a 9% filter at $f_{0,up} = 24$ GHz, for the presumed value of $C_{up} = 130$ fF. This value is based on the 130 μm-wide bridges

$Z_A(\Omega)$	50	$C_{0,1} = C_{3,4}$ (fF)	89
$Z_1(\Omega)$	77	$C_{1,2} = C_{2,3}$ (fF)	25
C_{up} (fF)	130	$\Phi_{0,1} = \Phi_{3,4}$ (deg.)	-40.0
θ_1 (deg.)	44.0	$\Phi_{1,2} = \Phi_{2,3}$ (deg.)	-15.1
θ_2 (deg.)	22.0	Φ_A (deg.)	-19.9

Table 3.2: Model parameters for the 21.7-24.0 GHz 3-pole tunable filter.

with an average height of 1.5-1.6 μm in the up state ($W = 160$ μm, $w = 130$ μm, and $g_0 = 1.5 - 1.6$ μm). The designed values of model parameters are given in Table 3.2, where the loading and coupling capacitors are shown with their physical values instead of their susceptance. The simulated S-parameters are shown in Fig. 3.8 for bridge capacitances of 130 fF (expected up-state value) and 180 fF (a theoretical biased value). The value of $C = 180$ fF for the lower band is the minimum required for two adjacent band tuning (non overlapping pass bands in the upper and lower bands). This is corresponding to $C_{max} = 1.38\ Cup$, which is the limit of what can be achieved using flat bridge varactors.

The physical layout of the tunable filter can also be obtained from the circuit model of Fig. 3.7. The series coupling capacitors are implemented as MAM (metal-air-metal) or interdigitated capacitors, depending on the required capacitance. The dimensions of these capacitors are determined using 2.5D moment-method EM simulators such as Momentum [39] or Sonnet [63]. Due to the existence of the shunt parasitic capacitors between the center conductor and the CPW ground, this implementations introduce a π combination instead a simple series capacitor. It is convenient to model these shunt parasitics as equivalent transmission-line lengths ($\Delta\Phi_x$), and include them in the length of the inverter arms Φ_x (see Appendix B). The physical lengths of the transmission-line sections are then calculated using measured or simulated $\varepsilon_{r_{eff(1)}}$ and the complete layout is obtained by cascading the individual parts. A final moment-method simulation can be performed to verify the design. The final full-wave analysis,

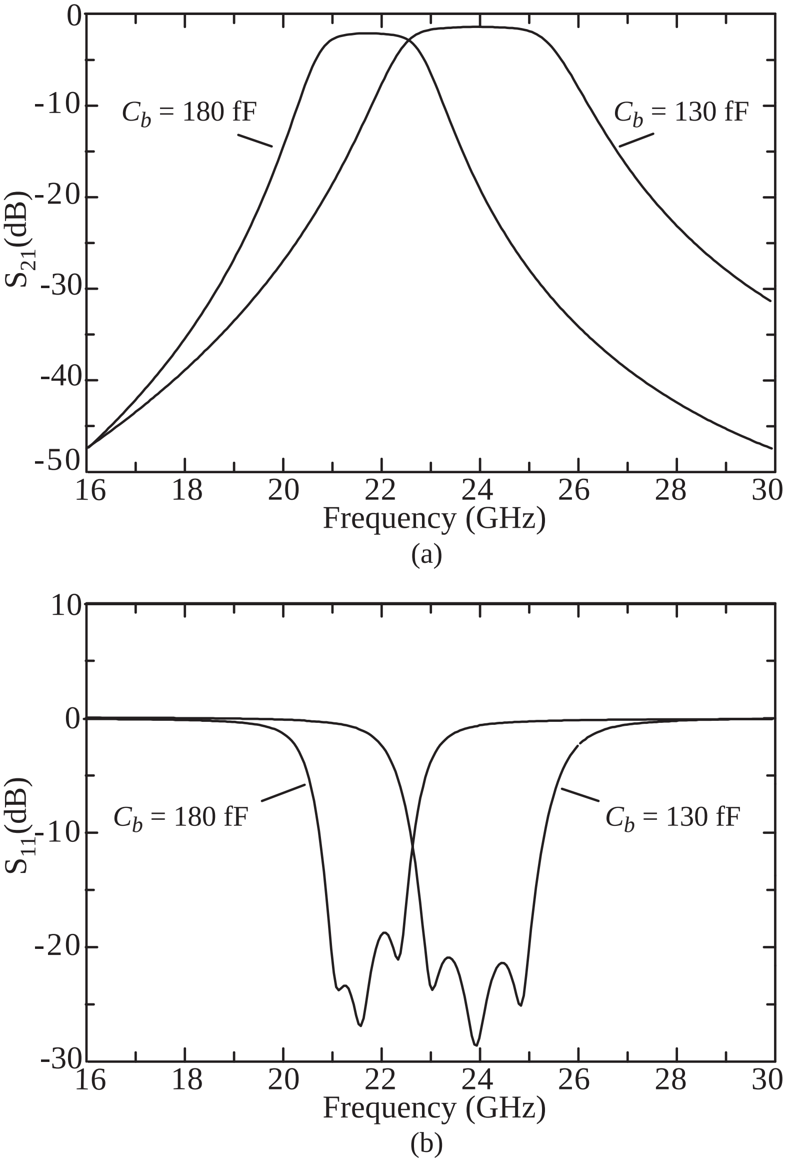

Figure 3.8: Simulated S-parameters of the capacitively-coupled tunable 3-pole filter.

however, does not prove more accurate than the circuit model simulation, and can be omitted from the design procedure.

The MEMS bridges are fabricated using 0.9 μm sputtered gold membranes. The fabrication process is straightforward and similar to standard CPW shunt switches, as explained in [64] and [65]. A photograph of the fabricated filter is shown in Fig. 3.9. To minimize the effect of the biasing circuitry, the control voltage is applied through

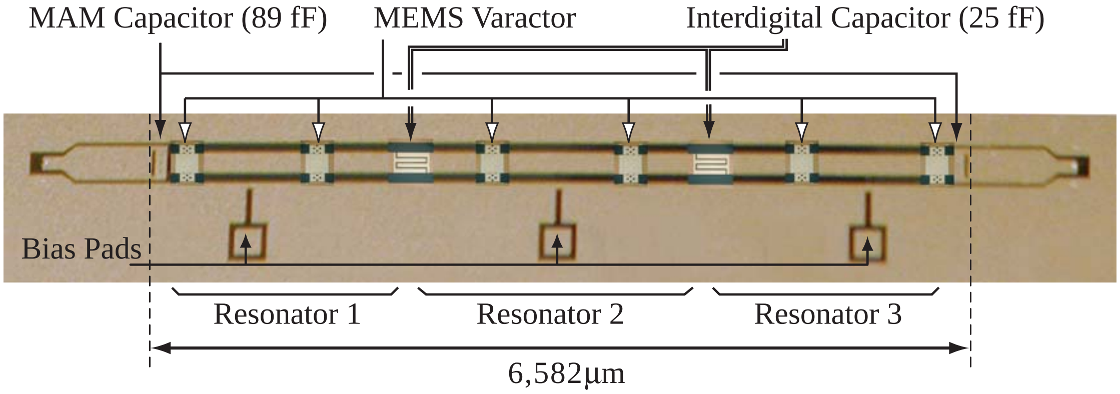

Figure 3.9: Photograph of the fabricated CPW tunable filter on a quartz substrate.

the bias lines that are made of high resistivity SiCr (1000-2000 Ω/square), and are connected to the CPW center conductor at the center of the resonators which has the minimum RF voltage. The filter is measured using on-wafer techniques in a 50 Ω system. The input/output lines are then de-embedded using a TRL calibration to obtain the S-parameters between the reference planes shown in Fig. 3.9. By applying a DC voltage of $V_b = 0 - 15$ V, this filter is tuned from 23.8 GHz to 22.6 GHz. The measured S-parameters for these two values of bias voltage are shown in Fig. 3.10. The mid-band insertion loss varies from 2.85 dB to 3.5 dB, and the fractional bandwidth varies from 8.4% to 6.6%, between the upper and lower bands of operation. The bumps in the measured S_{21} curves at 20 GHz are believed to be due the loading effect of bias circuitary[1]. This was verified by measuring the filter with the bias pads left disconnected, which resulted an undistorted response.

In Fig. 3.10 we have also included the fitted simulation values which are based on the model in Fig. 3.7 with the modified values of $C = 142$ and 166 fF and $R = 0.3$ Ω. Also we have added 500 Ω shunt resistors at the center of the resonators to account for the RF loading of the bias lines. The actual height of the bridge in the up and

---

[1] In the original layout, the bias pads were connected to the center conductor of the resonators using high-resistivity SiCr bias lines. In the fabricated sample, however, these bias lines were damaged and had to be replaced by conductive wire-bonds.

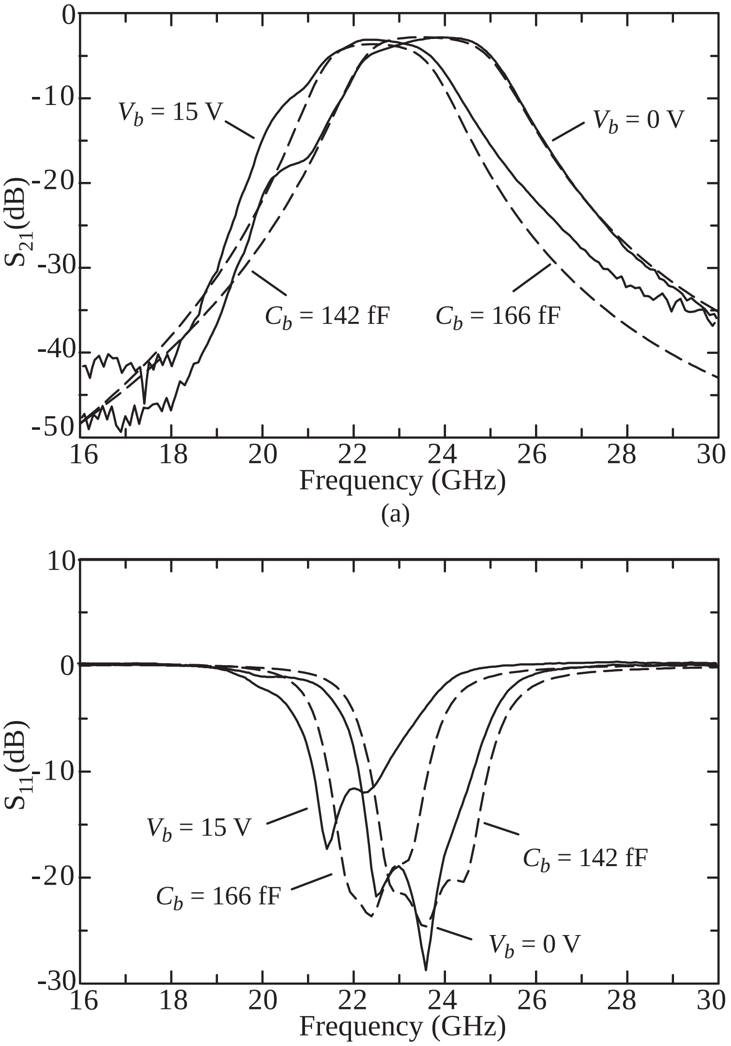

(a)

(b)

Figure 3.10: S-parameters of the capacitively-coupled tunable 3-pole filter. Solid lines show measured values for $V_b = 0$ and 15 V, and dashed lines show the simulations based on the fitted values of C and R.

biased states, as well as its approximate quality factor, can be calculated from the fitted values of C and R. This calculation results in a height of $g = 1.40 - 1.19$ μm for $V_b = 0 - 15$ V, and a varactor Q of 160-140 in the tuning range. The dB value of the mid-band insertion loss of the filter, IL, may be calculated from the following formula [60]:

$$IL = 4.343 \frac{\sum g_i}{w \cdot Q} \tag{3.18}$$

where g_i's are the prototype filter coefficients, w is the fractional bandwidth, and Q is the unloaded-Q of the resonators. For the filter coefficients in Table 3.1, this can be rewritten as:

$$Q = \frac{12.45}{w \cdot IL} \tag{3.19}$$

which is used to estimate the overall resonator Q based on the filter measurements. Based on this formula, a Q of ~ 50 is calculated for the open-ended CPW resonator with tapped varactor loads, in the tuning range. However, this calculation attributes all of the losses, including that of the inductive inverters, to the resonators, and therefore results in Q values which are lower than actual. The real value of the resonator Q is expected to be in the range of 70-80, which is comparable to that of an unloaded CPW resonator (80-90 at 23 GHz). The filter data are summarized in Table 3.3.

Bias Voltage (V)	0	15
Center Frequency (GHz)	23.8	22.6
Bandwidth 1-dB (%)	8.4	6.6
Insertion Loss (dB)	-2.85	-3.85
Av. Bridge Height* (μm)	1.40	1.19
Bridge Capacitance* (fF)	142	166
Bridge Resistance* (Ω)	0.3	0.3
Varactor Q* (@ center frequency)	157	140

* Fitted values based on measurements.

Table 3.3: Measured parameters of the capacitively-coupled tunable 3-pole filter.

3.5.2 Filters with Inductive Inverters

Studying the behavior of the capacitively-coupled filter reveals that the bandwidth, mid-band insertion loss, and the shape of the frequency response strongly vary with tuning in these filters. This is of course an undesirable effect that cannot be tolerated in most practical applications. The strong sensitivity to tuning stems from the fact that the resonance slope parameters and the inverter coefficients vary in different directions upon tuning. For example, increasing the bridge capacitor results in a lower resonance frequency which lowers $B_{i,i+1}$ and the inverter coefficients $J_{i,i+1}$ according to (3.15), while it increases b_i's (makes the resonators more capacitive). The result is reduction in the bandwidth and variation of the filter coefficients according to (3.17).

To avoid strong variations with tuning, the resonators and inverters have to be designed in such a way that their variations compensate each other. A primary requirement then would be to use designs with different types of loading and coupling. This means that the resonators with capacitive loading should be coupled using inductive inverters, and the resonators with inductive loading should be coupled using capacitive inverters. In this context, for the varactor-tuned resonators, the preferred type of coupling is inductive, which also implies using short-ended type of resonators (Fig. 3.3). Furthermore, to achieve an ideal tunable design, it is shown that the resonators have to be designed (or coupled) asymmetrically [66]. But this latter condition may be ignored in most practical applications.

The circuit model for an inductively-coupled tunable filter based on the previously developed varactors is shown in Fig. 3.11. The values of the inductive inverters are determined from the following standard formulas [60]:

$$\begin{aligned} \overline{K}_{0,1} = \overline{K}_{3,4} &= \sqrt{\frac{w\overline{Z}_A\overline{x}}{g_1}} \\ \overline{K}_{1,2} = \overline{K}_{2,3} &= \frac{w\overline{x}}{g_2} \end{aligned} \tag{3.20}$$

in which $\overline{x}$ represents the normalized reactance slope of the resonators, calculated from (3.9). The $K-$inverters are of the type shown in Fig. 3.6a.

The design steps are similar to those of the capacitive filter, except that the equations (3.8), (3.9), (3.20), and (3.13) are used instead of (3.4), (3.6), (3.17), and (3.15). Furthermore, by a proper choice of θ_2, the inductively-coupled design can be optimized for a constant absolute or fractional bandwidth. For a given design with fixed values of coupling inductors, the inverter ratios are calculated from (3.14), at each frequency point in the tuning range. Having the values of K, equations (3.20) can be used to calculate the required values of the resonator slope parameters $\overline{x}$ that result in a constant bandwidth, at several points in the tuning range. The difference between these required values and the actual slope parameters calculated from (3.9) is a measure of bandwidth variations, and can be used to determine the optimal values of θ_2 which minimizes these effects.

We have used the above procedure to design a 5% bandpass filter at 24 GHz. The previously extracted value of 142 fF has been used for C_{up} in this design, and θ_2 has been chosen to minimize variations of the *absolute* bandwidth, in a 10-15% tuning range. The designed model parameters are given in Table 3.4.

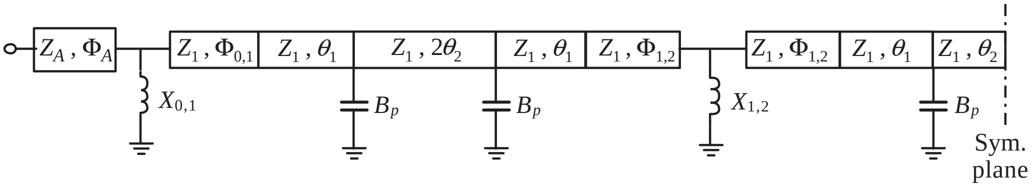

Figure 3.11: The complete circuit model for the tunable filter with inductive inverters (only one half of the circuit is shown).

The simulated S-parameters have been shown in Fig. 3.12 for three values of bridge capacitance: C = 142, 177, and 217 fF. The series resistance R has been neglected in this simulations, but an attenuation constant of 0.37 dB/cm is included the transmission-line models (from previous measurements). The center frequency,

$Z_A(\Omega)$	50	$L_{0,1} = L_{3,4}$ (pH)	89
$Z_1(\Omega)$	77	$L_{1,2} = L_{2,3}$ (pH)	19
C_{up} (fF)	130	$\Phi_{0,1} = \Phi_{3,4}$ (deg.)	-9.3
θ_1 (deg.)	18.0	$\Phi_{1,2} = \Phi_{2,3}$ (deg.)	-2.2
θ_2 (deg.)	55.0	Φ_A (deg.)	-14.7

Table 3.4: Model parameters for the 22.9-25.1 GHz 3-pole filter with a tunable bandwidth of 1.3 GHz.

absolute bandwidth, and the mid-band insertion loss of the filter for these values of C are listed in Table 3.5. It is observed that the pass-band can be tuned over a 10% band width (three adjacent bands), with a constant bandwidth and no significant variation in the shape of the pass-band response (notice that the pass-band return loss changes less than 3 dB with tuning). Although the required capacitance ratio for 10% tuning is too high to be realized using a simple flat profile MEMS varactor, the inductively-coupled design shows the interesting property that it can preserve the shape of the response over the tuning range. Also, as a direct consequence of this property, the mid-band insertion loss does not vary significantly with tuning. An even better compensation is possible if the separation between loads is chosen differently in the middle resonator and the end resonators. But this requires different values of bridge capacitance at any given frequency, which means two different control voltages in general.

Bridge Capacitance (fF)	142	177	217
Center Frequency (GHz)	24.1	22.9	21.7
Bandwidth 1-dB (GHz)	1.27	1.28	1.29
Insertion Loss (dB)	2.42	2.36	2.34

Table 3.5: Simulated parameters of the inductively-coupled 3-pole filter with a 1.3 GHz tunable bandwidth using ideal varactors and a transmission-line Q of 90 at 24 GHz.

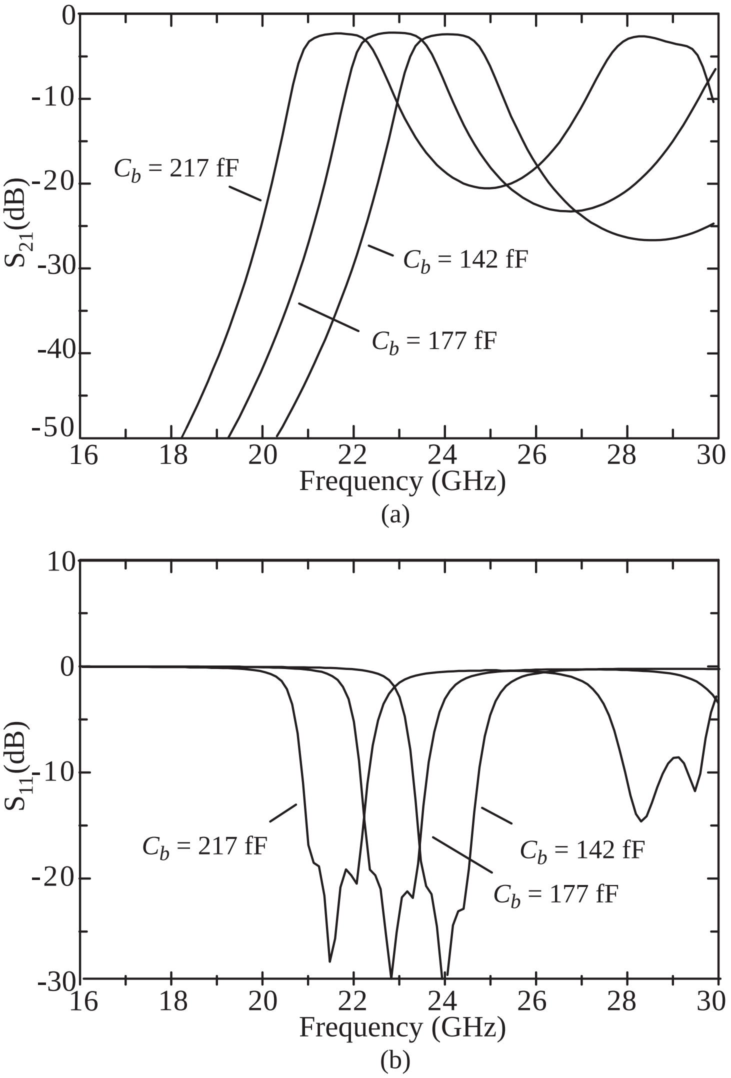

Figure 3.12: Simulated S-parameters for the inductively-coupled tunable 3-pole filter.

An important drawback of the inductively couples design is the existence of a very close second pass-band that drastically reduces the upper band rejection of the filter. This is due to the resonance between the inductive inverters and the resonators which show a capacitive behavior above the the fundamental resonant frequency. The second pass-band increasingly approaches the lower frequencies when the filter is tuned down, resulting an unacceptably poor rejection. This is a major limitation that makes the inductively-coupled design a non-practical option in spite of its otherwise nice behavior. In the next section, we present inductively-coupled tunable filters with distributed capacitive loading, which circumvent this difficulty.

3.6 Distributed Designs

As was mentioned in Section 3.2, MEMS varactors can be used to periodically load a portion of the CPW resonators and form compact slow-wave resonant structures. Due to the large number of varactors, this type of resonators show a higher tunability as compared to the resonators with tapped loading. Also the short-ended slow-wave resonators are suitable for the inductively-coupled filter, which has a well-behaved tuning. In this section, we discuss the principle of operation and the performance of the Slow-Wave MEMS Resonators (SWMR) and the miniature and tunable filters composed of these resonators.

3.6.1 Slow-Wave MEMS Resonator

The circuit model and the governing equations for the short-ended resonator with distributed loading were presented in Fig. 3.4 and (3.1) and (3.2). Due to the low phase velocity in the loaded section, this section forms a slow-wave section. The complete resonant structure is referred to as the Slow-Wave MEMS Resonator. Equation (3.11) expresses the resonance condition for this type of resonator. Starting with a given size and number of the MEMS bridges, one can use (3.11) to obtain the length of the unloaded sections for resonant at a the desired frequency. The design procedure is described below:

1. Choose the width of the MEMS bridges w, and determine values of C and Δl for the MEMS capacitors using EM simulation.

2. Choose the number of bridges n and the edge-to-edge separation s.

3. Using (3.1) and (3.2), calculate the loading factor K, Z_2, l_2 and θ_2 at the center

frequency.

4. Calculate θ_1 from (3.11).

Partial loading of the CPW resonator around the voltage maximum proves to be very effective in reducing the resonance length. There are two different effects involved in miniaturization: (i) the slow phase velocity over the loaded region, and (ii) the step impedance configuration. The larger number of bridges results in a more compact resonator, but at the same time it can reduce the quality factor (due to the finite Q of the bridge capacitors). Table 3.6 provides a quantitative comparison between two slow-wave MEMS resonators with 6 and 8 MEMS bridges, and a standard short-ended CPW resonator. All resonators are based on 3 μm thick electroplated gold with dimensions of 80/160/80 μm (G/W/G) on a 500 μm-thick quartz wafer with $\varepsilon_r = 3.8$ and $\tan\delta = 0.0001$. The dimensions of the CPW line are chosen to minimize the conductor losses, as per [62]. The measured CPW line parameters are $Z_1 = 77\ \Omega$, $\varepsilon_{r-eff(1)} = 2.37$, and the attenuation constant is $\alpha_1 = 0.37$ dB/cm at 21 GHz. The MEMS bridges are fabricated using electroplated gold membranes at an average height of 1.1 μm above the center conductor of the CPW line ($w = 50\ \mu$m, $s = 20\ \mu$m). The simulated values [39] of C and Δl are 74 fF and $-20\ \mu$m, respectively, which corresponds to $K = 23.2$ according to (3.2).

The measured unloaded Q's and the lengths of the resonators are given in Table 3.6. These values also include losses from the input/output coupling inductors in the test structure (see Fig. 3.4). Nevertheless, they help in understanding the effect of loading on the resonator Q. The lengths are normalized to the guided wavelength of the unloaded CPW line at the respective resonance frequencies. The slow-wave resonators are more than 3 times shorter than the standard resonator and show considerable miniaturization. This situation generally entails a much smaller quality factor. However, the MEMS capacitors used in this case are high-Q elements with an estimated Q of ~350-500 at 21 GHz ($R \approx 0.25\pm0.05\ \Omega$) [67], and the loading of the resonator reduces Q by only 10-20%.

Resonator Type	f_0 (GHz)	Length (λ_g@f_0)	Resonator Q	MEMS Bridge Q*
Standard	24.3	0.5	62	–
w/ 6-bridge loading	21.0	0.163	56	400
w/ 8-bridge loading	21.0	0.145	48	400

* Extracted value using model.

Table 3.6: Measured parameters of the standard and loaded transmission-line resonators. No bias lines presnt in this structure.

3.6.2 MEMS Miniature Filter

A bandpass filter may be designed by coupling of the slow-wave MEMS resonators through inductive impedance inverters of the type shown in Fig. 3.6a. The design routine is as follows:

1. Design the slow-wave MEMS resonators as described previously.
2. Calculate the reactance slope parameter $\overline{x}$ from (3.12), the inverter coefficients $K_{j,j+1}$ from (3.20), and the physical parameters of the capacitive inverters from (3.15).
3. If the resulting $\theta_1 + \Phi_{0,1}$ is negative or too small to be physically implemented, reduce the length of the loaded region in the resonators and repeat the steps.

In the CPW design, the shunt inductors are realized using narrow inductive lines between the center conductor and the ground plane [68]. For larger values of inductance, the lines are extended inside the ground conductors (see Fig. 3.14), forming short-circuited high-impedance CPW stubs. However, the cuts in the ground conductor introduce parasitic series inductances that are included in the model by adding correction lengths $\Delta\Phi_A$ and $\Delta\Phi$ to the individual arms of the inverters. To avoid anomalies in the asymmetric inductive stubs in the input/output inverters, the ground path is closed using electroplated air-bridges that are formed in the same process along with the MEMS capacitors. Several shunt inductors were individually fabricated and tested and the measured values of inductance for all of the examined cases were 10-20% lower than the predicted values using commercial MoM simulators [39][63] (see Appendix B).

Fig. 3.13 presents the complete circuit model of the miniature filter. This model has been used to design a 3-pole Chebychev filter with 8% equi-ripple bandwidth centered at 21 GHz and 0.05 dB pass-band ripple. The filter is based on the slow-wave MEMS resonators with 6 bridges (Table 3.6). The model parameters for this design are given in Table 3.7. In the physical layout, the unloaded sections of the resonators are adjusted to accommodate the correction lengths of the inductive stubs ($\Delta\Phi_x$).

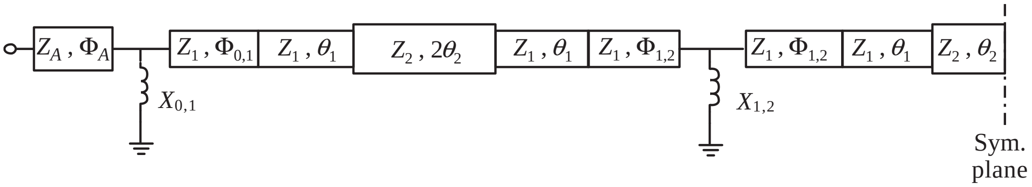

Figure 3.13: The complete circuit model for the miniature 3-pole filter (only one half of the circuit is shown).

The fabricated miniature filter is shown in Fig. 3.14. The total length of the miniature filter is 3620 μm, which is only $0.39\lambda_g$ at 21 GHz ($\lambda_g = 9280$ μm). A standard filter without the bridges would have been 12560 μm long (3.5 times longer). Fig. 3.15 presents the simulated and measured S-parameters of the miniature filter. The measured pass-band is centered at 21.1 GHz. The measured mid-band insertion loss is 2.9 dB vs. the simulated value of 2.3 dB which neglects the loss in the MEMS

$Z_A(\Omega)$	50	$L_{0,1} = L_{3,4}$ (pH)	135
$Z_1(\Omega)$	77	$L_{1,2} = L_{2,3}$ (pH)	36
$Z_2(\Omega)$	15.9	$\Phi_{0,1} = \Phi_{3,4}$ (deg.)	-11.6
θ_1 (deg.)	21.2	$\Phi_{1,2} = \Phi_{2,3}$ (deg.)	-3.5
θ_2 (deg.)	28.0	Φ_A (deg.)	-18.7

Table 3.7: Model parameters for the 21 GHz miniature 8% 3-pole filter with 6-bridge loading per resonator.

capacitors[2]. The 1-dB fractional bandwidth is 8.6%. Further miniaturization may be obtained using more bridges on each resonator at the expense of higher mid-band insertion loss. A second design based on the 8-bridge slow-wave resonators (Table 3.6) resulted in 3.5 dB mid-band insertion loss. This is due to the slightly lower Q of the resonators with longer slow-wave section (see Table 3.6). The measured data for the miniature filters with 6 and 8 bridges per resonator are summarized in Table 3.8.

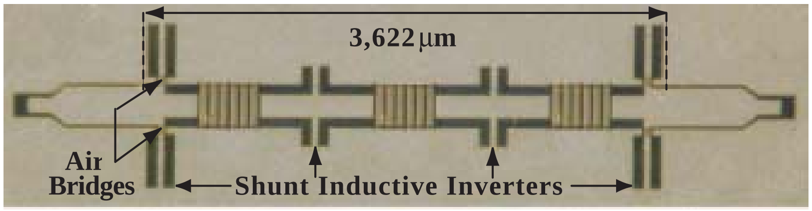

Figure 3.14: Photograph of the fabricated MEMS miniature filter (Design # 1 in Table 3.8).

Although the slow-wave MEMS miniature filter easily achieves a low-loss miniaturization, it suffers from sensitivity to the fabrication errors. With the state of the art technology, the MEMS bridges may be fabricated with ±0.1 μm height variations. The circuit model in Fig. 3.13 may be used to perform a sensitivity analysis vs. the height variations. Table 3.9 shows simulated values of the bridge capacitor, as well

---

[2] Simulations are based on a transmission-line Q of 80 at 21 GHz, and include the losses in the coupling inductors.

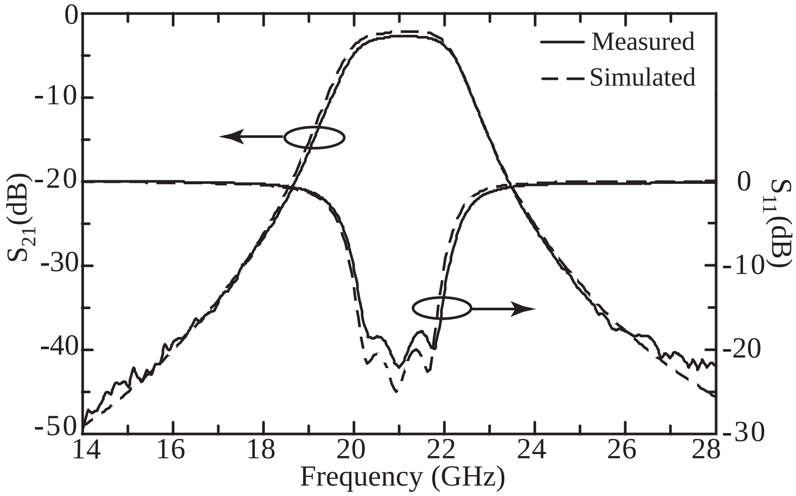

Figure 3.15: Measured and simulated S-parameters of the miniature 3-pole filter (Design # 1 in Table 3.8).

	#1	#2
No. of Bridges per Resonator	6	8
Total Length (μm)	3,622	3,254
Center Frequency (GHz)	21.1	21.2
1-dB Bandwidth (%)	8.6	7.8
Insertion Loss (dB)	2.9	3.5
Av. Bridge Height (μm)	1.1	1.1
Effective Loading Length l_2 (μm)	300	400
$\varepsilon_{r-eff(2)}$ in the Loading Region	55.0	55.0
Z_2 in the Loading Region (Ω)	15.9	15.9

Table 3.8: Measured parameters of the MEMS miniature filters.

as the pass-band center frequency, and fractional 1-dB bandwidth of the slow-wave miniature filter (Design #1 of Table 3.8) for 5 different values of the bridge height. At 1.1 μm, the slope of the variation of f_0 vs. g is 0.734 GHz/0.1 μm. The value of the bridge capacitor used at $g = 1.1$ μm is 76 fF ($w = 50$ μm, $W = 160$ μm), which is determined by fitting the model of Fig 3.13 to the measured results. This is very close to the full-wave simulated value of 74 fF, used in the filter design. The fractional bandwidth Δf is virtually insensitive to the height variations. While $S_C^{f_0}$ (sensitivity of f_0 to C) is nearly constant, $S_g^{f_0}$ (sensitivity of f_0 to g) is higher at low heights since $\delta C \sim -\delta g/g^2$. Therefore, a more robust design may be obtained by using higher MEMS bridges. However this will reduce the amount of loading and K in the slow-wave section, resulting in a lesser miniaturization.

Bridge Height g (μm)	0.9	1.0	1.1	1.2	1.3
Bridge Capacitance C (fF)	90	82	76	70	66
Center Frequency f_0 (GHz)	19.41	20.33	21.11	21.82	22.52
1-dB Bandwidth (%)	9.0	9.0	9.0	9.1	8.9

Table 3.9: Simulated pass-band parameters of the MEMS miniature filter for different bridge heights.

3.6.3 Miniature-Tunable K-Band Filter

The tunable filter is obtained by replacing the fixed bridge capacitors with MEMS varactors in the miniature filter presented in design #1 of Table 3.8. Fig. 3.16b shows 6 individual MEMS varactors ($w = 50$ μm) on the loaded section of the CPW line. The pull-down electrodes are 60 μm long and are located in the CPW gaps near the bridge anchors. To increase the capacitance ratio of the varactors, a step profile is used [69], which is higher at the pull down areas and lower in the middle section (Fig. 3.16c). To reduce the ohmic losses the bridge is electroplated with 2 μm gold except above the pull-down electrodes. This ensures a flexible membrane with a reasonable spring constant.

The tunable filter was fabricated on a glass substrate (quartz substrates were not available) with $\varepsilon_r = 4.6$ and $\tan\delta = 0.006$, and with the same layout shown in the previous section (Fig. 3.14). The measured parameters of the unloaded CPW line in this case are $Z_1 = 76\ \Omega$, $\varepsilon_{eff(1)} = 2.72$ and $\alpha_1 = 0.7$ dB/cm (transmission-line Q of 45 at 20 GHz). The MEMS bridges are fabricated at the height of 1.2 μm above the CPW center conductor (g_2) instead of 1.1 μm in the quartz-based design, which compensates for the higher dielectric constant. The pull-down electrodes are fabricated using a 1000 Å-thick SiCr layer with a resistivity of 1-2 kΩ/square. The electrodes on each side of the center conductor are tied to a different bias pad to eliminate any crossover with the CPW center conductor and therefore minimize the loading effects at microwave frequencies. This filter is tuned by applying a bias voltage of 0 to 90 volts. The bridges collapse at higher applied voltages.

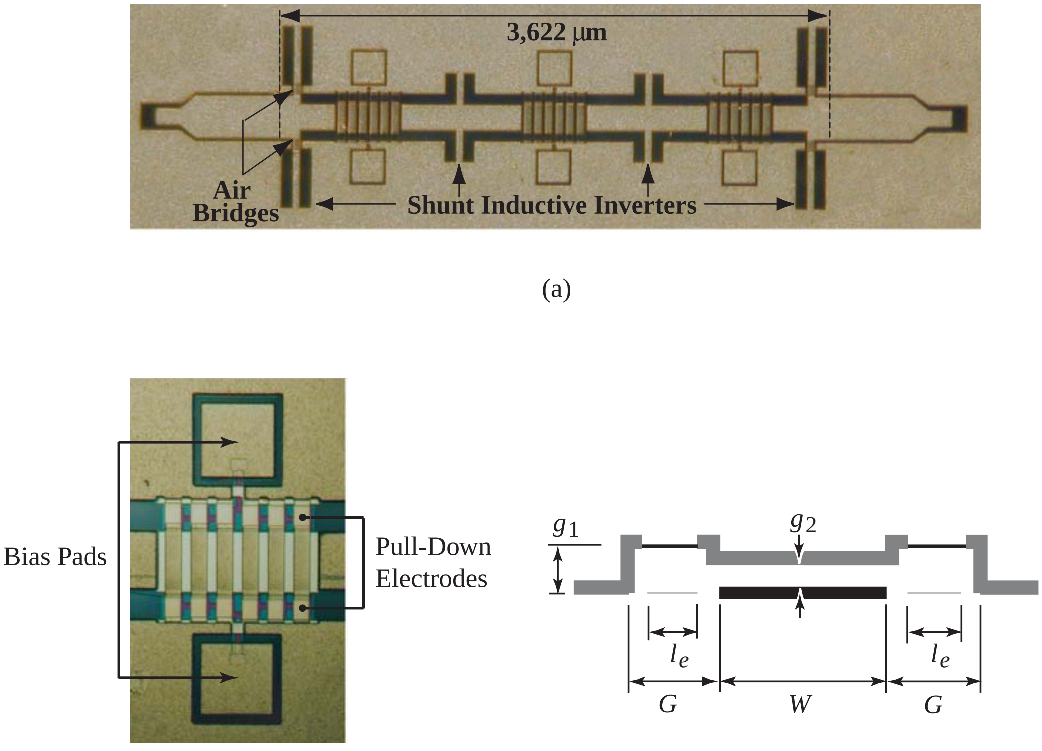

(a)

(b)

(c)

Figure 3.16: The fabricate miniature-tunable filter on a glass wafer: (a) photograph, (b) tunable slow-wave section, (c) MEMS bridge profile.

Figure 3.17 shows the measured response for a single tunable slow-wave MEMS resonator which is fabricated in this way (identical to the center resonator in Fig. 3.16a).

Table 3.10 provides the measured and fitted data for different values of the bias voltage. The loading factor and values of the MEMS capacitors have been extracted from the resonator model of Fig. 3.4b and (3.1) and (3.2). The MEMS varactors show a capacitance ratio of 2.84:1 in this case.

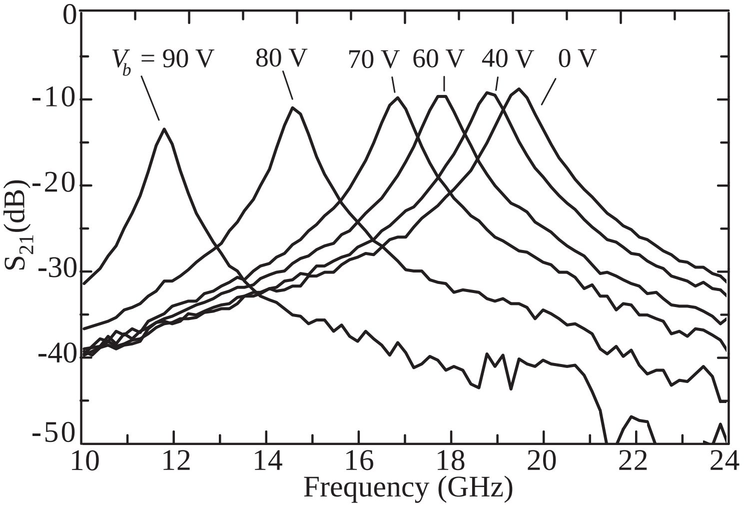

Figure 3.17: The measured $|S_{21}|$ of the tunable resonator for different values of the bias voltage.

Bias Voltage (V)	0	60	80	90
Resonance Frequency (GHz)	19.52	17.90	14.64	11.83
Normalized Length (to λ_g)	0.150	0.138	0.113	0.091
Bridge Capacitance (fF)*	88	106	160	250
Loading Factor K	25.3	30.3	45	70

* Extracted value using model.

Table 3.10: Measured parameters of The MEMS Slow-Wave Resonator for different bias voltages.

Fig. 3.18 presents the measured and simulated S-parameters of the miniature tunable filter for V_b =0 V and 80 V. Due to the fabrication mismatches, and also the relatively high level of the RF voltage at the second resonator of the filter, some bridges collapse for $V_b > 80$ V, and the filter shows a smaller tuning range than the comprising resonators. The exact value of the bridge height and capacitance vs. the bias voltage cannot be calculated using simple formulas due to the complex mechanical structure of the stepped-profiled bridge. The simulated S-parameters are based on the model in Fig. 3.13 with CPW line parameters and electrical lengths replaced by the new values, based on $K = 25.3$ ($C =$ 69 fF) and $K = 45$ ($C =$ 93 fF) for $V_b = 0$ and 80 Volts, respectively. The pass-band center frequency shifts from 21.44 GHz at 0 V to 18.60 GHz at 80 V, while the fractional bandwidth remains constant at $7.5 \pm 0.1\%$. The tuning range of this filter is $\pm 7\%$ centered at 20.0 GHz. The mid-band insertion loss varies from 3.85 dB in the upper band to 4.15 dB in the lower band. The higher value of loss as compared to the fixed miniature filter is believed to be due to the relatively high losses in the glass substrate. If the attenuation constant of the unloaded CPW line is changed from 0.70 dB/cm (measured on glass) to 0.37 dB/cm (measured on quartz), the simulated insertion loss in the upper band reduces to 2.8 dB, which is comparable to that of the quartz-based miniature filter. This indicates that the MEMS varactors maintain a Q of 350-450 similar to the fixed bridge capacitors.

An attractive feature of the miniature tunable filter is the constant fractional bandwidth in the tuning range. As was pointed earlier, this is due to the use of inductive inter-resonator couplings which compensate for the increasingly capacitive behavior of the resonators when they are tuned towards the lower frequencies [66]. While using inductive coupling along with tapped capacitive loading resulted in closer spurious pass-bands and lower rejection in the higher frequencies, in the case of the miniature tunable filter such negative effects are not observed. This may be attributed to the fact that in the short-ended slow-wave resonator, the loading has a minimal impact at the second resonance mode with a voltage null at the center. The first spurious pass-band in this special design appears at $> 3f_0$.

Fig. 3.19 shows a closeup plot of S_{21} for several values of the bias voltage. The

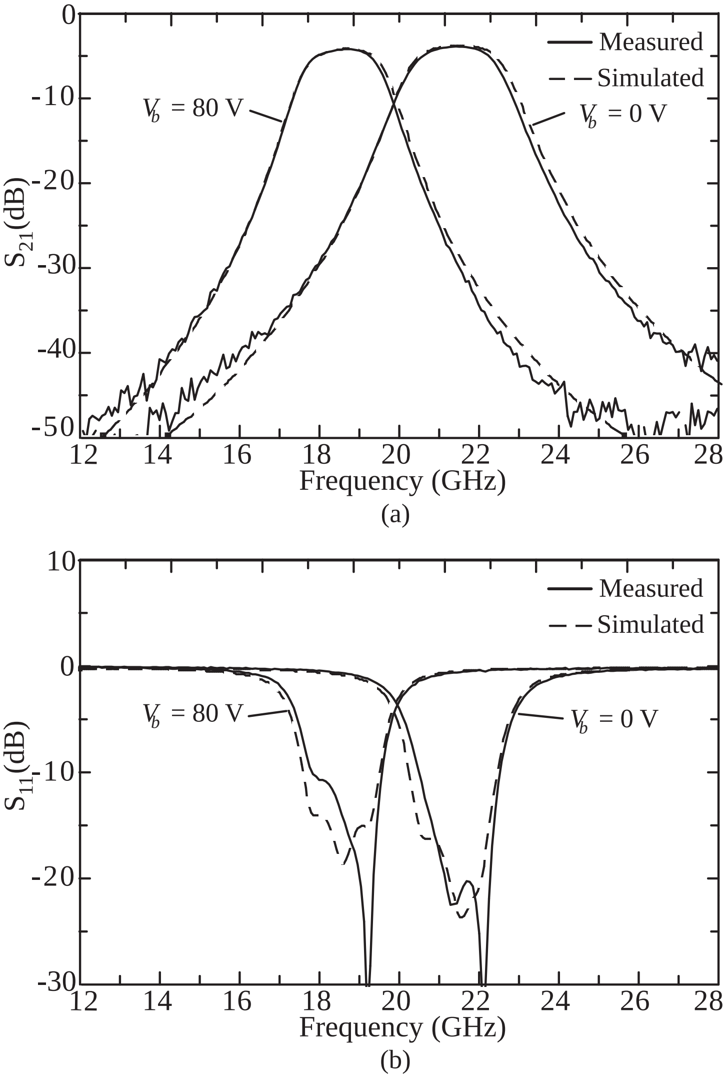

(a)

(b)

Figure 3.18: Measured and simulated S-parameters of the miniature tunable filter for $V_b = 0$ and 80 Volts; (a) S_{21}, (b) S_{11}.

corresponding data are summarized in Table. 3.11. The average estimated bridge resistance is R =0.15±0.05 Ω. R cannot be determined accurately, since its small impact on the mid-band insertion loss can be overwhelmed by the larger effect of the errors in the CPW line attenuation. A 10% error in the value α_1 used in the model, can change the estimated value of R up to 50%.

One concern about the miniature-tunable filter is the high value of the control

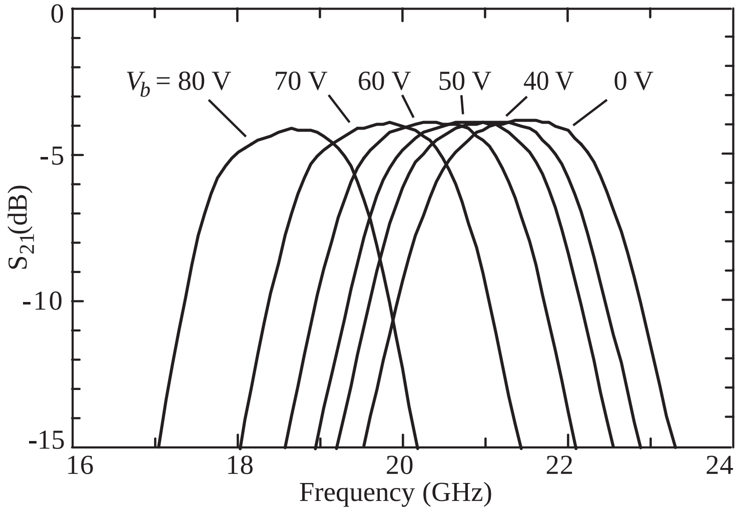

Figure 3.19: Measured pass-band response of the miniature tunable filter for different values of V_b.

Bias Voltage (V)	0	40	50	60	70	80
Center Frequency (GHz)	21.44	21.04	20.74	20.32	19.72	18.6
Bandwidth 1-dB (%)	7.37	7.60	7.52	7.67	7.35	7.58
Insertion Loss (dB)	3.85	3.90	3.90	3.92	3.94	4.15
Bridge Capacitance (fF)*	69	71	74	77	83	93
Bridge Height (μm)*	1.20	1.17	1.12	1.08	1.00	0.89

* Fitted values based on the measurement.

Table 3.11: Measured parameters of the miniature tunable filter for different values of bias voltage.

voltage. The reason for the high bias voltage in this case is the short length of the pull-down electrodes (l_e =60 μm) and the fact that they are located very close to the anchor points, resulting in a high effective spring constant. A solution to this problem is using the center conductor of the CPW line as the pull-down electrode. However, this requires adding large MIM capacitors in series with the coupling inductors or with the bridges in order to provide DC isolation between the center conductor and the bridges. The center actuated bridges typically have lower capacitive ratios, which limits the tuning range.

3.7 Nonlinear Characterization

Variations in the capacitance of the MEMS bridges under the high RF drive conditions result in a nonlinear behavior in the filters consisting MEMS capacitors. While the nonlinear effects are negligible for the MEMS miniature filter with thick electroplated bridges, they should be examined more carefully in the case of the MEMS tunable filters where flexible MEMS varactors are used.

A detailed study of the nonlinear behavior of the MEMS varactors and filters has been presented in [70]. This analysis shows that the nonlinear behavior of the MEMS varactor is directly related to the dynamic response of the bridge. For example, in the case of two-tone excitation, vibration of the bridge due to the force component at the beat frequency changes the capacitance, and presence of the input tones across this variable capacitor generates a third order intermodulation. The capacitance variations and consequently the IM_3 products are maximum for the beat frequencies near the mechanical resonant frequency of the bridge (f_m), and drop quickly at larger beat frequencies. What follows is based on the method developed in [70].

3.7.1 Capacitively-Coupled Tunable Filter [3]

The CAD-based model of a nonlinear MEMS capacitor is shown in Fig. 3.20. This model is composed of three blocks: A) electrostatic force generation, B) the mechanical bridge, and C) the variable-gap parallel plate capacitor. This model may be used to create a behavioral model in ADS [39] or similar CAD tools. Using this nonlinear element in the circuit model of Fig. 3.7, one can perform a nonlinear analysis of the capacitively-coupled tunable filter.

Although the outlined procedure forms a basis for the nonlinear simulation of

---

[3] This part has been indirectly reproduced from reference [70].

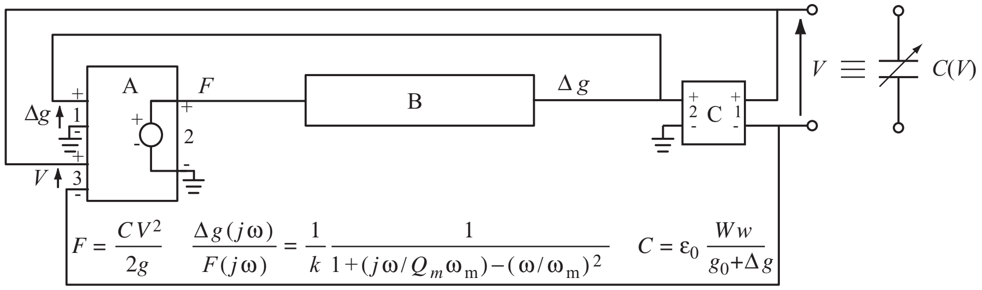

Figure 3.20: A CAD-based nonlinear model for the MEMS bridge capacitor.

the tunable filter, it requires the knowledge of the bridge mechanical parameters k, Q_m, and ω_m (see Fig. 3.20). As there is no straight forward way to determine these parameters, the preferred method is to perform some nonlinear measurements and then extract these parameters through fitting the simulation results to the measured data.

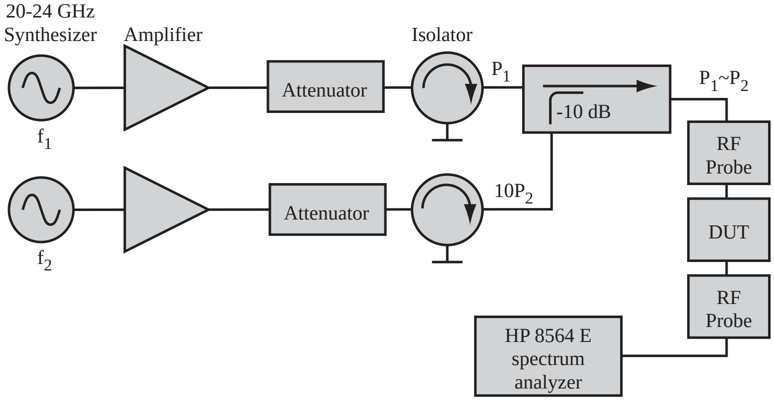

Figure 3.21: Experimental setup for intermodulation measurements.

This method has been used to characterize the tunable filter with capacitive coupling developed in Section 3.5.1. The setup used for measuring the intermodulation generation in the filter is shown in Fig. 3.21. The sinusoidal waveforms generated by two synthesizers are amplified and combined and then delivered to the MEMS filter. The output power at the fundamental frequencies as well as the third order intermodulation products are measured using a spectrum analyzer. Fig. 3.22a presents the measured intermodulation component (IM_3) vs. the difference frequency of the input tones (Δf). The simulated curve has been generated using the nonlinear model with the mechanical parameters $k = 55$ N/m, $Q_m = 1.7$, and $f_m = \omega_m/2\pi = 60$ kHz. The bridge dimension are $W = 160$ μm, $w = 130$ μm, and $g_0 = 1.4$ μm. The mechanical Q is relatively large, since holes have been made in the bridges to reduce the squeezing air effect (see Fig. 3.1).

Fig. 3.23b presents the power of the fundamental and intermodulation components vs. the input power for several values of the beat frequency. For $\Delta f = 60$ kHz, which is equal to f_m of the bridge, IIP_3 is 26.6 dBm. This value increases to 39 dBm for $\Delta f = 200$ kHz. The intermodulation decreases as $1/\Delta f^4$, and therefore the IIP_3 is $\cong 60$ dBm at $\Delta f = 2$ MHz [70].

3.7.2 Miniature-Tunable Filter

A similar analysis can be performed on the miniature-tunable filter with slow-wave MEMS resonators, developed in Section 3.6.3. However, since the different varactors in the slow-wave sections are subject to different values of RF voltage, the loaded-line-theory-based model in Fig. 3.13 cannot be used. Instead, nonlinear analysis of this filter has to be performed based on the full circuit model in which each slow-wave section is modelled by a combination of individual MEMS varactors (6 of them) and transmission-line sections. Each varactor is then replaced by a nonlinear model as shown in Fig. 3.20. The mechanical parameters of the MEMS bridge are extracted by matching the simulated IM curves using this nonlinear model to measurements.

The measured and simulated IM_3 curves resulting from a two-tone excitation are shown in Fig. 3.23a vs. the difference frequency Δf. The fitted mechanical bridge parameters in this case are $k = 190$ N/m, $Q_m = 1.9$ and $f_m = 52$ kHz for the bridge dimensions of $W = 160$ μm, $w = 50$ μm, and $g_0 = g_2 = 1.2$ μm. The high value

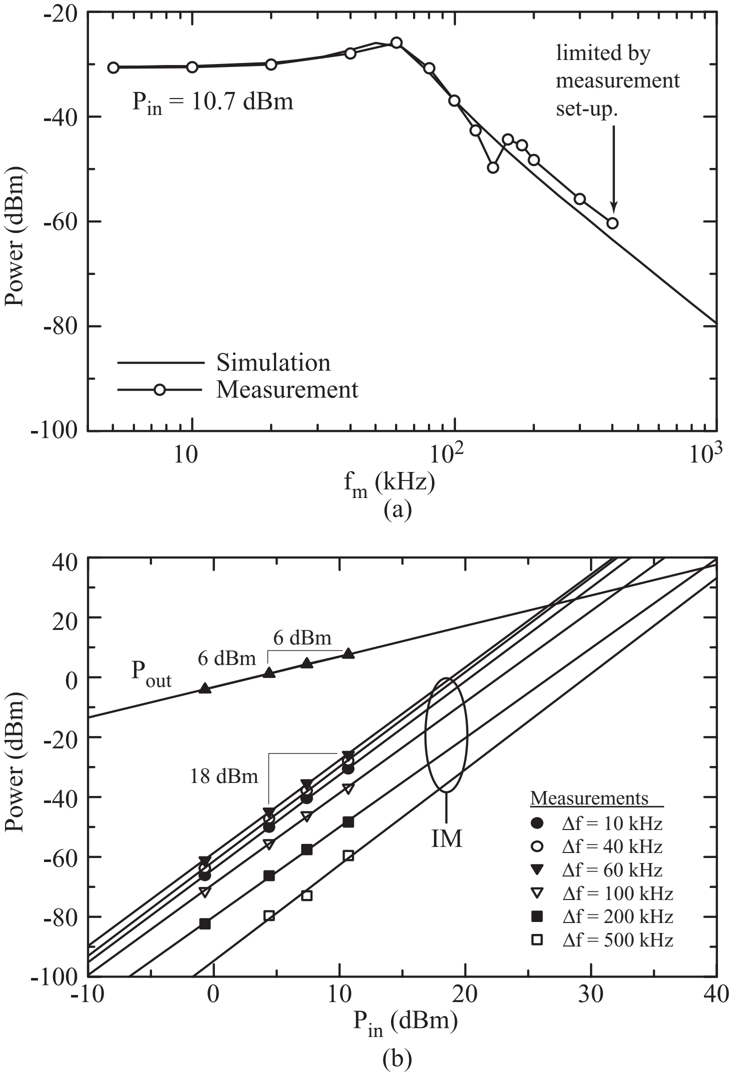

Figure 3.22: The third-order intermodulation product measured at $V_b = 0$ V for the capacitively-coupled tunable filter; a) the two-tone IM_3 vs. the beat frequency, b) the fundamental and intermodulation components vs. the input power.

of the spring constant is believed to be due to the very high residual stress which is estimated around 200 MPa. The output power P_{out} and the output IM_3 vs. the input power P_{in} are given in Fig. 3.23b. The IIP_3 is measured at $\sim$ 32 dBm for Δf = 50 kHz ($\cong f_m$) and increases to > 50 dBm for Δf > 150 kHz. The two-tone IM generation in the miniature filter is observed to be smaller than the tapped tunable filter. Both designs show a better linearity as compared to the tunable filters using diode varactors, with IIP_3's in the range of 12 dBm [55] to 28 dBm [56].

The nonlinear measurements presented here were carried out at $V_b = 0$ V. As demonstrated by Dussopt et al. [70], however, the third-order IM products vary as $1/g_0^8$, where g_0 represents the bridge height with no RF applied. Since g_0 decreases from 1.2 μm to 0.9 μm when the filter is tuned to 18.6 GHz (see Table 3.11), the IM_3 level is expected to be 10 dB higher in the lower band of operation which corresponds to a 5 dB reduction in IIP_3.

3.8 Conclusion

The possibility of using simple MEMS varactors to design tunable filters was addressed in this chapter. Two different schemes for integration of MEMS varactors in the CPW filter structures were considered and design methodologies were developed in each case. While a simple design based on capacitively coupled CPW resonators with tapped varactor loading is a straightforward method to achieve tuning, it results in filters with large size, small tuning range and very sensitive to tuning. Coupling slow-wave MEMS resonators using inductive inverters, on the other hand, proves a very effective means to obtain compact tunable filters with moderate tuning range, fixed fractional bandwidth, and robust frequency response.

The MEMS tunable filters are highly linear components in terms of generating mixing products of the input, and in worst case perform better than the semiconductor-based counterparts. Also they have a lower mid-band insertion loss, which is essentially limited by the losses in the CPW resonators. Further enhancement of the tuning range can be achieved by using better varactors with an extended capacitive range, or switched capacitors.

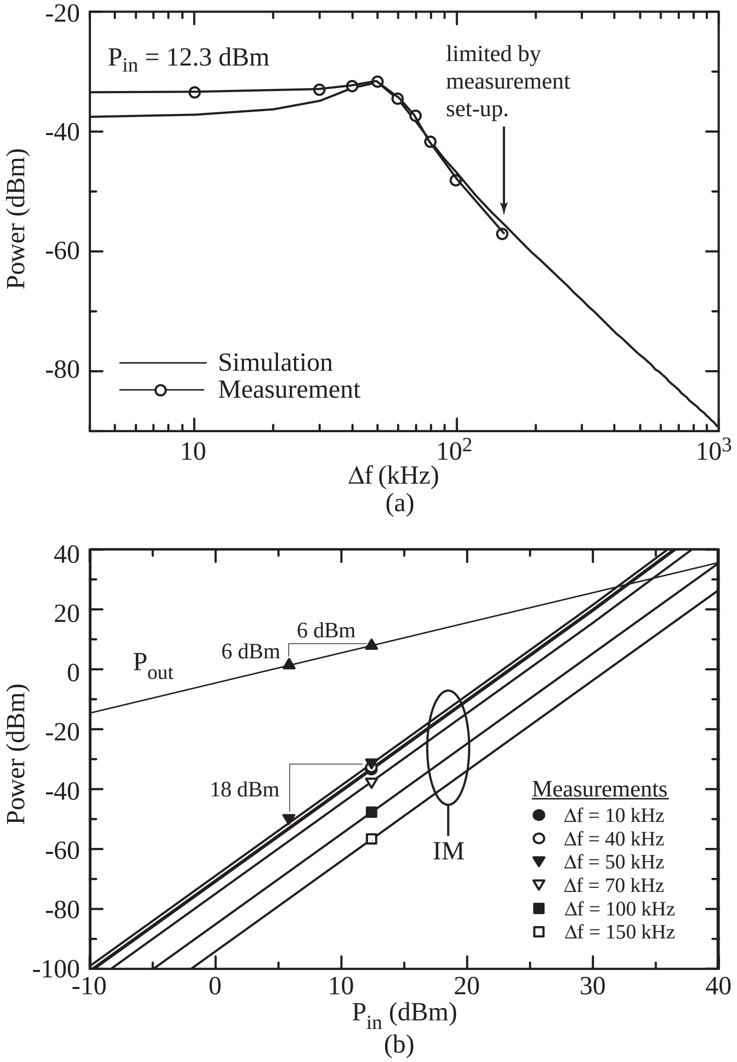

(a)

(b)

Figure 3.23: The third-order intermodulation product measured at V_b = 0 V for the miniature-tunable filter; a) the two-tone IM_3 vs. the beat frequency, b) the fundamental and intermodulation components vs. the input power.

CHAPTER 4

Antenna-Filter-Antenna Arrays As A Class of Bandpass Frequency-Selective-Surfaces

4.1 Introduction

Frequency selective surfaces (FSS) can be viewed as filters with radiative ports, which are generally realized using planar periodic structures. Depending on the geometry, a single-layer FSS can present a bandpass or bandstop response around its resonant frequency. High-order filters are commonly designed using multi-layers FSS structures [71][72]. Since the computational complexity drastically increases for multiple layers, design of the high-order frequency selective surfaces is performed by combining the individually designed FSS layers. The FSS layers, acting as individual resonators, are stacked using thick $(0.2 - 0.3\lambda_0)$ dielectric slab spacers which can be considered as simple impedance inverters, to form multi-pole filters. However, there are several problems with this method. First, the resulting filter topology as a chain of resonators and inverters is suitable only for a limited class of filter responses, which reduces the design space considerably. Second, the direct near-field coupling between the FSS layers in the stack and the loading effect of the dielectric slabs can invalidate the simple resonator-inverter interpretation. As a result, the filter synthesis methods offer only a rough first-pass design, and the design procedure generally has to be followed by re-tuning the individual FSS layers and dielectric slabs using elaborate optimization methods. Third, the overall stacked structure can be thick and bulky which is not desirable for many applications.

In this chapter, we introduce a new approach that uses an array of Antenna-Filter-Antenna (AFA) modules to form a high-order FSS. This method, which is described in more detail in the following sections, can be used to synthesize a large family of bandpass filters.

Developing an FSS design methodology, based on the described type of AFA modules is the main subject of this chapter. Specifically, we describe three illustrative design examples which demonstrate the variety of the response types that can be realized using this concept. Circuit based AFA design techniques, the relationship between AFA and FSS, finite element analysis, fabrication and measurement of the FSS samples are all addressed in detail.

4.2 Antenna-Filter-Antenna Concept

A schematic representation of an AFA array is shown in Fig. 4.1. Each AFA module is composed of a receive antenna, a non-radiating resonant structure, and a transmit antenna. Although the frequency characteristics of the antenna sets the limit on the transmission bandwidth of these modules, a more general category of the filtering shapes can be synthesized using this method. A simple example of such an FSS has been proposed in [71] (based on an earlier work [73]), where a pseudo-highpass filter is formed between the input and output apertures of an array of open ended waveguides.

Figure 4.2 shows a case where the radiative elements in the AFA are two back-to-back microstrip patch antennas, and the middle resonant structure is an ensemble of co-planar waveguide (CPW) resonators, which are fabricated in the common ground plane (referred to as the CPW layer). The coupling between the antennas and the

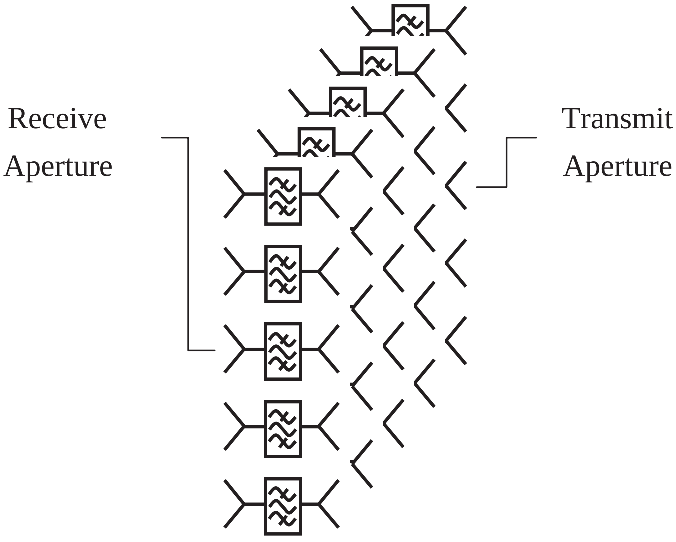

Figure 4.1: An array of antenna-filter-antenna modules as a bandpass FSS.

CPW resonators is achieved through coupling slots in the CPW layer. Use of the resonant-type radiative elements is advantageous, since a resonant element by itself can be considered as a combination of a radiative resistance and a resonator. The built-in resonators of the receive/transmit antennas can then be combined with the CPW resonant structure to form a bandpass filter between the radiative ends (Fig. 4.3). For a given filter order, this reduces the required number of CPW resonators. A special case of this structure is used in [74], where two patch antennas are coupled through a non-resonant slot to form a two-pole bandpass filter. As opposed to the conventional stacked FSS designs, a higher order response can be obtained simply by adding resonators in the CPW layer, instead of increasing the number of layers. Although some of the results might be rather general, the developments in the rest of this chapter are based on using AFA's with the described structure.

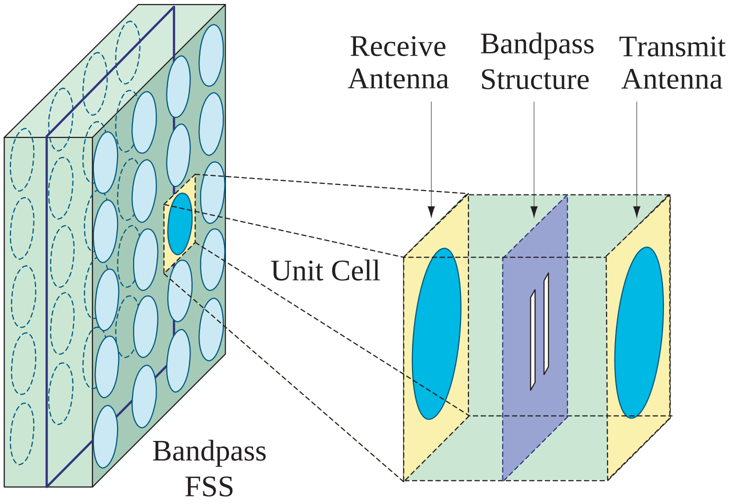

Figure 4.2: An AFA array composed of patch antennas and CPW resonators.

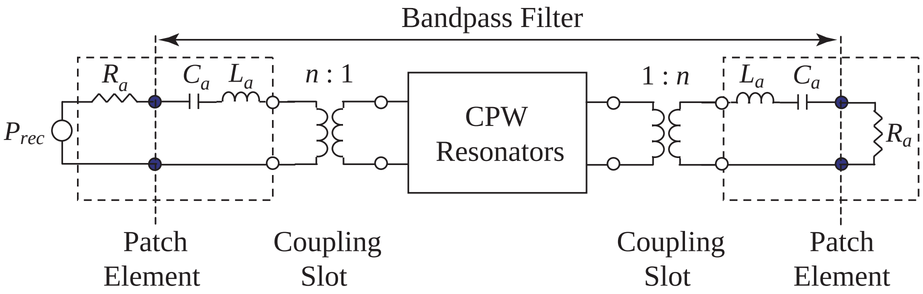

Figure 4.3: AFA as a bandpass filter between two radiative ports.

4.3 Design of AFA Modules

As soon as the circuit models of the antennas and the coupling slots, and their role in the filter topology is understood, designing the AFA modules is streamlined using microwave filter design techniques. Section 4.3.1 describes the general concerns in design of radiative elements and coupling slots. Design of the CPW structure depends on the specific filter topology, and will be demonstrated through three different AFA design examples in the subsequent section.

4.3.1 Basic Design Concerns

According to the circuit model shown in Fig. 4.3, the first and last resonators and the input/output coupling of the bandpass AFA are fixed upon the choice of the radiative element. The input/ouput coupling of the filter are related to the external Q (Q_{ext}) of the end resonators [60], which for a resonant patch element can be written as [37]:

$$Q_{ext} = Q_r = 2\pi f_0 \frac{W}{P_r} \tag{4.1}$$

where f_0 is the resonant frequency, W is the total stored electromagnetic energy, and P_r is the radiated power. Neglecting the losses in the antenna, Q_{ext} can be written in the following form:

$$Q_{ext} = 2\pi f_0 \frac{L_a}{R_a} \tag{4.2}$$

where L_a and R_a come from the series RLC model of the antenna (see Fig. 4.3). In the case of patch antennas, the substrate thickness is particularly important in achieving the desired value of Q_{ext}: the thicker the substrate, the lower Q_{ext} and the wider the pass-band. Also the geometry of the patch element can slightly affect the value of Q_{ext}. For a hexagonal patch element tuned at 35 GHz on a 500 μm-thick 7740 Corning Glass substrate ($\varepsilon_r = 4.45, \tan\delta = 0.006$), the estimated value of the external Q is 15.6, which is obtained by a lossless FEM simulation [75]. Based on the design equations in [60], this can be used to obtain a 3-pole Chebyshev filter with a fractional bandwidth of up to nearly 10% and a pass-band ripple of ≤ 0.45 dB (>10 dB return loss).

The amount of the coupling between the antennas and the CPW resonators is also very important and has to be carefully controlled. For the bandwidths of $< 10\%$, where the required values of the inter-resonator couplings are small, the coupling between the antenna and the CPW layer can be achieved by a short slot in the

CPW layer. Also, it is important to localize this coupling and prevent other parasitic interactions between the antennas and the CPW circuitry. In general, the CPW lines do not couple to the patch, since the magnetic currents in the CPW gaps are out of phase and cancel. Nevertheless, discontinuities, bends, or any geometrical deformations in the CPW lines that result in a net magnetic current, can generate a parasitic coupling mechanism and should be avoided.

To simplify the design task, the same type of patch element and layer structure is used for all designs that will be considered in this section. The CPW resonators have the cross sectional dimensions of $G/W/G = 50/100/50$ μm, with a thickness of 3 μm (Fig. 4.4). The simulated loss of the CPW line is $\alpha = 1.2$ dB/cm, which results in a resonator Q of 56 at 35 GHz.

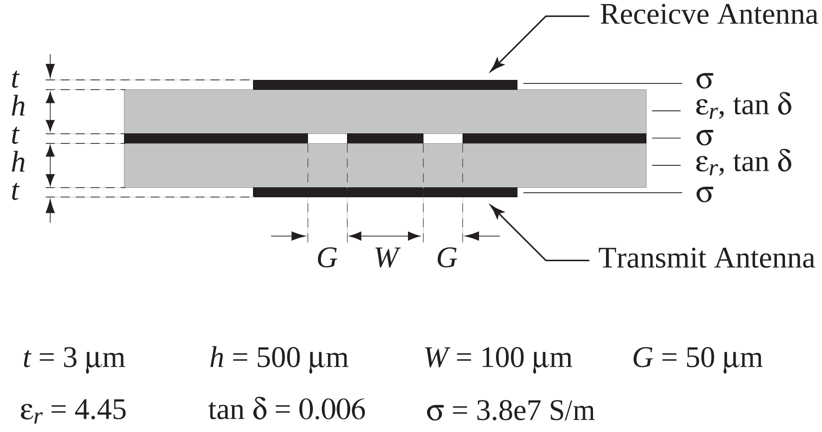

Figure 4.4: The layer structure used in the AFA designs.

4.3.2 Type-I AFA: 3-Pole Chebyshev Bandpass

The first design is a 3-pole Chebyshev bandpass design with 8% bandwidth at 35 GHz (Fig. 4.5a). This AFA, which we refer to as Type-I, is composed of two patch antennas and a quarter-wave CPW resonator. The CPW resonator is coupled to the fundamental resonance mode of the patches through its open end. The equivalent circuit consists of two series LC resonators, and a shunt stub that presents a parallel resonance at the center frequency (Fig. 4.5b). In practice, due to the finite inductance of the shorted end, the physical length of the shunt stub is slightly less than $\lambda_g/4$ (λ_g is the CPW guided wavelength).

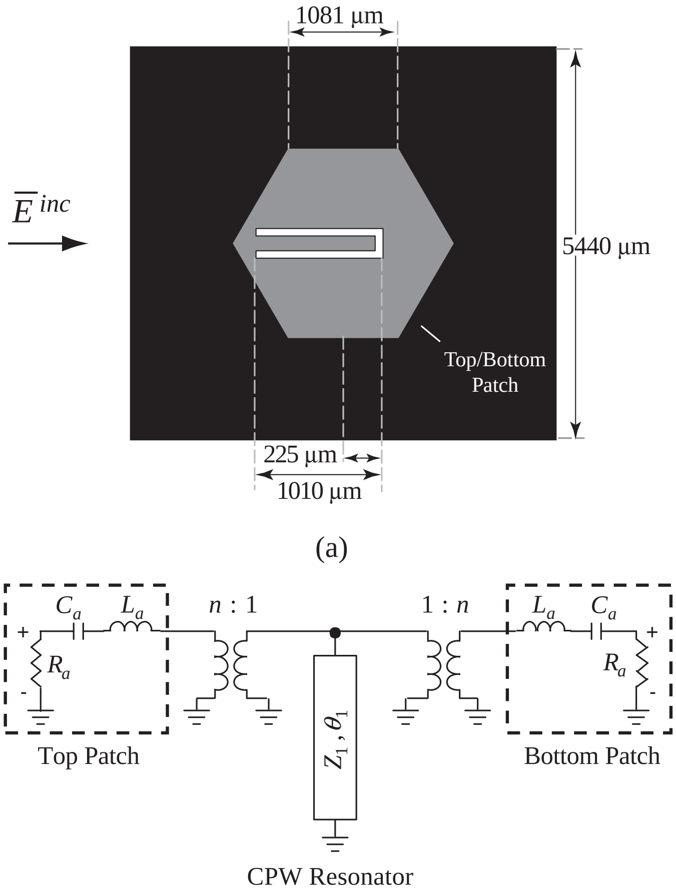

(a)

(b)

Figure 4.5: Type-I AFA: a) layout, b) circuit model.

The model parameters for the Type-I AFA are given in Table 4.1. The parameters in the antenna model can be extracted form the simulation of the antenna and the coupling slot in an infinite structure, or in a periodic array with a cell size of 5.44 mm which is determined from the effective radiative aperture of the antennas (see Sec. 4.4.1). The real design parameter after fixing the antenna and the CPW line dimensions, is the value of coupling between the antennas and the resonator (or equivalently n), and this is controlled by the position of the coupling slot with respect to the center of the patch. Fig. 4.6 presents the simulated S-parameters based on the circuit model. S_{21} and S_{11} represent the ratio of the transmitted and reflected power to the total power received by a single AFA cell (P_{rec}). The proposed circuit model and frequency response are only valid for a normal incident wave with the electric field polarized in parallel to the CPW resonator. This polarization will be here forth referred to as the principal polarization for this structure. The orthogonal polarization experiences different transmission and reflection coefficients.

R_a (Ω)	50	n	0.196
L_a (nH)	3.7	Z_1 (Ω)	65
C_a (fF)	5.6	θ_1 (deg.)	90

Table 4.1: Model parameters for the Type-I AFA at 35 GHz.

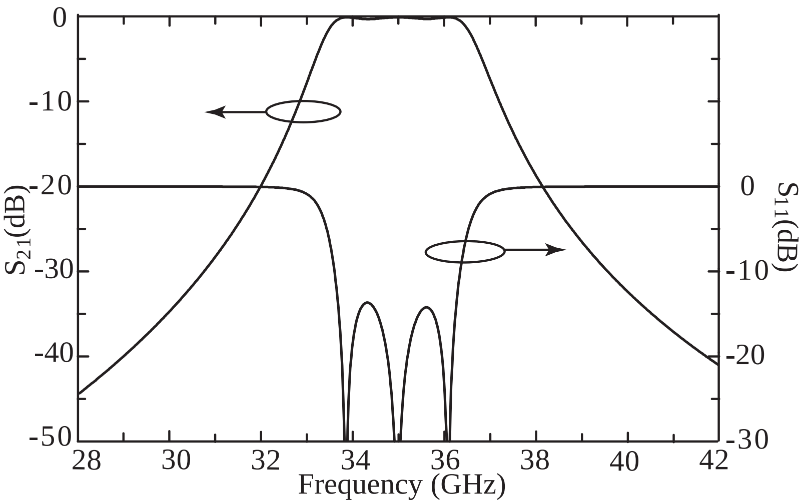

Figure 4.6: The simulated S-parameters of the Type-I AFA using the circuit model in Fig. 4.5b.

4.3.3 Type-II AFA: 3-Pole Bandpass with Transmission Zeroes

The geometry of the Type-II AFA cell is shown in Fig. 4.7 along with its equivalent circuit model. This filter has an equi-ripple response in the pass band and two attenuation zeros in the lower rejection band. A handful of topologies may be considered to realize transmission zeros, but what makes this design interesting is the presence of a 180° phase shift between its input and output at the center frequency.

The Type-II AFA is composed of two patches and a half-wave short-ended CPW resonator. The patches are coupled to the resonator through flared ends of the CPW gaps, which form two coupling slots. The phase translation is achieved by moving each patch towards one end of the resonator and coupling it to a different slot. In the fundamental resonant mode, the magnetic currents generated in these slots are out of phase, resulting in a 180° phase shift between the fields in the receive and transmit patches. Although the dominant coupling to each patch is through the slot which lies inside its resonance region (represented by the transformers with the turn ratio n_1), there is also a residual coupling through the opposite slot which interacts with the fringe field (represented by the transformers with the turn ratio n_2). Presence of this parallel signal path is, in fact, responsible for the existence of the transmission zeros in the lower rejection band. As the coupling in each patch takes place at two different locations, a transmission line (Z_0, θ_0) is introduced in the model to account for resulting phase difference, as shown in Fig. 4.7b. Since this secondary out of phase coupling tends to reduce the net amount of the coupling between the antennas and the CPW resonator, the coupling slots have to be designed significantly longer than in the Type-I AFA. The long slots present a considerable self-inductance, which is included in the model by adding inductors to the ends of the CPW resonator. Presence of these inductors modifies the resonant length of the half-wave resonator. The long slots also increase the length of the current path in the patch ground plane, and the patches need to be made smaller to compensate for the resulting change in the resonant frequency.

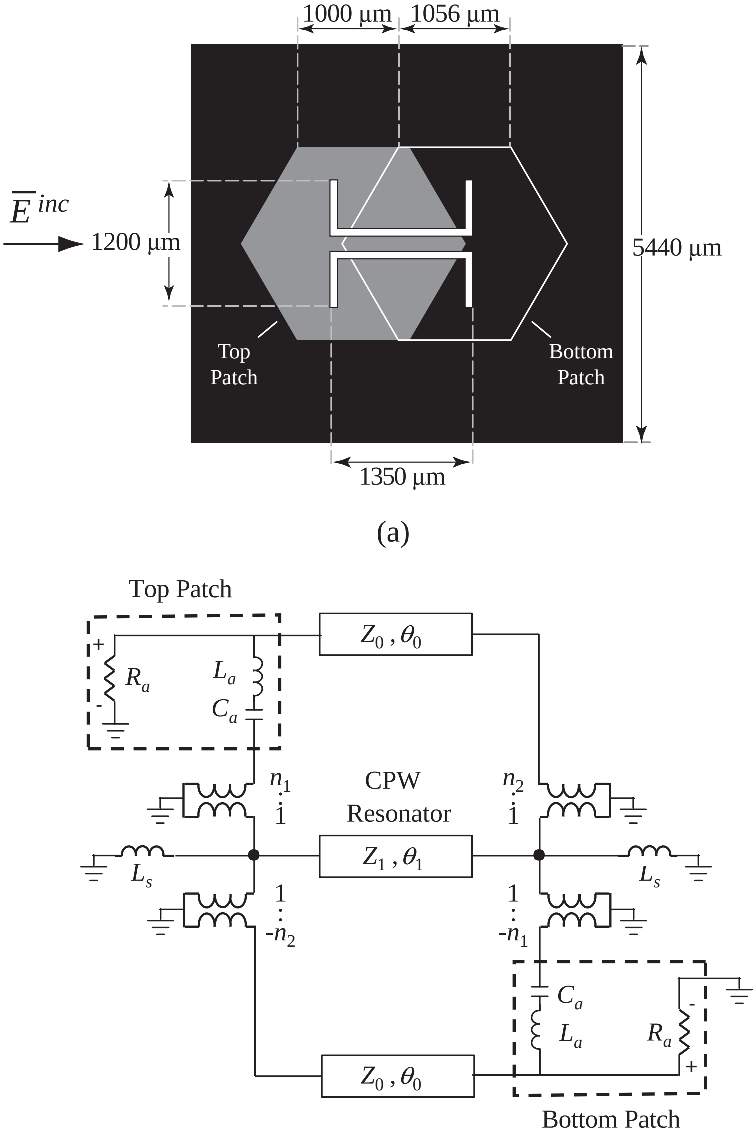

Figure 4.7: Type-II AFA: a) layout, b) circuit model.

The design process for the Type-II AFA includes finding the lengths of the coupling slots and the CPW resonator, and the relative location of the patch elements. As these parameters are generally linked in the physical layout, the design task requires more optimization through full wave simulation. However, the circuit model proves extremely helpful in understanding the effect of the geometrical parameters. The values of the model parameters for an 8% bandpass filter at 35 GHz are given in Table 4.2. Fig. 4.8 shows the simulated S-parameters for the Type-II AFA. Again, the simulated responses are valid only for the incident waves with principal polarization, which is defined similar to the previous example. The simulated S_{21} has two transmission zeros in the lower rejection band at 25.5 and 32.0 GHz.

R_a (Ω)	50	n_2	0.089
L_a (nH)	3.82	Z_0 (Ω)	50
C_a (fF)	5.6	θ_0 (deg.)	107.9
L_s (pH)	210	Z_1 (Ω)	65
n_1 (fF)	0.431	θ_1 (deg.)	107.9

Table 4.2: Model parameters for the Type-II AFA at 35 GHz.

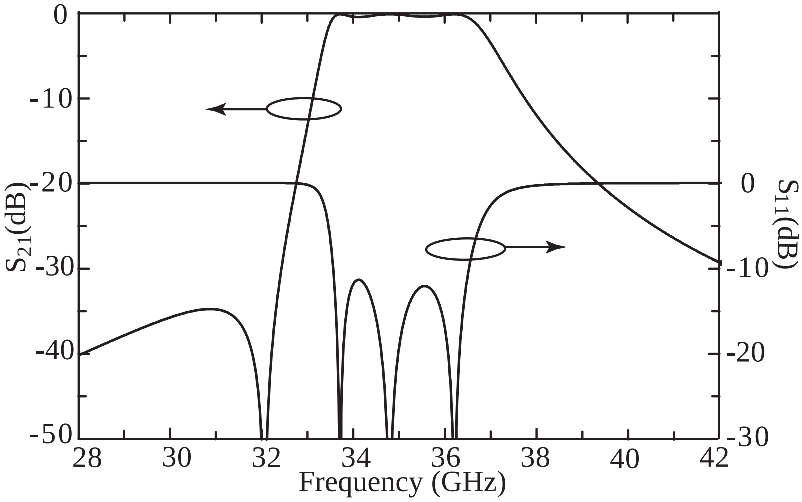

Figure 4.8: The simulated S-parameters of the Type-II AFA using the circuit model in Fig. 4.7b.

4.3.4 Type-III AFA: 4-Pole Chebyshev Bandpass

So far we have presented only 3-pole AFA designs. As the proposed AFA structures consist of three metal layer, one may tend to compare the AFA method with the standard multi-layer FSS approach. However, the advantage of using the AFA approach becomes evident when higher order filters are required.

A 4-pole AFA is obtained by using two quarter-wave resonators in the CPW layer (Fig. 4.9a). While each resonator in the Type-III AFA is coupled to only one of the antennas through its open end (similar to Type-I), the coupling between the resonators is achieved through shunt inductors at their common point. The inductors are realized using high-impedance lines between the center conductor and the coplanar ground [68]. These inductors result in no net magnetic current, and therefore they do not generate any unwanted coupling to the antennas.

The circuit model of the Type-III AFA is shown in Fig. 4.9b. The locations of the coupling gaps are determined for the required value of coupling (or equivalently n), similar to the Type-I design. The value of the coupling inductor, $L_{2,3}$, is simply determined from standard inverter design formulas [60]. The resonator length (θ_1) must then be modified to account for the self inductance of the coupling inductor [68][76].

The model parameters for an 8.5% Chebyshev bandpass filter at 35 GHz, and the simulated S-parameters are presented in Table 4.3 and Fig. 4.10. As expected, increasing the order of the filter can increase the bandwidth and enhance the out-of-band rejection of the filter.

One can easily think of ways to extend the structure of the Type-III AFA to obtain higher order filters. Any combination of CPW resonators that can be coupled to the quarter-wave resonators in Fig. 4.9b can readily increase the order of the filter. As long as these resonant structures lie outside the patch resonance regions, they do not form parasitic couplings to the antennas, and can be designed by a free use of the

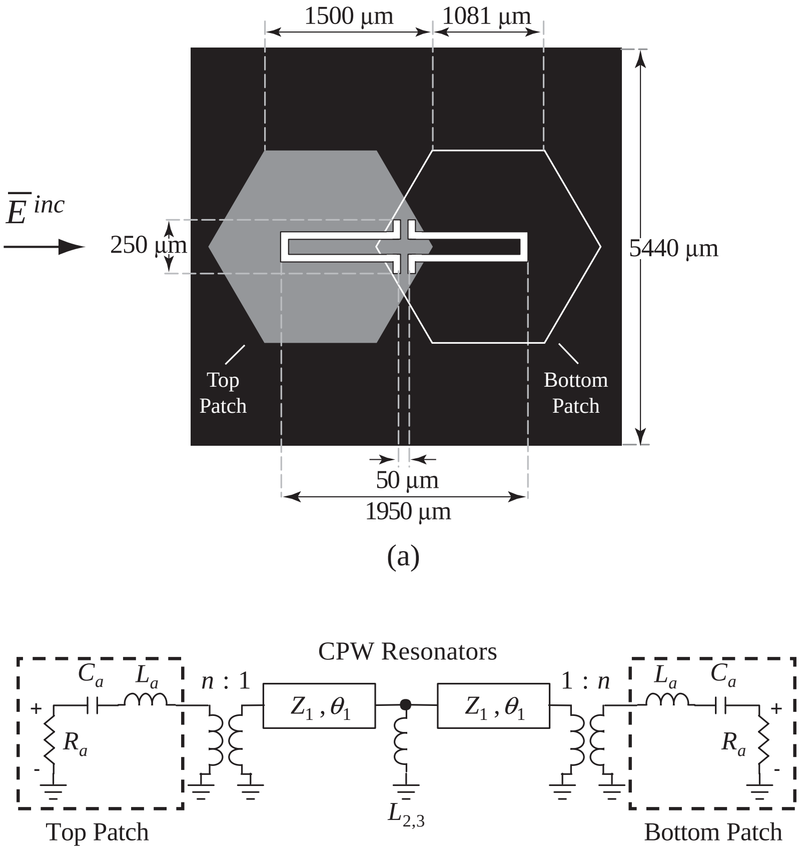

(a)

(b)

Figure 4.9: Type-III AFA: a) layout, b) circuit model.

filter design techniques. Nevertheless, an extensive use of CPW resonators can result in structures with unacceptable loss.

R_a (Ω)	50	n	0.196
L_a (nH)	3.7	Z_1 (Ω)	65
C_a (fF)	5.6	θ_1 (deg.)	87.7
$L_{2,3}$ (pH)	12		

Table 4.3: Model parameters for the Type-III AFA at 35 GHz.

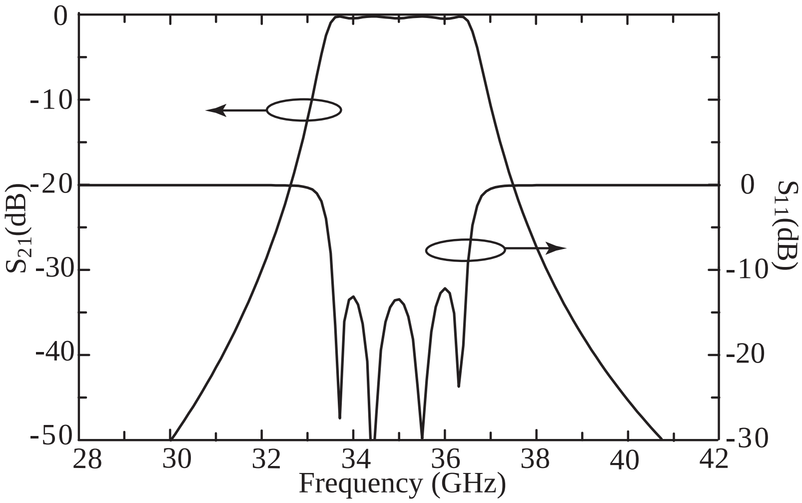

Figure 4.10: The simulated S-parameters of the Type-III AFA using the circuit model in Fig. 4.9b.

4.4 AFA-Based Frequency-Selective Surfaces

Once the AFA modules are designed, it is straightforward to form the FSS by arranging these modules in a periodic array. However, the frequency response of the FSS will not follow that of the AFA modules, unless a cautious choice of the cell size is applied. Also the grid size can affect the performance of the FSS through the surface-wave nulls.

4.4.1 Effect of The Cell Size on Frequency Response

As it was mentioned earlier, the filtering action of the AFA is performed only on the portion of the incident power which is received by the module (P_{rec}). This power is ultimately limited by the radiative aperture of the receive antenna, A_r, defined as [37]:

$$A_r(\vartheta,\varphi) = \frac{\lambda^2}{4\pi} D_e(\vartheta,\varphi) \tag{4.3}$$

where λ is the free space wavelength at the center frequency and $D_e(\vartheta, \varphi)$ represents the directivity of the antenna element in the direction of incidence (ϑ, φ)[1]. A single AFA element on an infinite ground plane can be viewed in the pass-band as a matched window ($Z_s = \eta_0 = 377\ \Omega$) of area A_r in the ground plane. In the rejection band, the AFA presents a purely reactive surface ($Z_s = jX_s$) to the incident wave, resulting in a total reflection of the incident power, and can be interpreted as a reactive panel of area A_r in the ground plane.

Using the above interpretation, an infinite AFA array can be considered as a metallic surface periodically covered with the impedance panels of area A_r, whose surface impedance $Z_s(\omega)$ is a function of frequency. If the cell area A_c is chosen equal to A_r, the patches form a uniform surface (Fig. 4.11a), and the entire incident power is delivered to the array of AFA elements. In this case, as long as the mutual coupling is negligible, $Z_s(\omega)$ is equal to the input impedance of the AFA modules, $Z_{in}(\omega)$, and the frequency response of the FSS is expected to be identical to that of the AFA's. On the other hand, if the cell size is different than A_r (Figs. 4.11b and c), the periodic array forms a nonuniform impedance surface. The frequency response in this case is no longer determined solely by the impedance of the patches, and is different than that of the comprising AFA's.

The above intuitive interpretation[2] suggests that there is only one value of A_c that results in a one-to-one correspondence between the frequency responses of the FSS and the constituent AFA's. Also this argument does not propose an optimal cell geometry (for example square or hexagonal). Nevertheless, it can be shown that in the absence of mutual coupling, the power received by each antenna element in a periodic rectangular array, is equal to that of a stand-alone element, if and only if $A_c = A_r$.

For the design examples in the previous section, the simulated directivity of the

---

[1] Although it is not obvious from (4.3), A_r is generally related to the physical dimensions of the antenna and does not have a strong dependence on frequency.

[2] Authors are not aware of a quantitative account of this subject in the open literature.

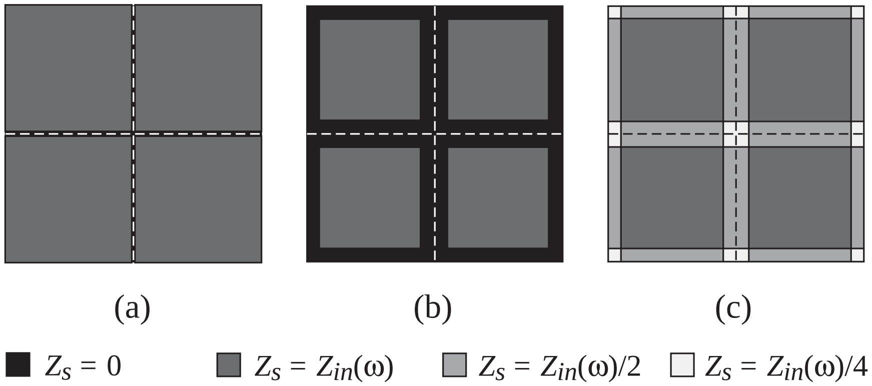

Figure 4.11: Representation of 4 unit cells in a periodic array of impedance panels: a) $A_r = A_c$, b) $A_r < A_c$, and c) $A_r > A_c$. Cell boundaries are shown in dashed lines. $A_c \equiv$ cell area; $A_r \equiv$ effective radiative aperture.

antenna elements at boresight is $D_e(0,0) = 7.04$ dBi at 35 GHz [39]. The effective radiative aperture is calculated using (4.3) as $A_r = 29.6$ mm^2 for the normal incidence in the principle polarization. Therefore an optimal square cell should have a side length of $l_c = 5.44$ mm.

4.4.2 Surface-Waves and Operation at Oblique Incidence

The fact that the FSS cell size has to be chosen equal to A_r can present a problem in applications where the FSS is considered for large incidence angles. For the microstrip patch antennas with a directivity of 6-8 dBi, the optimal A_c results in a cell side length of $l_c > 0.56\lambda_0$, for which the FSS forms an under-sampled array [77]. As a result, for some oblique angles of incidence, the periodic structure is prone to carrying surface wave modes at frequencies near to the pass-band [71]. These surface wave modes create strong transmission zeros, and their occurrence near the pass-band can result in a distorted frequency response. For an xy-aligned infinite array on a square grid of period l_c and the layer structure shown in Fig. 4.4, the TM Floquet modes excited due to incidence of a plane wave at angle (ϑ, φ) can be written as:

$$E_{z(m,n,p)} = \exp(-j[(\tfrac{2m\pi}{l_c} - k_0 \sin\vartheta \cos\varphi)x + (\tfrac{2n\pi}{l_c} - k_0 \sin\vartheta \sin\varphi)y]) \times \begin{cases} \frac{1}{\varepsilon_r} e^{-\alpha h} \cos\beta z & ,0 < z < h \quad \text{(dielectric)} \\ \cos\beta h e^{-\alpha z} & ,h < z < \infty \quad \text{(air)} \end{cases} \tag{4.4}$$

where α and β are the modal attenuation constant and wave number in the z direction (normal to the substrate), respectively. The values of α and β are calculated from:

$$\begin{gathered} \alpha h = \frac{\beta h}{\varepsilon_r} \tan(\beta h) \\ \varepsilon_r(\alpha h)^2 + (\beta h)^2 = (\varepsilon_r - 1)\left[(\frac{2m\pi h}{l_c} - k_0 h \sin\vartheta\cos\varphi)^2 + (\frac{2n\pi h}{l_c} - k_0 h \sin\vartheta \sin\varphi)^2\right]. \end{gathered} \tag{4.5}$$

The modal index (m, n, p) refers to the p'th solution of (4.5), for given m and n $(m, n = 0, \pm1, \pm2, ...)$. The resonant frequency of the $\mathrm{TM}_{m,n,p}$ surface wave mode is given by:

$$f_{m,n,p} = \frac{1}{2\pi}\left[\frac{\alpha^2 + \beta^2}{\mu_0\varepsilon_0(\varepsilon_r - 1)}\right]^{1/2} \tag{4.6}$$

With $l_c = 5.44$ mm, and for incidence at $(\vartheta, \varphi) = (0, 0)$, $(15°, 0)$ and $(30°, 0)$, the first surface wave null $(f_{1,0,1})$ is predicted at 49, 41.2, and 35.5 GHz, respectively. The surface wave nulls can be somewhat deterred by using lower-directivity elements with smaller A_r and closer packing of the AFA modules in the array. But the techniques for reducing directivity, such as using small antennas on high permittivity substrates may prove not useful, as increasing the dielectric constant tends to lower the frequency of the surface wave modes according to (4.5) and (4.6).

The underpopulated FSS is also prone to having grating lobes. But the grating lobes appear at higher frequency than the first surface wave null, and therefore do not pose an additional limitation.

4.5 Finite Element Simulation

When the cell size is determined, a finite element simulation of the structure can be performed based on the periodic boundary conditions. If the polarization of the incident electric field is in parallel with one of the FSS grid axes and for the normal incidence, the periodic boundary conditions may be replaced by the PEC and PMC walls to reduce the computational complexity. The layer structure presented in Fig. 4.4 is used, and the thickness of the metal layer and the losses in the dielectric substrate and conductors are neglected at this stage. The layout of the CPW layer is designed based on circuit model parameters and moment-method simulations [39]. The FSS structure is simulated using the commercial FEM simulator, HFSS [75]. The final tuning of the frequency response, if necessary, is performed by tweaking some critical dimensions.

Fig. 4.12a shows the FEM simulation of the reflection and transmission coefficients for an FSS obtained by arraying Type-I AFA elements and $l_c = 5.44$ mm. The circuit-based S-parameters of the AFA are also presented, which clearly match the FEM results. The FEM simulations for FSS's with the same type of element and ±20% variation in l_c are shown in Fig. 4.12b. It is evident that only for the optimal value of $l_c = \sqrt{A_r}$, the FSS achieves the desired frequency response. According to the FEM simulations, for $l_c = 5.44$ mm, the surface wave null is located at 48 GHz (within 2% of the value calculated in previous section). For $l_c = 6.62$ mm, this null moves to 41 GHz, as can be seen in Fig. 4.12b.

Similarly, FSS's can be formed based on the Type-II and Type-III AFA's and using the optimal cell size (Fig 4.13). The FEM simulation closely follows the AFA-based analysis for the Type-II FSS, but shows a noticeable discrepancy in the case of the Type-III FSS. In the latter case, the simulated transmission coefficient contains two out-of-band transmission zeros, which are not predicted using the AFA model. A closer inspection of the AFA geometry in Fig. 4.9, however, suggests formation

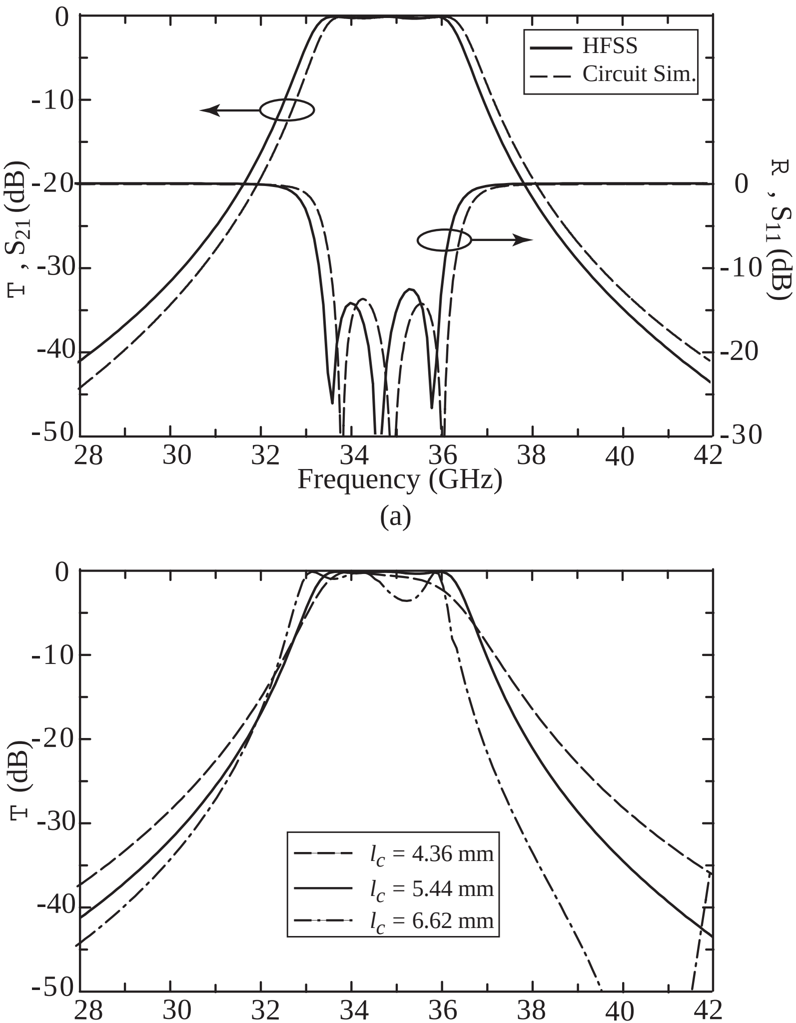

(a)

(b)

Figure 4.12: FEM simulation of the Type-I FSS: a) FEM (sloid) versus AFA circuit simulation (dashed), b) FEM simulations for different values of l_c.

of a direct coupling of the input/ouput signals (waves) to the quarter-wave CPW resonators, which are prone to radiation at their open ends. This direct coupling, which is not included in the AFA model of Fig. 4.9b, creates a parallel signal path which is responsible for the presence of the transmission zeros.

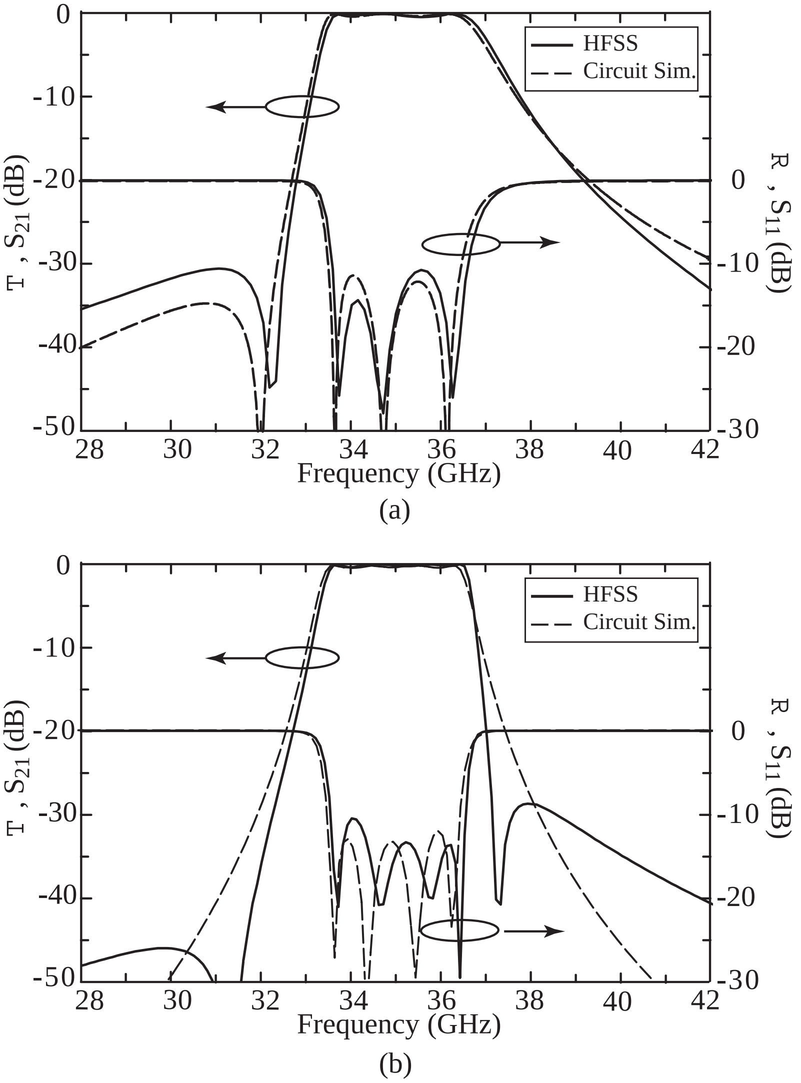

(a)

(b)

Figure 4.13: FEM simulations of reflection and transmission coefficients a) Type-II FSS, b) Type-III FSS. Dashed lines show the AFA circuit simulation.

4.6 Fabrication

Choice of the fabrication process for the AFA-based FSS's is particularly important at millimeter-wave frequencies, for at least two reasons: 1) geometrical tolerances, and 2) stacking imperfections.

Due to the small dimensions of the features at the Ka-band, the proper operation of the FSS requires an accurate control of the fabrication process. The sensitivity is maximized for the CPW layer, where tolerances of less than ±2 μm are necessary. Therefore, it is not possible to prototype the AFA-based FSS structures using simple PCB (printed circuit board) and copper etching techniques, and a more advanced fabrication process based on the thin film technology should be used. Furthermore, as most adhesives are lossy at millimeter-wave frequencies and also cannot be applied with an accurately controlled thickness, stacking the substrate layers as shown in Fig. 4.4, poses another challenge.

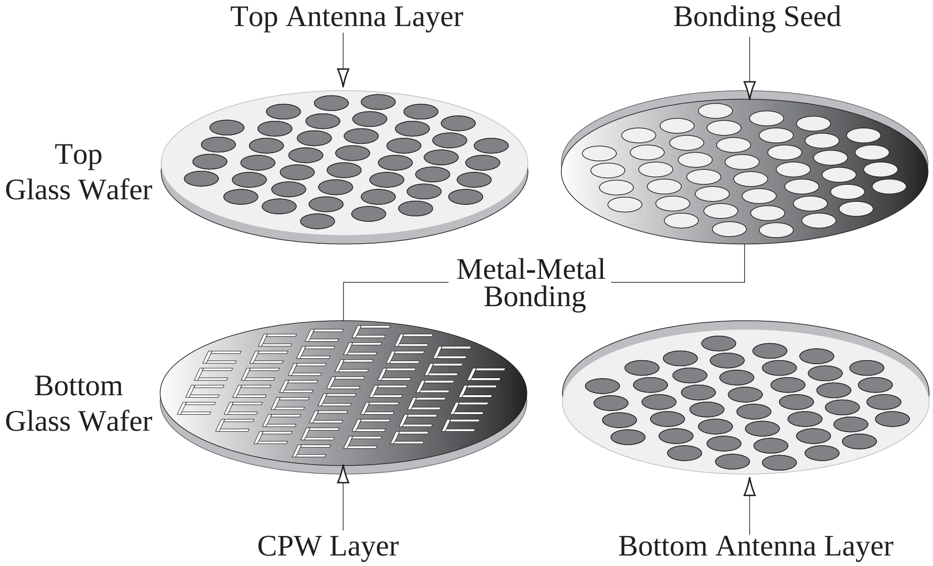

Figure 4.14: The detailed description of the physical layers in a laboratory fabricated prototype.

Fig. 4.14 outlines the process for the fabrication of a laboratory prototype. The sample is fabricated using two 500 μm-thick 7440 Corning Glass wafers. First one side of each wafer is covered with a 500 Å evaporated Ti layer. Photoresist is then spun on this seed layer and patterned using lithographic techniques. The patch antennas are deposited using an evaporated film of 300 Å Ti/5000 Å Au, and a lift-off process. These patches are then electroplated with Au to a thickness of 3-5 μm, and the Ti seed layer that has served to the electrical connectivity of the patches during the electroplating is now removed, leaving an array of thick gold isolated patches. This completes the fabrication of the top and bottom antenna layers as shown in Fig. 4.14. In the next step, the photo resist is spun and patterned on the second side of the two wafers. The CPW layer and the bonding seed layer, are then deposited using another evaporated 500 Å Ti/5000 Å Au layer. The bonding seed is a metallic grid that entirely overlap with the CPW ground plane in the final stack. This layer has no electromagnetic function, and is merely used to facilitate metal-to-metal bonding of the wafers. The CPW layer is then electroplated to 3 μm, which is approximately 5 times the skin depth at 35 GHz ($\sigma = 3.8 \times 10^8$ S/m). The bonding seed layer is left intact.

The final fabrication step is to bond the two processed wafers. As mentioned earlier, using adhesives between the two wafers can cause a multitude of problems, from adding losses to thickness variations to changing the effective dielectric constant of the CPW layer. Overall, using such materials is not recommended. The process of choice in this case is a thermo-compression bonding [78]. In this process the top and bottom wafers are aligned and the bonding is formed between the gold in the CPW and bonding seed layers, by applying a pressure of 40-50 N/cm^2 at the temperature of 390°C. This temperature can be readily endured by the Pyrex glass wafers (strain point = 510°C, softening point = 821°C).

4.7 Measurement Method

An accurate measurement technique is vital to the assessment of the design method. In particular, the ability to accurately measure both transmission and reflection coefficients can provide an enormous help in identifying the design errors and fabrication imperfections.

Usually, the frequency selective surfaces are measured either by shining a large sample with a plane wave in the anechoic chamber, or by replacing a small sample in a waveguide and measuring the S-parameters. The first method obviously requires a large sample, and normally does not provide a way to measure the reflection. The waveguide technique can measure reflection, but it has two disadvantages. The cross-sectional dimensions of a standard waveguide are not generally integer multiples of the FSS grid period l_c. Also, as the full metallic waveguide cannot carry an TEM mode, it cannot be used to measure the sample at normal or arbitrary angles of incidence.

An alternative approach is to use a free space measurement setup that simulates the guided system. Quasi-optical measurement systems have been used for this purpose by a number of researchers [79], [80], for performing similar measurements at 60-300 GHz. But the required lens/mirror size and focal length prove impractical at Ka-band. Based on the hard-horns developed by Ali et. al. [81], a guided measurement system can be developed to simulate an oversized parallel-plate waveguide. Hard-horns are antennas with nearly uniform aperture distribution, which are formed by dielectric loading of the metallic pyramidal horns. A specially designed dielectric lens is used at the aperture to compensate the spherical phase error across the aperture. The hard-horns act as a matched transition between the coaxial terminals and the oversized TEM waveguide ports. The sample under test can be sandwiched between two of these waveguide ports, to form a guided system with coaxial ports. This system has been successfully used for excitation and measurement of Ka-band quasi-optical amplifier arrays [82]. Although in our application it is impractical to sandwich the FSS sample between the two hard-horns, due to the loading effect of the dielectric lenses, still the hard-horns can be used to form a quasi-guided system. In the modified system, which is shown in Fig 4.15, the hard horns form two parallel TEM ports that are separated by an air gap, and the sample under test is replaced in the middle of the two ports. Due to their high directivity, the hard-horns are expected to generate a good approximation of the plane wave in the near-field, as is required for the FSS measurements. As the sample can be freely reoriented in the air gap, the quasi-guided system proves convenient for performing measurements at arbitrary angles of incidence. However, the oblique incidence measurements generally require larger samples and a wider air gap.

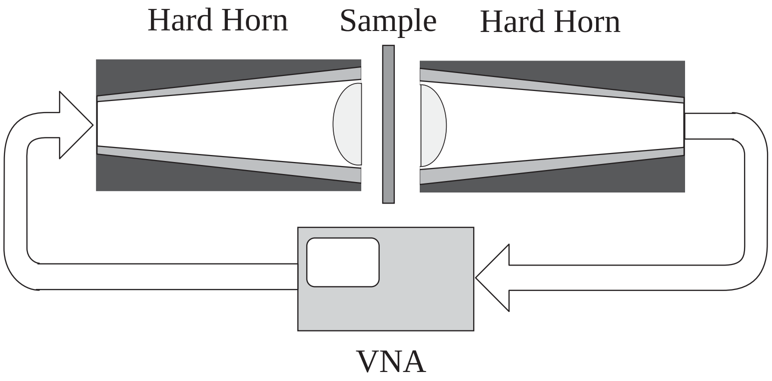

Figure 4.15: The free-space measurement system using hard horns.

Since the electromagnetic field in the gap region is assumed to be predominantly TEM, the air gaps between the hard horn apertures and the surface of the sample can be treated as transmission-line sections. This allows for a standard TRL (Thru-Reflect-Line) calibration of the measurement setup, which simultaneously de-embeds the connecting cables, hard horns, and the air gaps from the measurement [83]. Also a time-gating process is applied, to filter out the residual error due to the multiple reflections of the high-order modes.

4.8 Experimental Results

Samples of the Type-I and Type-II FSS's were fabricated and tested at the University of Michigan. Although the initial samples had the general form of the desired frequency response, the measured results were considerably different from the simulations (not shown). A close examination of the fabricated arrays revealed the sources of this discrepancy. In the simulations, the CPW layer are considered to be immersed in a homogeneous dielectric medium of $\varepsilon_r = 4.45$. However, as it can be seen from the layer structure in Fig. 4.4, due to the finite thickness of the gold CPW lines ($t \approx 3$ μm), a portion of the CPW gaps is filled with air. Also, the bonding seed layer is 0.5-0.6 μm thick, and creates an air gap between the top wafer and the CPW metal layer (see Fig. 4.14). Although very thin, presence of these air regions at the location of the highest electric field density results in a measurable reduction in the effective dielectric constant of the CPW lines. Fitting the circuit model simulations and the measured data for the first set of samples of the Type-I and Type-II FSS resulted in $\varepsilon_{r-eff} = 4.15$. Based on this observation, the lengths of the CPW resonators were adjusted and new FSS samples were fabricated. The layout dimensions in Figs. 4.5a and 4.7a indicate these modified values.

The measured and simulated reflection and transmission coefficients of the Type-I FSS for normal incidence in the principal polarization are presented in Fig. 4.16. The measured data are given for the 30-40 GHz band, which is the range of operation of the measurement setup. A pass-band response with 1-dB band-width of 8.2% centered at 35.1 GHz, and a mid-band insertion-loss of 3.0 dB are measured. Circuit simulations can be repeated based on the model in Fig. 4.5b, with the values of Z_1 and θ_1 modified for $\varepsilon_{r-eff} = 4.15$. After adding a series resistor of $r_a = 7.0\ \Omega$ to the antenna model and an attenuation coefficient of $\alpha_1 = 1.7$ dB/cm to the CPW transmission-line, the circuit simulations show a perfect match with the measurement. This is equivalent to an antenna efficiency of 88%, and a resonator Q of 38 for the CPW resonator. Figure 4.16 also presents the FEM simulations after introducing a finite conductivity of $\sigma = 3.8 \times 10^7$ S/m (for the electroplated gold) and a dielectric loss tangent of $\tan\delta = 0.006$. From the total of 3.0 dB insertion loss at the mid-band frequency, 1.3 dB is due to the losses in the dielectric substrate, and the rest is due to the ohmic losses in the metallic structure which is mainly contributed from the CPW resonator.

Fig. 4.17 shows the measured and simulated frequency response for the Type-II FSS, for normal incidence in the principal polarization. The pass-band is 8.2% wide and is centered at 36.0 GHz. Although the layout of this design was also modified for $\varepsilon_{r-eff} = 4.15$, later matching of the circuit simulations to the measured data resulted

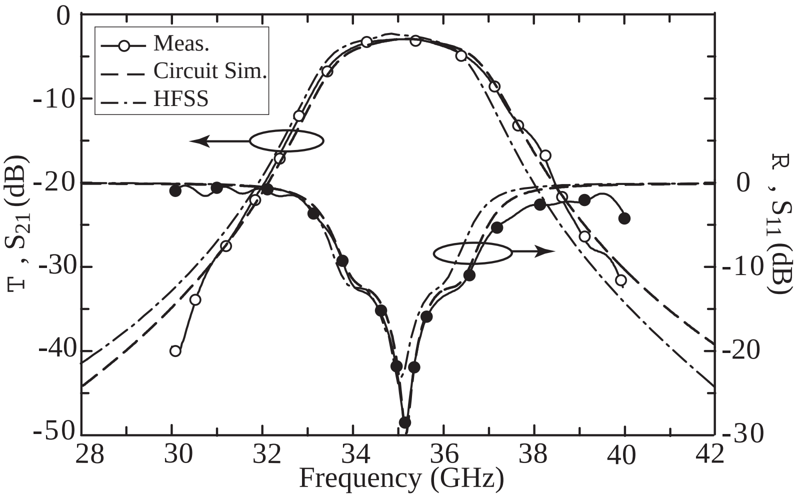

Figure 4.16: The measured and simulated frequency response of the Type-I FSS for normal incidence with the principal polarization.

in a dielectric constant of $\varepsilon_{r-eff} = 4.00$ for the CPW line, which explains the 3% de-tuning of the pass-band. This could be caused by higher thicknesses of the gold in the CPW layer, or the air gap between the top wafer and CPW metallization. The presented circuit simulations are based on the model in Fig. 4.7b with values of Z_1 and θ_1 adjusted for $\varepsilon_{r-eff} = 4.00$, and losses added in the antennas, CPW resonator, and the series inductors ($r_a = 7.0\ \Omega$, $\alpha_1 = 1.7$ dB/cm, $r_s = 2.2\ \Omega$). The measured mid-band insertion loss is 3.5 dB, in this case, from which 1.2 dB is result of the dielectric losses and the rest is due to the conductor loss in the CPW structure and antennas. There is no clear explanation why the FEM simulated insertion loss does not match the measurement, but it can be due to the same type of fabrication imperfections that cause the detuning in the pass-band.

The Type-III FSS was not fabricated for this work. But using the loss parameters obtained from matching of the two previous design to the circuit model, a modified circuit simulation can be performed. Such a simulation predict a mid-band insertion loss of 5.4 dB for an actual FSS sample of this type.

As mentioned earlier, the performance of the AFA-based FSS's at the oblique

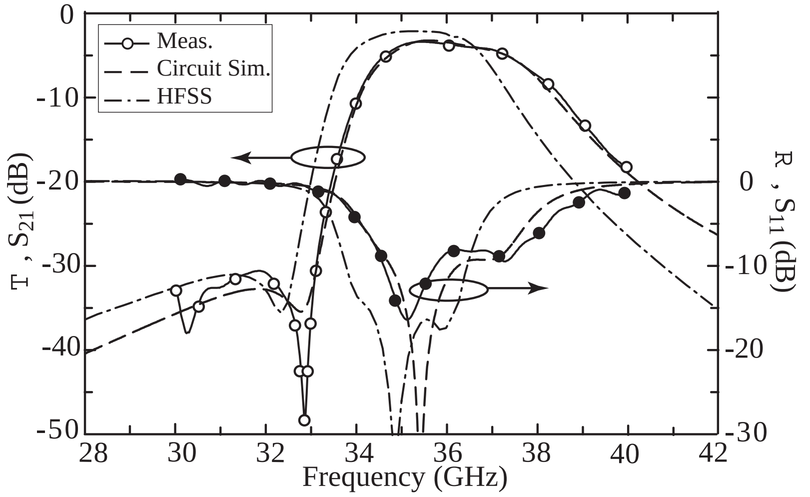

Figure 4.17: The measured and simulated frequency response of the Type-II FSS for normal incidence with the principal polarization.

angles of incidence is limited by the presence of the first surface-wave null. To further examine the angular range of operation, the measurement of the Type-I FSS was repeated for the incidence angles of $(\vartheta, \varphi) = (15^\circ, 0)$ and $(25^\circ, 0)$. The resulting transmission coefficients are presented in Fig. 4.18 along with the measured response for the normal incidence. As expected, the transmission coefficient quickly deteriorates with increasing the angle of incidence. At $\vartheta = 25^\circ$, the transmission null is located at 36.5 GHz, which is practically inside the pass-band.

4.9 Conclusion

Using periodic arrays of the antenna-filter-antenna (AFA) modules is proposed as a new method to design high-performance band-pass FSS's with a shaped frequency response. The flexibility of this method stems from the fact that the AFA modules can be designed as individual elements based on filter synthesis techniques. This results in an accurate design method which requires a minimal number of full-wave simulations. The AFA method can be used to form frequency responses that are much

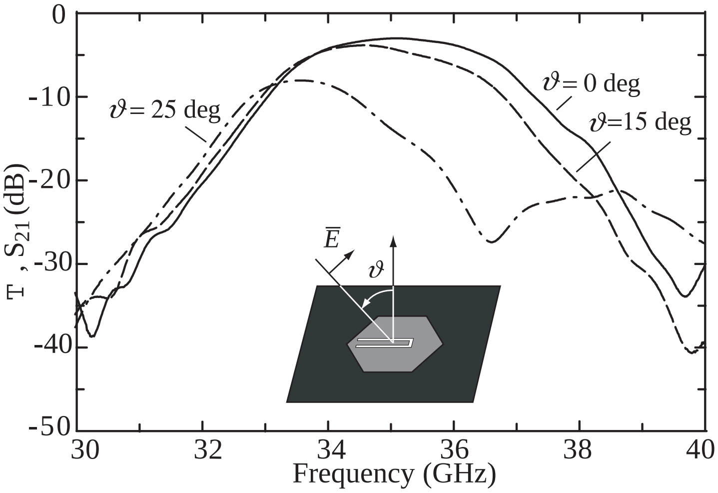

Figure 4.18: Measured transmission coefficient of the Type-I FSS for 3 different values of the angle of incidence.

more general than what is achievable using stacked FSS designs. Also, the AFA-based FSS's have a simple layer structure and a much smaller overall thickness. However, as the cell size cannot be made arbitrarily small, the FSS structure can easily support surface wave resonant modes that are close to the pass band at oblique angles of incidence, which results in a narrow angular range of operation ($\vartheta \leq \pm 20°$). Also, as the AFA modules are generally polarization sensitive, designing a dual-polarized FSS based on this technique seems rather difficult. In spite of these limitations, the AFA arrays may be considered for applications where the incoming signal is collimated and linearly polarized. They are expected to find application in designing radomes for high gain antennas, multi-feed shared-aperture antennas, high-impedance reactive surfaces, and bandpass filters for waveguides or band-limited quasi-optical amplifiers.

CHAPTER 5

Filter-Lens Arrays

5.1 Introduction

Lens antennas are extensively used in millimeter-wave radars, for applications in beam-forming, scanning, imaging, and quasi-optical power combining. However, traditional lens antennas are heavy and costly, and suffer from inherent reflection losses when made using high refractive index materials. In this regard, the lens arrays are attractive alternatives due to their planar geometry, simple fabrication process, and low profile. The concept of planar lens array has been addressed by a number of researchers and reported extensively, see for example [84][85][10][13]. In these works, focusing is obtained by using arrays of receive and transmit antennas which are connected by transmission line sections of appropriate lengths. Hollung et al. [8] also use the same method to design an active lens array, in which they integrate amplifiers in the path between the receive and transmit elements.

An alternative approach that has also been outlined in [85] is based on using a modified version of frequency-selective surfaces (FSS), in which the resonant unit cells are de-tuned to provide the required phase translation between the spherical and planar wavefronts. In the simple cases of the first and second order FSS's examined in [85], the author concludes that the FSS technique fails, because sufficient phase transition between the input and output wavefronts cannot be achieved in the passband. However, as will be shown in this chapter, this deficiency can be circumvented by using antenna-filter-antenna (AFA) arrays with higher-order filter response (see Chap. 4). While an array based on a single type of third-order AFA elements can be used to achieve a phase translations of $0 - 180°$, a combined architecture based on two types of third-order AFA's can achieve phase translations of nearly $0 - 360°$, which is required for implementing the wave transformation in the larger arrays.

Using AFA elements in the lens array results in a bandpass transfer function. This bandpass characteristic is desirable for radar and power combining applications, where it can eliminate the need for the bandpass filters in the transmit and receive paths. This is especially useful in high-power applications, where the distributed nature of the AFA array can improve the power-handling and heat dissipation in the structure. Due to its dual functions of filtering and focusing, the AFA based lens is referred to as the Filter-Lens Array (FLA). This chapter describes the theory, design process, and analysis of FLA's. A Ka-band array is designed, fabricated, and measured to demonstrate the functionality of the FLA concept.

5.2 Wave Transformation Using An Array of Scaled AFA's

In terms of wave optics, a convex lens can be described as a device that transforms a diverging input spherical wave into a plane wave at the output, or an input plane wave into a converging spherical wave at the output [86]. In an AFA array, the wave transformation is achieved by modifying the received phase distribution through the phase-delay of the AFA modules (Fig. 5.1). In an array with optimal cell size (see Sec. 1.4.1), the input-output phase-delay in each cell is a function of frequency, and can be written in terms of the S-parameters of the AFA cell[1]:

$$\Phi_m(\omega) = -\angle S_{21}^m(\omega) \tag{5.1}$$

where m is the cell index. To achieve the desired wave transformation at a given frequency ω_0, the AFA modules must be designed to provide the necessary phase-delay at that frequency.

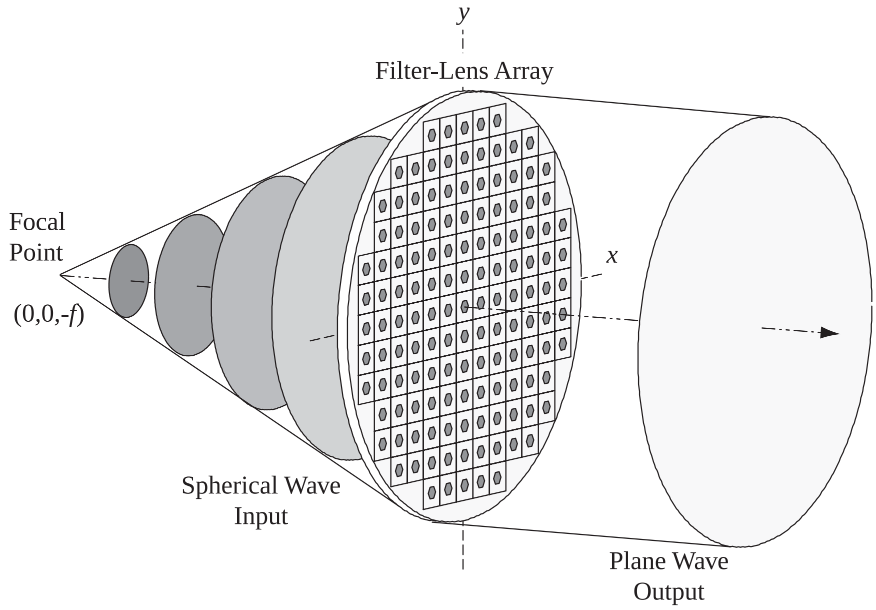

Figure 5.1: Wave transformation using a planar AFA array.

One way to achieve AFA elements with different values of phase-delay is to use scaled versions of a single design. This concept is illustrated in Fig. 5.2a, where scaled versions of the Type-I AFA are used (see Sec. 4.3.2). As a direct result of Maxwell's equations, the frequency response of the scaled AFA can be simply obtained by scaling of the frequency variable proportionally. For a scaling factor of α this gives:

$$S_{21}^{\alpha}(\omega) = S_{21}(\alpha\omega). \tag{5.2}$$

---

[1] In this text, sometimes we use the term phase-translation to refer to $\angle S_{21}$, as opposed to the phase-delay which is defined by $-\angle S_{21}$.

In practical circumstances, where the scaling is possible only in transversal dimensions and the substrate and metal thicknesses and the cell area cannot be changed from one cell to another, (5.2) is no longer an exact relation and holds only for the scaling factors near unity. For $0.97 \leq \alpha \leq 1.03$ and on a 500 μm-thick substrate, the required change in the thickness would be within ± 15 μm, which is of the order of the random thickness variations across the wafer. Also a $\pm 3\%$ change in cell size has no considerable impact on the frequency response. Therefore, for these values of α, (5.2) still represents a good approximation. Fig. 5.2b and c show the amplitude and phase of S_{21} for the scaled Type-I elements. It is observed that at 35 GHz, nearly 180° of phase-shift can be achieved by scaling, with less than 1 dB change in the amplitude response. This value of phase shift, which is limited by the in-band phase variations of the 3-pole AFA response, is not enough for fast lenses with small f/D. To increase the phase-shift, one way is resorting to higher-order AFA elements (5-pole or higher), but such elements are generally very lossy. The preferred approach is to combine two types of 3-pole AFA elements in the array. This will be explained in the next section.

5.3 Phase Response of The Type-I and Type-II AFA's

In Chapter 4 we designed two types of 3-pole bandpass AFA elements. Type-I element with a Chebyshev frequency response (Sec 4.3.2), and Type-II element with transmission zeros in the lower rejection band (Sec. 4.3.3). For the FLA design purpose, the interesting difference between these two types of elements is in the phase response, where the Type-II element shows an additional phase-delay (of theoretically 180°). This additional delay is due to the special topology of the CPW resonator in Type-II element which results in an out-of-phase coupling to the receive and transmit

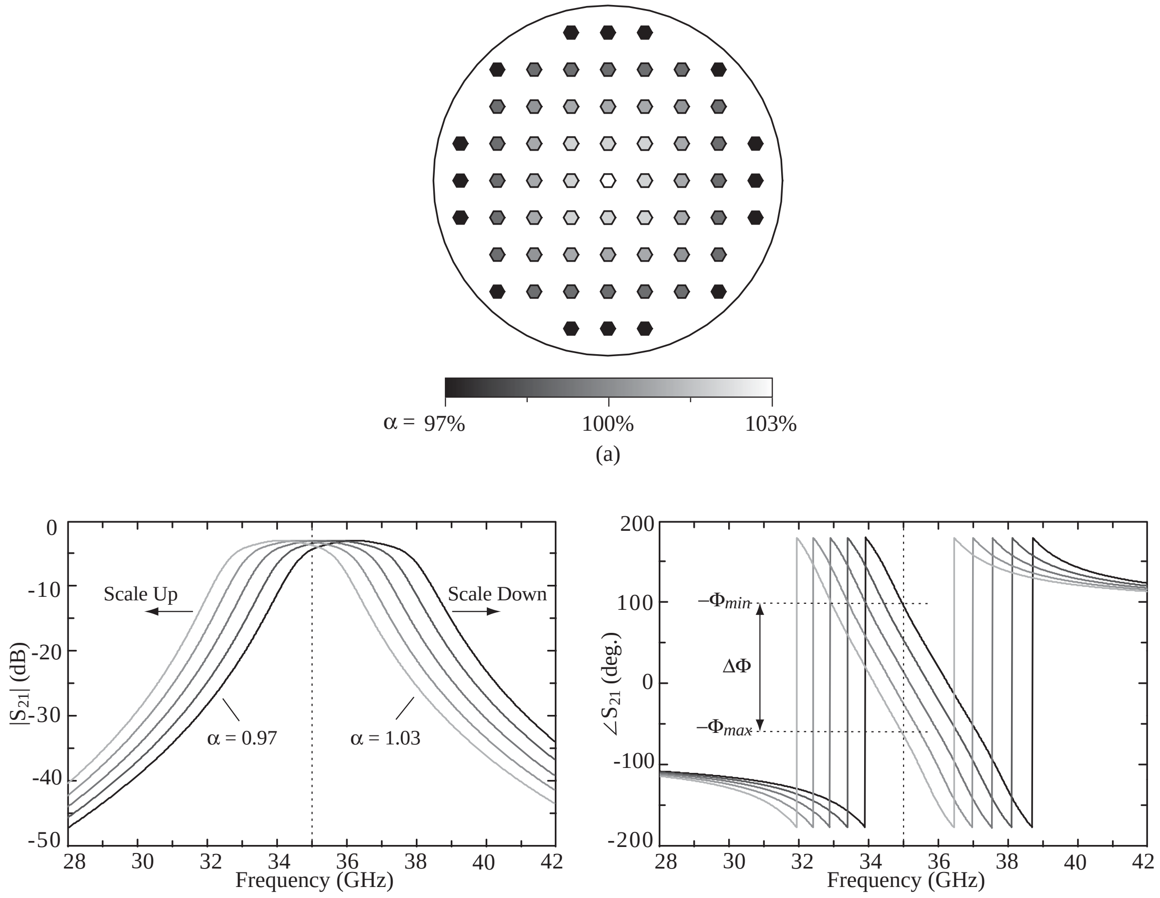

(a)

(b)

(c)

Figure 5.2: Filter-Lens Array using scaled AFA elements: a) a convex FLA using Type-I AFA cells, b) the amplitude response of the scaled AFA's, c) phase response.

antennas (see Fig. 4.7).

Fig. 5.3 shows the amplitude and phase of $S_{21}(\omega)$ for the Type-I and Type-II elements, based on the measurements of the corresponding FSS structures. To avoid the high insertion-loss and frequency offset in the final measured sample of the Type-II AFA, as reported in Sec. 4.8 (see Fig. 4.17), an earlier version is used in the design of FLA, for which the measured results are presented in Fig. 5.3b. Since the mid-band insertion-loss for the Type-I design is 3.0 dB, the edges of the 1-dB pass-band for both designs are defined as the frequencies where the $|S_{21}|$ drops below -4.0 dB (indicated by the marker lines). For each design, variations of $\angle S_{21}$ in the 1-dB pass-band determine the maximum value of phase-shift that can be achieved using scaling.

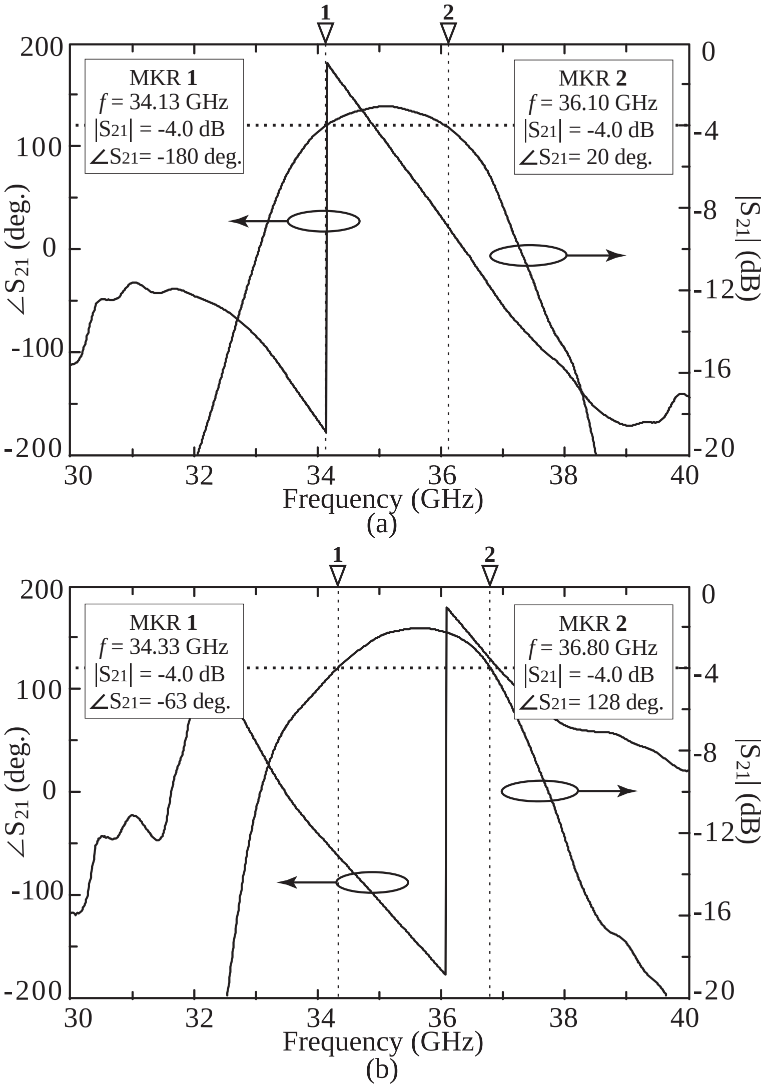

Figure 5.3: Measured magnitude and phase of S_{21} in two types of AFA elements: a) Type-I element, b) Type-II element.

Table 5.1 summarizes the important pass-band parameters for the two types of AFA. It should be noticed that the measured values of phase for the Type-II AFA do *not* represent the actual values of phase-delay due to the ambiguous unwrapping of phase in the band-limited measurement (not measured from DC). Based on physical reasons, the actual phase-delay of the Type-II design is believed to be higher than that of the Type-I design. However, to obtain a continuous range of phase-translations, the phase of the Type-II AFA is interpreted as leading that of the Type-I AFA. Such a selective interpretation, which is the result of adding integer multiples of 360° to the phase response, is permissible as long as a narrow-band operation is concerned. Based on this choice, phase-translations in the range of $-63°$ to $-340°$ can be achieved with an insertion-loss of $\leq$ 4 dB, by using scaled versions of the two type of elements. Although this is less than the theoretically required value of 360°, it proves to be sufficient for most practical purposes, where a proper design can minimize the effect of the phase errors.

AFA Element	Type-I	Type-II
Center Frequency (GHz)	35.1	35.5
1-dB Bandwidth (GHz)	2.0	2.5
Mid-band Insertion Loss (dB)	3.0	2.1
Min. In-band Phase (deg.)	-180	-63
Max. In-band Phase (deg.)	-340	-232
Combined Phase Variation (deg.)	277	

Table 5.1: Measured pass-band parameters of the Type-I and Type-II AFA's.

5.4 FLA Design

When the AFA elements are designed and characterized, design of the FLA becomes straightforward. The cell size is determined according to the design rules in Sec. 4.4.1, and the corresponding array grid is formed. If we assume that the receive aperture of the FLA lies at the xy plane, a spherical wave emerging from the focal point, $(x_f, y_f, z_f) = (0, 0, -f)$, can be written as:

$$w_1(x,y,z) = A_1 \frac{1}{\sqrt{x^2+y^2+(z+f)^2}} e^{-j\frac{2\pi}{\lambda_0}\sqrt{x^2+y^2+(z+f)^2}} \tag{5.3}$$

where A_1 is the complex amplitude, λ_0 is the free-space wavelength, and a time variation of $e^{j\omega_0 t}$ has been assumed. For a plane wave output of:

$$w_2(x,y,z) = A_2 e^{-j\frac{2\pi}{\lambda_0}(z+f)} \tag{5.4}$$

the required transmittance function between the input and output apertures of an FLA structure with the total thickness of $2h$ (see Fig. 4.4) is given by:

$$\tau(x,y) = \frac{w_2(x,y,2h)}{w_1(x,y,0)} = \left|\frac{A_2}{A_1}\right| \sqrt{x^2+y^2+f^2} e^{j\frac{2\pi}{\lambda_0}\left[\sqrt{x^2+y^2+f^2}-f\right]+j\Phi_0} \tag{5.5}$$

where Φ_0 is an arbitrary constant phase. For $f/D \geq 1$, the variations in the amplitude of (5.5) are within 12%, and can be neglected for most practical purposes. The phase relationship is enforced at each cell m with the center coordinates of $(x_m, y_m, 0)$, as follows:

$$-\Phi_m = \angle S_{21}^{m}(\omega_0) = \frac{2\pi}{\lambda_0}\left[\sqrt{x_m^2+y_m^2+f^2}-f\right] + \Phi_0. \tag{5.6}$$

Assuming that the m'th cell is a scaled version of the Type-I_m AFA ($I_m =$ I,II) with the scaling factor α_m, (5.6) can be written as:

$$\angle S_{21}^{I_m}(\alpha_m\omega_0) = \frac{2\pi}{\lambda_0}\left[\sqrt{x_m^2+y_m^2+f^2}-f\right] + \Phi_0 \tag{5.7}$$

where $S_{21}^{I_m}$ is the forward-path S-parameter. Hence, the design task becomes to determine I_m and α_m which satisfy (5.7), for each cell m. The arbitrary constant Φ_0 is selected so as to minimize the maximum required value of scaling ($\max\{|\alpha_m - 1|\}$). The design process can be programmed as following:

1. Design the AFA elements and tabulate the (measured or simulated) values of

$S_{21}(\omega)$ vs. frequency. Choose a consistent unwrapping method for tabulating the phase response.

2. Determine the pass-band, and the range of phase-delays that can be achieved using each type of element, as well as the combined range $[\Phi_{\min}, \Phi_{\max}]$.
3. Choose the size of the FLA and focal distance. The array cell area is set equal to the radiative aperture of the antennas in the AFA elements given by (4.3). Calculate the array grid based on this cell area.
4. Determine the required value of phase-delay for each cell from (5.6). Choose the arbitrary constant Φ_0 to center the required range of Φ_m in the middle of the combined range of achievable phase-delays. This minimizes the required scaling.
5. If the achievable range is considerably smaller than the required range of phase-delays, choose Φ_0 so that the achievable range covers the lower part of the required values ($\max(\Phi_m) = \Phi_{max}$). This minimizes the phase-error at the center of the lens, and expectedly reduces the adverse effects on the sidelobe-level.
6. For each cell m, solve (5.7): determine type of the element (I_m) which achieves the required phase-delay at a frequency ω_m within its pass-band, and calculate $\alpha_m = \omega_m/\omega_0$. If both types can be used, chose the one which has the lowest insertion loss or the one which results in a smaller $|\alpha_m - 1|$.

This procedure has been used to design a circular FLA with $f = 10$ cm and $D = 7.8$ cm (for fabrication on 3 inch glass wafers). This FLA is based on the previously developed Type-I and Type-II AFA elements, and is designed to operate at 35 GHz. With a square grid and a cell area of 29.6 mm^2 (side length $l_c = 5.44$ mm), a total of 137 elements can be fitted in the area of this lens. The array grid and AFA cells are presented in Fig. 5.4a, where the two types of elements appear in different gray levels. Fig. 5.4b shows the calculated scaling factor and element type as a function of the distance from the center.

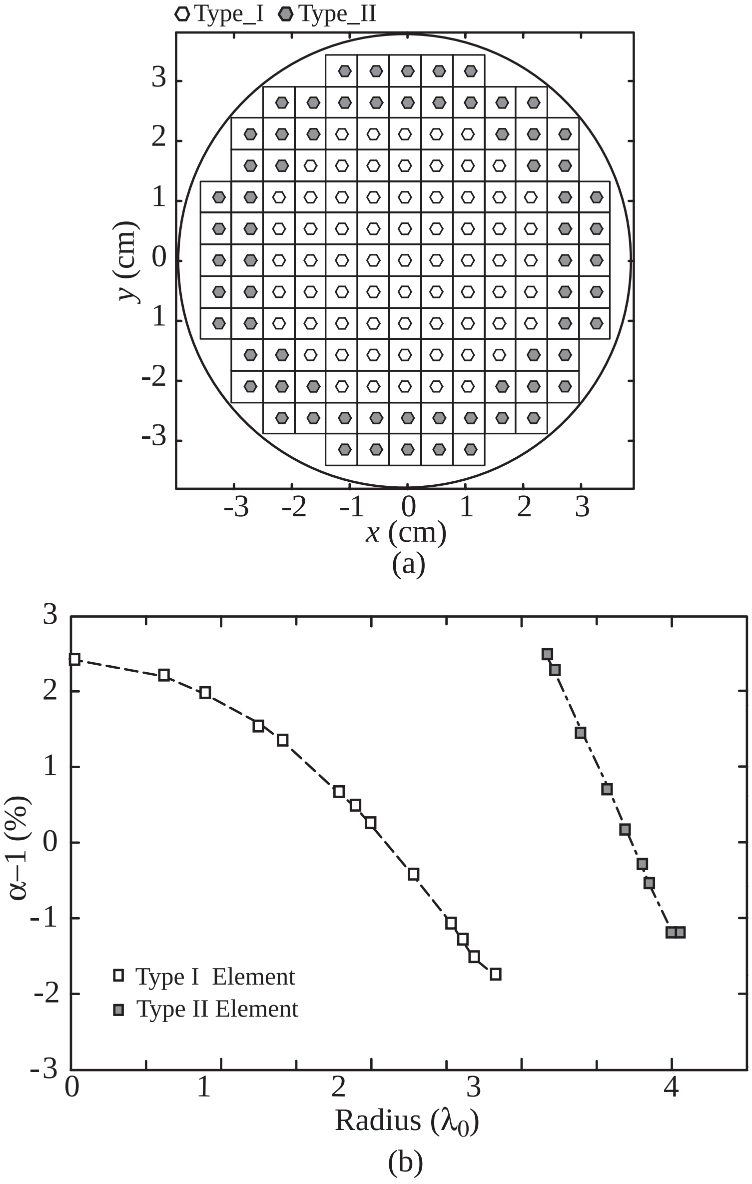

Figure 5.4: A 3-inch FLA using Type-I and Type-II elements: a) array grid geometry, b) type and scaling factor of the AFA elements.

5.5 Analysis

A simple analysis of the FLA can be performed by using basic antenna and array concepts. This analysis neglects the mutual coupling between antennas, and assumes that the frequency response of the AFA elements has no strong dependence on the angle of incidence. While the former is generally true for arrays with large cell size, as it is usually the case for AFA arrays, the latter is valid only if the subtended angle of the lens (from the focal point) does not exceed $20° - 30°$. Also, for the analysis purposes we consider FLA in the transmit mode. However, due to reciprocity, the results will be valid for both transmit and receive modes of operation.

Assume that the FLA is a circular disc of diameter D and is illuminated by an antenna at the focal point $(0, 0, -f)$ and having the directional gain of $G_f(\vartheta, \varphi)$. For the unit input power, the power received by the m'th element in the array is given by:

$$P_{rec}^m = \frac{1}{4\pi r_m^2} G_f(\vartheta_m, \varphi_m) A_r(\vartheta_m, \varphi_m) \tag{5.8}$$

where:

$$\begin{aligned} r_m &= \sqrt{x_m^2 + y_m^2 + f^2}, \\ \vartheta_m &= \tan^{-1} \frac{\sqrt{x_m^2 + y_m^2}}{f}, \\ \varphi_m &= \frac{y_m}{|y_m|} \cos^{-1} \frac{x_m}{\sqrt{x_m^2 + y_m^2}}. \end{aligned} \tag{5.9}$$

A_r is the radiative aperture of the antenna in the AFA element, and is related to the directivity of the patch antennas in the AFA elements, $D_e(\vartheta, \varphi)$, through (4.3). Borrowing the notation of the two-port scattering parameters, the incident wave at the input port (port 1) of the m'th element, can be written as:

$$a_1^m = \sqrt{P_{rec}^m} e^{-j\frac{2\pi}{\lambda} r_m} \tag{5.10}$$

where a phase factor is introduced to account for the propagation delay between the feed and AFA receive antennas. The outgoing wave at the output port (port 2) of AFA is given by:

$$b_2^m = S_{21}^m(\omega) \cdot a_1^m = S_{21}^{I_m}(\alpha_m \omega) \cdot a_1^m. \tag{5.11}$$

Combining (5.8), (4.3),(5.10) and (5.11), we obtain the following expression:

$$b_2^m = \frac{\lambda}{4\pi r_m} \cdot \sqrt{G_f(\vartheta_m, \varphi_m) D_e(\vartheta_m, \varphi_m)} \cdot e^{-j\frac{2\pi}{\lambda} r_m} \cdot S_{21}^{I_m}(\alpha_m \omega). \tag{5.12}$$

The values of b_m are proportional to the amplitude of the current distribution over the patches on the transmit side of the FLA[2], and can be considered as the output array coefficients. The radiated power density at a point (r, ϑ, φ) in the far-field is calculated from:

$$S(\vartheta, \varphi) = \frac{1}{4\pi r^2} D_e(\vartheta, \varphi) \left| \sum b_2^m \; e^{j\frac{2\pi}{\lambda}\sqrt{x_m^2 + y_m^2} \sin\vartheta \cos(\varphi - \varphi_m))} \right|^2. \tag{5.13}$$

where the summation is over all AFA elements. If the interaction between the radiating elements is neglected, the total radiated power is given by:

$$P_{out} = \sum |b_2^m|^2. \tag{5.14}$$

Directivity of the FLA is defined as the ratio of the radiated power density to what would have been obtained from the isotropic radiation of the output power:

$$D(\vartheta, \varphi) = \frac{1}{P_{out}/4\pi r^2} S(\vartheta, \varphi) = D_e(\vartheta, \varphi) \frac{\left| \sum b_2^m \; e^{j\frac{2\pi}{\lambda} \sin\vartheta \cos(\varphi - \varphi_m)} \right|^2}{\sum |b_2^m|^2}. \tag{5.15}$$

The FLA *Power Transfer Ratio* (PTR) can be defined as:

$$T_{FLA}(\omega) = \frac{P_{out}}{P_{rec}} = \frac{\sum |b_2^m|^2}{\sum |a_2^m|^2} \tag{5.16}$$

---

[2] The transmit side is sometimes referred to as the non-feed side [10], which is generally a more exact expression.

where P_{rec} is the total power *intercepted* by the FLA. $T_{FLA}(\omega)$ represents the combined frequency response of the AFA array, including the internal losses of the FLA structure. Besides these and the losses in the feed antenna (included in G_f), the only additional source of loss is the spill-over. This loss can be included by introducing a spill-over efficiency factor:

$$\eta_{SO} = \frac{P_{rec}}{1} = \sum |a_2^m|^2. \tag{5.17}$$

Even if an optimal feed antenna is used (see. (5.21)), the spill-over loss still will be present, due to the incomplete coverage of the circular illumination area of the FLA by the square AFA cells. Gain of the FLA is defined similar to its directivity, except it is measured against the input power (equal to 1 in this case):

$$G(\vartheta, \varphi) = \frac{1}{1/4\pi r^2} S(\vartheta, \varphi) = D_e(\vartheta, \varphi) \left| \sum b_2^m \; e^{j\frac{2\pi}{\lambda}\sin\vartheta\cos(\varphi-\varphi_m)} \right|^2. \tag{5.18}$$

This gain is related to the spill-over efficiency, PTR, and FLA directivity as follows:

$$G(\vartheta, \varphi) = \eta_{SO} \cdot T_{FLA}(\omega) \cdot D(\vartheta, \varphi). \tag{5.19}$$

The filtering response of the FLA can be characterized by considering the variations of the maximum gain, $G(0,0)$, as a function of frequency. This is referred to as the *Gain Response*, and written as:

$$G_{max}(\omega) = D_e(0,0) \left| \sum b_2^m \right|^2. \tag{5.20}$$

It is evident from the above derivations that the FLA gain, directivity, and even PTR depend not only on the FLA itself, but also on the gain of the feed antenna. To establish a reference we assume an optimal feed antenna with:

$$G_f^{opt}(\vartheta, \varphi) = \begin{cases} G_{f0} = \dfrac{2}{1-\cos\vartheta_{sub}} & , \vartheta \le \vartheta_{sub} \\ 0 & , \text{elsewhere} \end{cases} \tag{5.21}$$

where ϑ_{sub} is the lens subtended angle:

$$\vartheta_{sub} = \tan^{-1} \frac{D}{2f} \tag{5.22}$$

and assess the performance of the FLA under the ideal circumstances. In this case, the overall FLA gain is proportional to G_{f0} and can be expressed as following:

$$G(\vartheta, \varphi) = G^{opt}(\vartheta, \varphi) = G_{f0} \cdot G_{FLA}(\vartheta, \varphi) \tag{5.23}$$

in which G_{FLA} is obtained from (5.12) and (5.18) with $G_f(\vartheta_m, \varphi_m) = 1$, and can be interpreted as the *focusing gain* of the FLA under optimal feed illumination. For a general feed pattern, the FLA gain can be written as:

$$G(\vartheta, \varphi) = \langle G_f \rangle \cdot \eta_T \cdot G_{FLA}(\vartheta, \varphi) \tag{5.24}$$

where:

$$\langle G_f \rangle = \frac{\int_0^{2\pi} \int_0^{\vartheta_{sub}} G_f(\vartheta, \varphi) \sin\vartheta \; d\vartheta d\varphi}{\int_0^{2\pi} \int_0^{\vartheta_{sub}} \sin\vartheta \; d\vartheta d\varphi} \tag{5.25}$$

is the average feed gain within the subtended angle. η_T represents the *taper efficiency* and accounts for the variations of the focusing gain due to the non-uniform aperture illumination. It can be easily shown that:

$$\langle G_f \rangle = \eta'_{SO} \cdot \eta_f \cdot G_{f0} \tag{5.26}$$

where G_{f0} is defined in (5.21), η_f is the overall efficiency of the feed antenna, and η'_{SO} represents the *extrinsic spill-over efficiency*[3], given by:

$$\eta'_{SO} = \frac{\int_0^{2\pi} \int_0^{\vartheta_{sub}} G_f(\vartheta, \varphi) \sin\vartheta \; d\vartheta d\varphi}{\int_0^{2\pi} \int_0^{\pi} G_f(\vartheta, \varphi) \sin\vartheta \; d\vartheta d\varphi}. \tag{5.27}$$

From (5.23), (5.24), and (5.26) it is concluded that for a general feed antenna:

---

[3] The extrinsic spill-over loss is resulted from the wide-angle pattern of the feed antenna, while the intrinsic spill-over loss is caused by the non-circular boundary of the FLA.

$$G(\vartheta,\varphi) = \eta'_{SO} \cdot \eta_f \cdot \eta_T \cdot G^{opt}(\vartheta,\varphi). \tag{5.28}$$

For the rest of this chapter we assume that the FLA is excited by an optimal feed antenna, both in simulations and in presenting the measurement results. Appendix D considers the effect of using feed antennas with cosine-type patterns, which are better approximations of the actual systems.

5.6 Measurement Method

Before presenting the simulation and measurement results, we briefly describe our measurement methods in this section.

5.6.1 Pattern

The pattern measurement system used for characterizing FLA is shown in Fig. 5.5. In this system, FLA is fed by a simple open-ended waveguide (OEWG) at its focal point. A small optical bench setup is used to facilitate the fine adjustments of the feed-FLA distance, as well as the angle of the FLA. This fixture is rotated in an anechoic chamber and the radiated power is measured in the far-field using a standard horn antenna and a spectrum analyzer at the receive end. A computer program controls the positioner and the spectrum analyzer, and records the measured power. As the OEWG has a wide radiation pattern, a major portion of the input power radiates at angles $\vartheta > \vartheta_{sub}$, not intercepted by the FLA. Direct reception of this portion of power can corrupt the FLA pattern measurement. To circumvent this difficulty, the OEWG+FLA setup is enclosed in a box covered with absorber, and having a circular window of diameter D in front of the FLA.

Figure 5.6 shows the E-plane ($\varphi = 0$) measured patterns of the OEWG, and the OEWG+FLA with and without the box. It is evident that the measured radiation

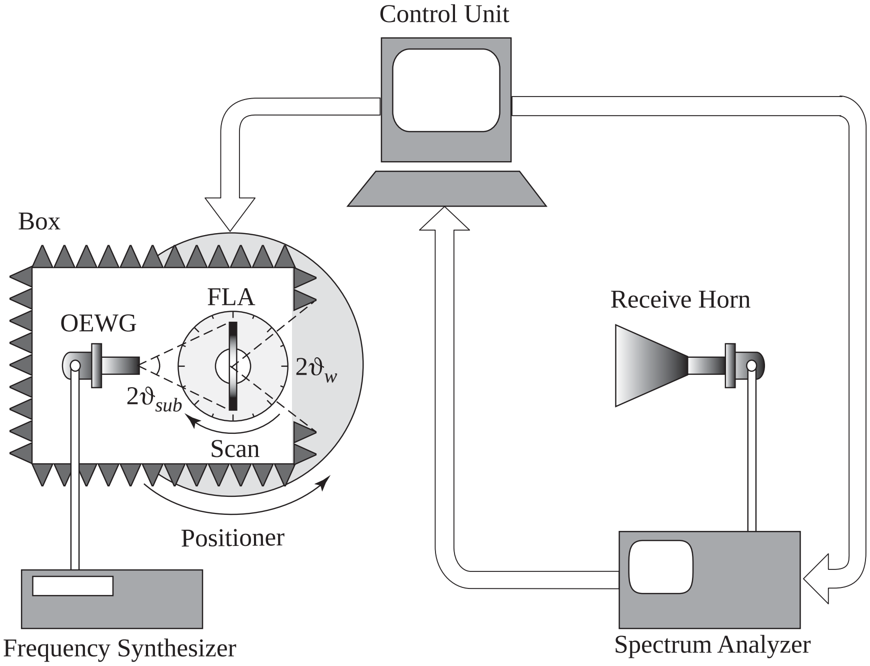

Figure 5.5: Top view of the pattern measurement setup consisting the signal source, open-ended waveguide feed, FLA, box, receive horn, spectrum analyzer, and computer controlled positioner.

pattern in the absence of the box is completely dominated by that of the OEWG for angles $\vartheta > \vartheta_{sub} = 21°$. Enclosing box has little impact on the measured radiation pattern for angles $\vartheta < \vartheta_{sub}$, but it strongly suppresses the feed radiations outside this region, theoretically leaving behind only the FLA radiations. The box is also likely to somewhat attenuate the FLA radiations for $\vartheta > \vartheta_w$ (see Fig. 5.5), which if true, can result in a rather optimistic evaluation of the sidelobe levels in this region.

In the next section, we also consider the performance of the FLA for the beam-steering systems. Beam-steering in the lens systems is generally achieved by switching the input power between an array of feed antennas, located at the focal surface. The measurement setup, described previously, can be easily modified for measuring the scanned radiation pattern of such systems. If the focal surface is approximated with a sphere of radius f and center $(0, 0, 0)$, moving the feed point over this surface this

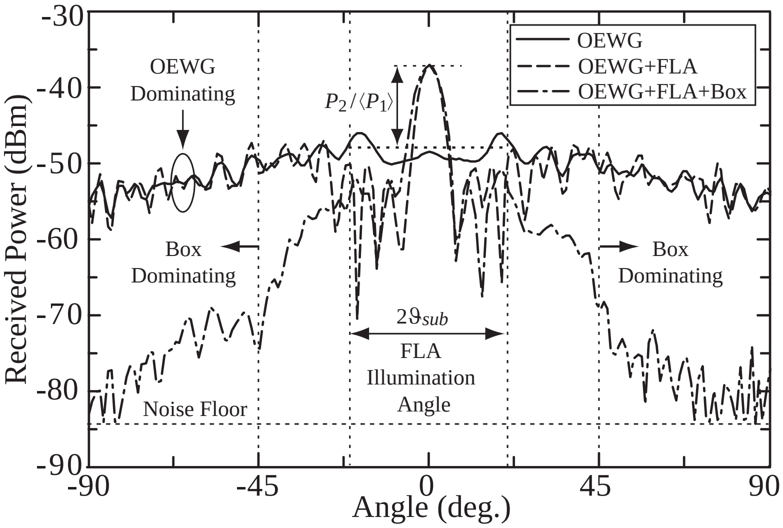

Figure 5.6: The measured radiated power (at 35 GHz) for OEWG, OEWG and FLA, and OEWG and FLA inside the box.

surface can be simulated by reorienting the FLA around its center. This is most easily performed in the constant φ planes, by re-initializing the positioner by the amount of scan angle. The FLA is then rotated by the negative of this amount around its vertical axis, so that the lens axis realigns with that of the measurement chamber. The rotary dial at the base of the FLA stand (see Fig. 5.5) serves this purpose. For a different value of φ, the OEWG feed, FLA, and receive horn are reoriented around the z-axis, and the same procedure is repeated. In addition to its simplicity, an interesting result of using such a method, is that the confinement box is always aligned with the main beam, so that the accurate measurement window of $2\vartheta_w$ symmetrically spans around ϑ_{scan}.

5.6.2 Gain

While for gain measurements it is generally required to calibrate the measurement system using a standard gain antennas or other methods, in case of FLA (or in general any lens antenna) this proves unnecessary. In fact, we would need such standard measurements if we were to measure the combined gain of the feed and FLA as a complete antenna system. However, to obtain the gain of the FLA in reference to an ideal feed system, it is sufficient to measure its focusing gain under (nearly) optimal illumination, which can be obtained from measured radiation patterns of a low-gain feed antenna with and without FLA.

Assume that the measured received power as a function of ϑ and φ is equal to $P_1(\vartheta, \varphi)$ for the feed antenna with no FLA, and is equal to $P_2(\vartheta, \varphi)$ for the combination of the feed antenna and FLA. If both measurements are performed using the same input power, P_1 and P_2 can be expressed as following:

$$\begin{aligned} P_1(\vartheta, \varphi) &= C_x \; G_f(\vartheta, \varphi) \\ P_2(\vartheta, \varphi) &= C_x \; G(\vartheta, \varphi) \end{aligned} \tag{5.29}$$

where C_x is an unknown constant which includes all common gain/loss factors between the receive and transmit ends. If the feed antenna has a nearly uniform radiation pattern in the cone of $\vartheta \leq \vartheta_{sub}$ so that $\eta_T \cong 1$, equations (5.24), (5.25) and (5.29) can be combined to give:

$$P_2(\vartheta, \varphi) = \langle P_1 \rangle \cdot G_{FLA}(\vartheta, \varphi) \tag{5.30}$$

where:

$$\langle P_1 \rangle = \frac{\int_0^{2\pi} \int_0^{\vartheta_{sub}} P_1(\vartheta, \varphi) \sin \vartheta \; d\vartheta d\varphi}{\int_0^{2\pi} \int_0^{\vartheta_{sub}} \sin \vartheta \; d\vartheta d\varphi}. \tag{5.31}$$

Equation (5.30) results in $G_{FLA} = P_2(\vartheta, \varphi)/\langle P_1 \rangle$, which can be used in (5.23) to give the FLA gain under optimal feeding conditions:

$$\begin{aligned} G^{opt}(\vartheta, \varphi) &= G_{f0} \cdot \frac{P_2(\vartheta, \varphi)}{\langle P_1 \rangle} \\ &= \frac{2}{1 - \cos \vartheta_{sub}} \cdot \frac{P_2(\vartheta, \varphi)}{\langle P_1 \rangle}. \end{aligned} \tag{5.32}$$

This equation relates the optimal gain of the FLA to the measured quantities P_1

and P_2 and can be used as a basis for extracting the FLA gain from the pattern measurements[4].

5.6.3 Gain-Response

Theoretically, gain-response of the FLA can be measured by repeating the single point measurement at the direction of the maximum gain, for different frequencies. However, as the confinement box fails to block the leakage of the power from around the FLA structure, the dynamic range of this measurement system is limited and the rejection band characteristics cannot be measured appropriately.

Alternatively, a close-range measurement setup can be designed based on a hard-horn receive antenna [81] (also see Sec. 4.7), as shown in Fig. 5.7. There is no straightforward method to calibrate this setup beyond the coax input/ouput terminals. If we can assume a flat frequency response for the coax-waveguide transitions, OEWG, and the hard horn (within the measurement band), the measured frequency response will be proportional to the gain response of the FLA under ideal feeding conditions. Therefore the measured response can be normalized to its value at ω_0, and then multiplied by the previously measured value of $G(0,0)$ at this frequency, to produce an estimation of the gain response:

$$G_{max}(\omega) = \left| \frac{S_{21}^{meas}(\omega)}{S_{21}^{meas}(\omega_0)} \right|^2 \cdot G(0,0)\,|_{\omega=\omega_0} \quad . \tag{5.33}$$

Besides the possible non-flat frequency response of the hard-horn and OEWG, the difference between the the horn and the FLA radiating apertures introduces an aperture clipping error (due to exclusion of the elements near the periphery of the FLA). At the same time, the margin between the horn aperture and the edges of the

---

[4] The focusing gain of the FLA can also be measured based on a Gaussian optics characterization, as described in Appendix E. This method, however, does not measure the spill-over and structural losses and is only good for estimating what can be better called as *focusing directivity.*

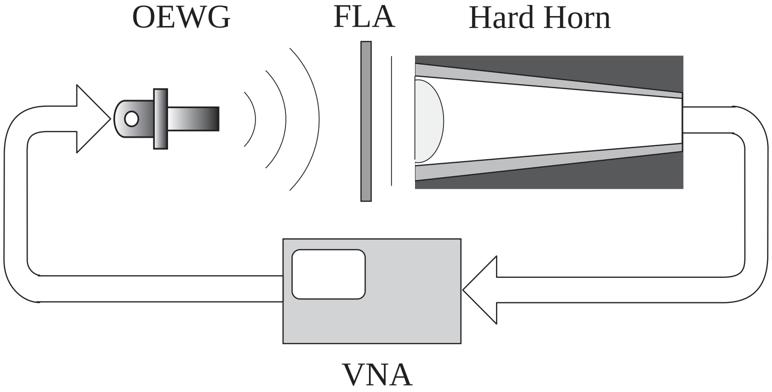

Figure 5.7: The measurement setup for the FLA gain-response.

FLA is believed to be responsible for discarding the diffraction components from the measurement, which in turn results in a larger dynamic range as compared to the far-field approach.

5.7 Results

In this section we present the simulated and measured results for the FLA designed in Sec. 5.4. The reported measurements are for a prototype which was fabricated using the procedure described in Sec. 4.6.

The array coefficients at the output of the FLA can be calculated using (5.12). The normalized coefficients $\{b_2^m/b_2^1\}$ can serve as a measure of the amplitude and phase errors across the output aperture of the FLA, as shown in Fig. 5.8, where the horizontal access shows the normalized distance from the center of the FLA $(\sqrt{x_m^2+y_m^2}/\lambda_0)$. The AFA elements which are located at the same radius have the same phase of excitation, but as they receive the feed signal from different angles with the directivities of $D_e(\vartheta_m,\varphi_m)$[5], are in general excited with different amplitudes. This results in multiple values of amplitude for some values of radius in Fig. 5.8. Also notice that two curves are shown for the amplitude, calculated based on the optimal

---

[5] D_e is the directivity of the patch antenna in the AFA element.

and measured OEWG feed patterns (see Fig. 5.6). While the phase variation is less than 10° across the output array, the amplitude error is as high as ±2 dB. In both simulations, the elements at the outer rings of the FLA have larger excitation coefficients, which is to some extent because of the lower insertion loss of the Type-II elements.

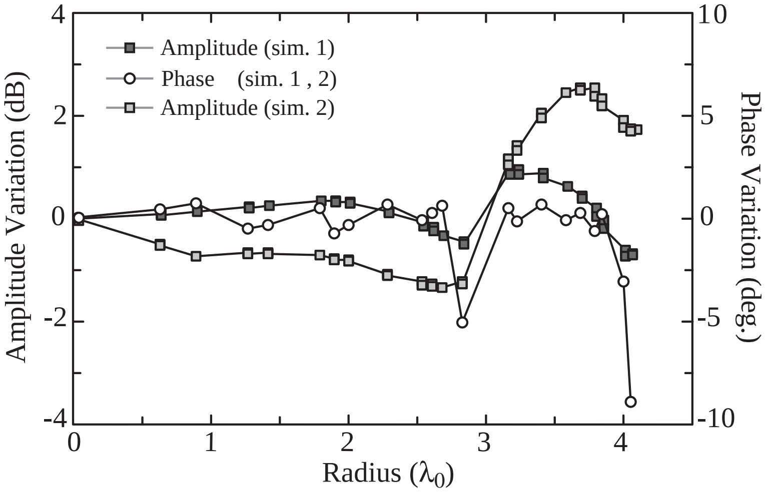

Figure 5.8: The simulated aperture distribution at the output of the FLA.

The FLA gain, $G(\vartheta, \varphi)$, can be calculated from the equations in Sec. 5.5, and measured using the method described in Sec. 5.6.2. The average value of $\langle P_1 \rangle = -48$ dBm, obtained from OEWG measurement, is used in (5.32) to extract the FLA gain from measurements. The simulated and measured gain patterns are shown in Fig. 5.9, for E- and H-planes ($\varphi = 0$ and 90° respectively). Besides the slight difference in the level of the gain in the maximum direction, the simulations almost accurately predict the radiation pattern in the mainlobe and its two nearest sidelobes. The farther sidelobes, however, are measured at significantly higher levels than predicted. This can be due to the differences in the aperture distribution, which are resulted from the nonuniform feed pattern and fabrication errors. At the same time, this can be caused by the leakage of the direct feed radiations through the walls of the confinement box, or its diffraction along the edges of the FLA (notice that nulls are filled in the measured pattern). The measured values of the maximum gain and 3-dB beam-width are 25.6 dBi and 6.4° (in both planes), vs. the simulated values of 24.8 dBi and 7.0°, respectively. Considering that directivity is approximately proportional to $1/\vartheta_{3-dB}^2$, the 0.8 dB difference in gain is consistent with the nearly 9% difference in the 3-dB beam-widths. The measured sidelobe level is -14 dB in E-plane, and -17 dB in H-plane.

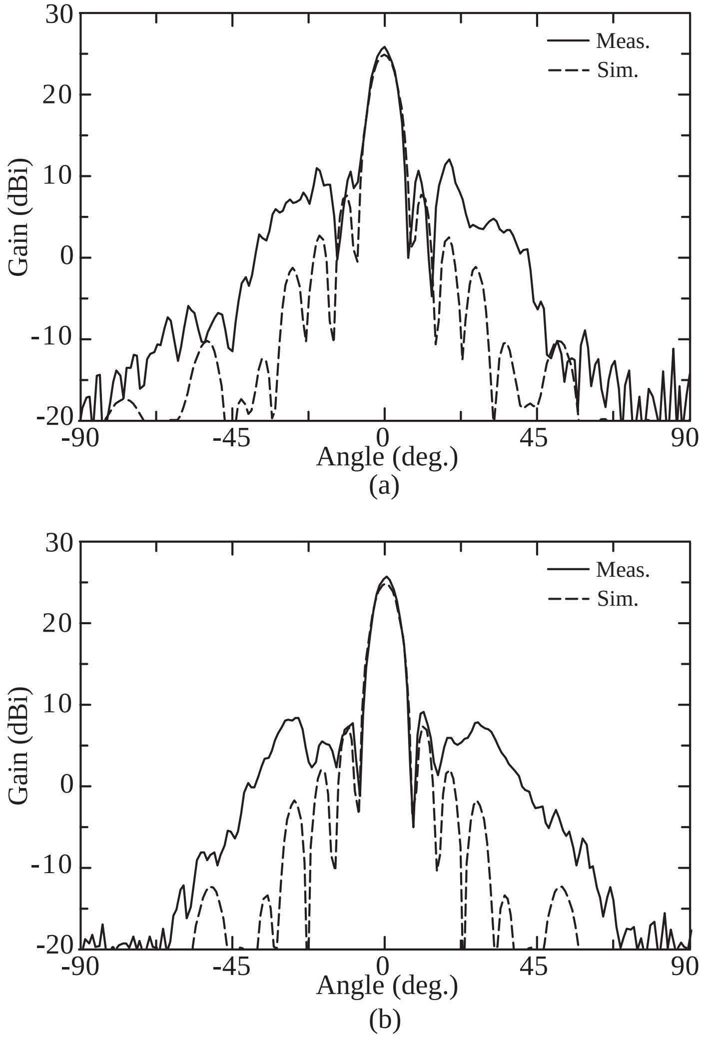

Figure 5.9: Measured gain pattern of the FLA at 35 GHz: a) E-plane, and b) H-planes patterns.

It is important to estimate the efficiency of the FLA and determine the sources of loss. This can be done by comparing the gain of the FLA with the directivity of an ideal uniform aperture of same area. Assuming a uniform aperture distribution, the ideal directivity is related to the aperture area A through [77]:

$$D_{max} = \frac{4\pi}{\lambda_0^2} A. \tag{5.34}$$

For a circular aperture of diameter 7.8 cm ($A = 47.8$ cm^2) at 35 GHz, a directivity of 29.1 dBi is calculated using this formula. The actual area occupied by the AFA elements, however, is equal to $137A_c = 40.55$ cm^2 in the present design, which results in a theoretical directivity of 28.4 dBi (0.7 dB spill-over loss). The calculated value η_{SO} is -0.74 dB based on (5.17). The remaining difference between the measured gain and the maximum directivity is -2.8 dBi, which can be attributed to the collective effect of the aperture amplitude and phase errors, as well as the the FLA power transfer ratio (PTR). A simulation based on the measured pattern of the OEWG, results in a PTR of -2.8 dB, which perfectly agrees with this observation. Based on these values, the overall estimated efficiency of the FLA with an ideal feed is equal to -3.5 dB or 45%[6]. These results and some other specifications of the designed FLA are summarized in Table 5.2.

Figure 5.10 presents the simulated and measured gain response of the FLA. The measurement is performed using the system described in Sec. 5.6.3, and the result is renormalized for $G_{max} = 25.6$ dBi at 35 GHz. The outcome is a gain response which is very similar to what is predicted using the theory of Sec. 5.5. According to these results, when the FLA is fed by an optimal feed, it is equivalent to the combination of a lossless lens with 29.1 dB of directivity, and bandpass filter with 8.2% bandwidth at 35.3 GHz and 3.5 dB mid-band insertion-loss (equal to $\eta_{SO} \cdot T_{FLA}(\omega_0)$). The FLA filtering performance data are summarized in Table 5.3.

The last step in evaluating the designed FLA is considering its scanning perfor-

---

[6] For a practical feed with a $\cos^n$ with -10 dB of edge-taper ($n = 37$), the FLA efficiency reduces to 41%.

Aperture Size (λ^2)	65
F-Number (f/D)	1.25
Gain (dBi)	25.6
HPBW (deg.)	6.4
SLL E-Plane (dB)	-14
SLL H-Plane (dB)	-17
η_{SO} (dB)	-0.7
T_{FLA} (dB)	-2.8
Power Efficiency	45%

Table 5.2: Radiation performance data for the FLA at 35 GHz.

Center Frequency (GHz)	35.25
Mid-band Directivity (dBi)	29.1
Mid-band Insertion-Loss (dB)	3.5
3-dB Gain Bandwidth	8.2%
20-dB Rejection-Band Edges (GHz)	32, 38.8

Table 5.3: Filtering performance data of the FLA.

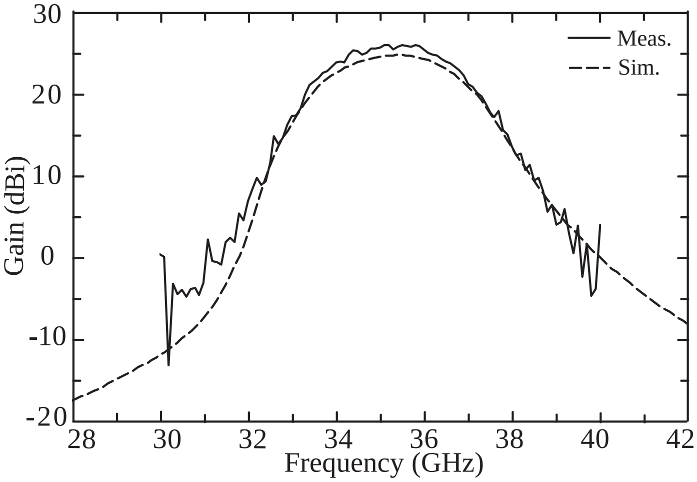

Figure 5.10: Gain response of the FLA.

mance. A simple focal-plane scanning (FPS) system based on FLA is illustrated in Fig. 5.11. In the transmit mode, for example, the input RF signal is switched between different feed antennas which form a feed matrix at the focal surface of the FLA. For best performance, the feed elements are oriented so that their main-beams are towards the center of the FLA. For each feed, the output is a confined beam in the direction of the line connecting it to the FLA center, resulting a switchable multi-beam system. However, since the functionality of the FLA quickly deteriorates by displacing the feed antenna from the focal point, the gain drops and sidelobes increase by increasing the scan-angle. Besides the non-ideal wave transformation for the off-axis waves which is a main source of the imperfection, the FLA performance can also be limited by the behavior of the AFA elements at oblique angles of incidence.

Scanning pattern measurements can be carried out using a single feed antenna and the method described in Sec. 5.6.1. We have measured the FLA at 6 states of scanning ($\vartheta_{scan} = \pm 10°, \pm 20°$, and $\pm 30°$), in each principal plane. The resulting measured radiation patterns are presented in Figs. 5.12 and 5.13, along with simulations. While the simulated patterns generally follow the measured results nicely, it is observed that with moving from boresight, the measured gain drops faster than the simulated gain.

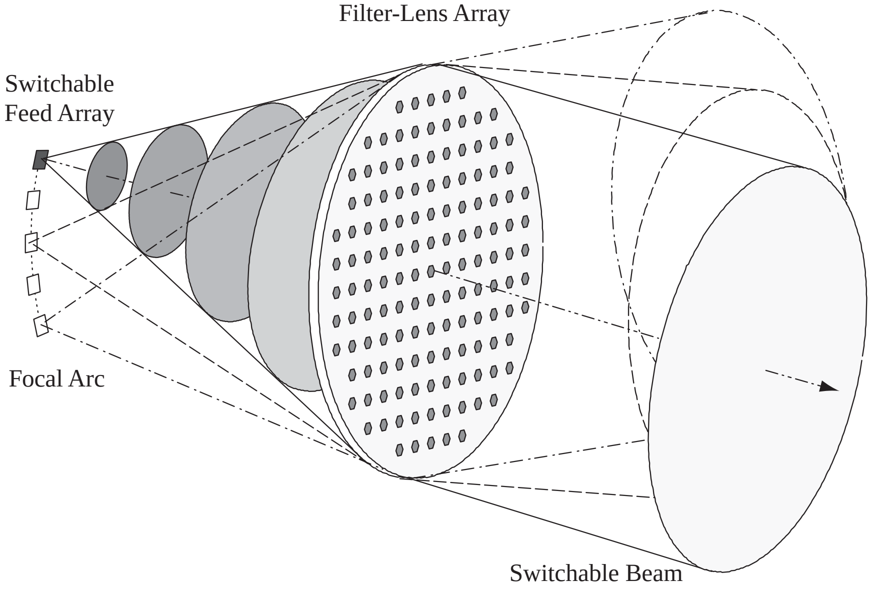

Figure 5.11: A focal plane scanning system using FLA.

The reason for the higher measured scan loss is the degradation in the frequency response of the AFA elements at oblique angles of incidence, which is not included in the simulations.

Maximum gain, 3-dB beam-width, and sidelobe-level are listed for different values of the scan angle in Table 5.4. A better scanning performance is observed in the H-plane, where the main beam receives a scanning loss of less than 3.6 dB at $\vartheta_{scan} = \pm 30°$, vs. in the E-plane where it receives nearly 4.5 dB of loss at $\vartheta_{scan} = \pm 20°$. For $\vartheta_{scan} = \pm 30°$ in the E-plane, the attenuation is so high that basically suppresses the output beam. This can be explained by the behavior of the surface-waves in the FLA structure[7]. According to the theory in Sec. 4.4.2, the two dominant surface-wave modes are $\text{TM}_{\pm 1,0,1}$ and $\text{TM}_{0,\pm 1,1}$. A scanned beam in the E-plane ($\varphi = 0$), is essentially TM and can strongly couple to the $\text{TM}_{\pm 1,0,1}$ modes, resulting in a loss component which increases with the scan angle. Particularly, for $\vartheta_{scan} = \pm 30°$, the

---

[7] Although FLA is not a truly periodic structure, it is almost periodic and therefore the its surface-wave modes are approximately the same as those of the FSS structure. However, the surface-waves are expected to be stronger in the output array, where the electromagnetic field is predominantly a plane wave.

surface-wave modes creates a transmission-null at 35.5 GHz (see Sec. 4.4.2) which almost eliminates the main-beam. On the other hand, a scanned beam in the H-plane ($\varphi = 90°$) is predominantly a TE wave and does not couple to the $\mathrm{TM}_{0,\pm1,1}$ modes considerably, resulting in a lower scan-loss in this case.

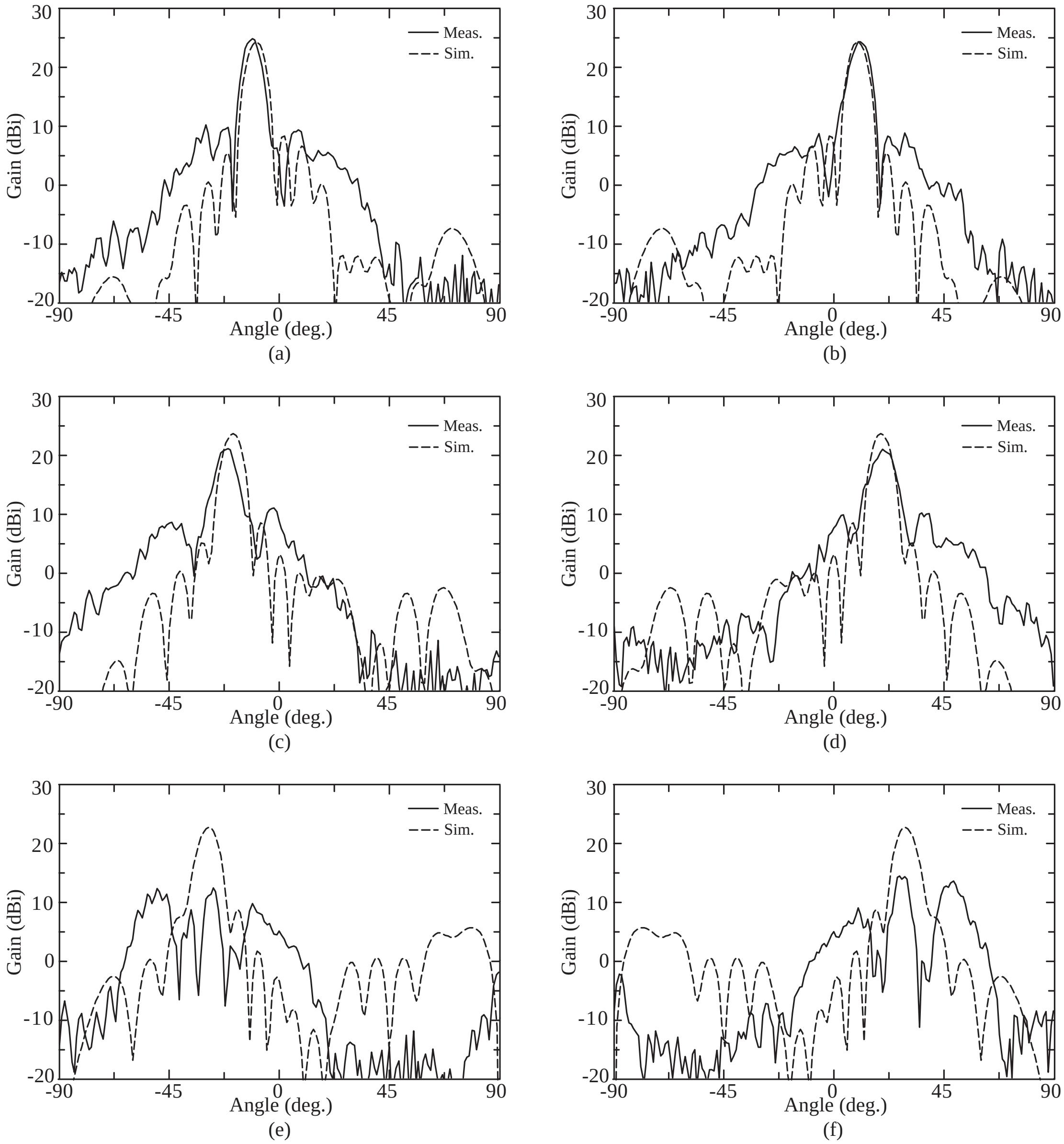

Figure 5.12: The gain pattern of FLA in the E-plane ($\varphi = 0$) for different values of scan angle, a) $\vartheta_{scan} = -10°$, b) $\vartheta_{scan} = 10°$, c) $\vartheta_{scan} = -20°$, d) $\vartheta_{scan} = 20°$, e) $\vartheta_{scan} = -30°$, and f) $\vartheta_{scan} = 30°$.

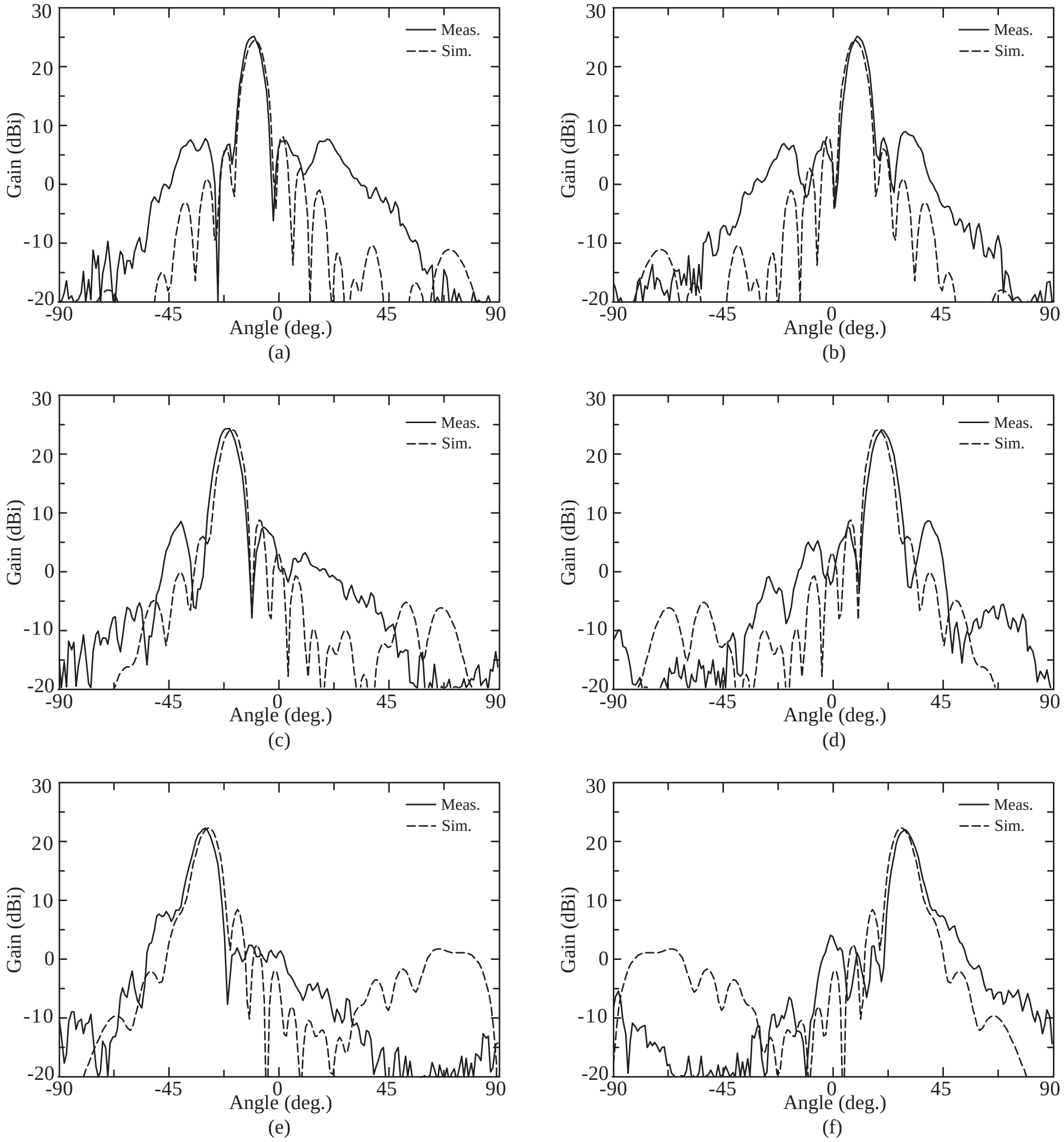

Figure 5.13: The gain pattern of FLA in the H-plane ($\varphi = 90°$) for different values of scan angle, a) $\vartheta_{scan} = -10°$, b) $\vartheta_{scan} = 10°$, c) $\vartheta_{scan} = -20°$, d) $\vartheta_{scan} = 20°$, e) $\vartheta_{scan} = -30°$, and f) $\vartheta_{scan} = 30°$.

5.8 Conclusion

The novel concept of Filter-Lens Array was introduced in this chapter. FLA is a planar array of AFA elements, which combines the filtering and focusing functions.

Scan Angle (deg.)	Gain (dBi)		HPBW (deg.)		SLL (dB)	
	E-Plane	H-Plane	E-Plane	H-Plane	E-Plane	H-Plane
-30	-	22.3	-	7.8	-	-15
-20	21.2	24.2	7.1	7.4	-11	-16
-10	24.9	25.2	5.6	6.5	-15	-18
0	25.6	25.6	6.4	6.4	-14	-17
+10	24.4	25.2	7.1	6.7	-16	-16
+20	21.0	23.8	8.8	7.6	-11	-16
+30	-	22.0	-	8.1	-	-14

Table 5.4: Scanning performance data of the FLA at 35 GHz.

Design, analysis, and measurement methods were developed and used to implement and characterize a Ka-band FLA, based on the bandpass AFA elements of Chapter 3. With an f/D of 1.25, the designed FLA shows 11 dB of focusing gain at 35 GHz, which translates to a total of 25.6 dBi in combination with an optimal feed antenna, and it has a 8.2% gain-bandwidth centered 35.2 GHz. This FLA was also tested for beam-steering, where it was able to sustain a gain of > 22 dBi and a sidelobe-level of < -14 dB for the scanning angles of up to $\pm 30°$. The total efficiency is estimated as $40 - 50\%$ at 35 GHz, when the FLA is used in the boresight.

According to these results, a properly designed FLA can meet the system requirements for a wide range of applications. FLA's present a compact, simple, and efficient means of focusing and filtering at millimeter-wave frequencies, and can replace the standard combinations of dielectric lenses and bandpass filters. They are expected to find application in power combining, medium-angle beam-steering, and millimeter-wave imaging systems.

CHAPTER 6

Conclusion

This thesis introduces novel antenna and filter concepts for application in millimeter-wave passive front-ends. This includes planar interleaved-subarray antennas, MEMS tunable filters, integrated antenna-filter-antenna elements and arrays, and planar filter-lens arrays.

The interleaved-subarray antenna (ISA) is based on a modified version of an existing concept. Subarray overlapping (interleaving) is a method for controlling the sidelobe-level in phased arrays with a small number of phase-shifters and narrow scanning-width. The novelty of the planar design, as proposed in this thesis, is in finding a realization of the overlapped subarrays and the feed network, which does not require vertical fabrication processes such as via-holes and RF-crossovers. This is specially important at millimeter-wave frequencies, where such processes are generally poorly characterized and are difficult to reproduce consistently. The other contribution to this subject is introducing the concept of resonant-feed network, which makes it possible to realize and maintain the required array coefficients in the presence of heavy mutual coupling effects, as is generally encountered in planar array structures. Measurement results for an example ISA show a sidelobe-level of better than -20 dB over a tuning range of ±10°. The number of phase-shifters is reduced by a factor of 2.5 in this design.

MEMS tunable filters, which are described in Chapter 3, represent the state of the art of such components. Several design issues involving tunable filters are addressed and resolved in a systematic approach. The outcome is a miniature-tunable bandpass filter with a continuous tuning range of 14% around 20 GHz and the total length of nearly a quarter of a free-space wavelength at the center-frequency. This filter has a fixed fractional bandwidth, and its mid-band insertion-loss is nearly 4 dB through the tuning range, which is similar to a standard (fixed) filter using the same technology.

Antenna-filter-antenna elements are introduced in Chapter 4, as the integrated building blocks of bandpass frequency-selective surfaces and filter-lens arrays. The FSS structures which are formed based on the AFA elements are structurally much simpler than the standard multi-layer FSS designs, and can realize a rather general category of frequency responses. Rigorous, yet simple, design methods which have been proposed in this chapter, reduce the black magic of the FSS design to a game of filter synthesis, which can be completed in a matter of hours and using a minimal amount of full-wave electromagnetic modeling.

The filter lens-array is a novel multi-function component which can replace the dielectric lens in power combining, focal plane scanning, and millimeter-wave imaging systems. FLA, which is formed as a non-uniform array of AFA elements, can be considered as the combination of a focusing array and a bandpass filter (or FSS). FLA's are simple structures that can be fabricated using any standard thin-film process. For a 3 inch FLA with f/D of 1.25, 11 dB of focusing gain has been measured at 35 GHz. With a 3-dB bandwidth of 8.2%, the combined efficiency of this FLA is $40 - 50\%$. This is similar to a teflon lens and much less than the combination of the lens and bandpass filter. The two-dimensional scanning performance of the FLA has been demonstrated for $\pm 30^\circ$ in the H-plane and $\pm 20^\circ$ in the E-plane.

The developed components may be used in a diverse range of applications. Their major commonality, however, is the technological compatibility which allows their integration together or with other MEMS/microfabricatied components. This leads to some ideas for future developments, as will be discussed in the rest of this chapter.

Interleaved-Subarray Antennas with Integrated MEMS Phase-Shifters - Multi-bit MEMS phase-shifters have been demonstrated successfully at millimeter-wave frequencies [64][7][2][67]. An interesting extension towards an integrated passive front-end is the wafer-scale integration of these components with the interleaved sub-array antennas. As the number of the phase shifters is greatly reduced in this type of phased array, fabrication of such systems is believed to be feasible, even within the limits of commercially available microfabrication technologies. In addition to the obvious benefits of having an integrated phased-array system, if the design of the phase shifters is considered in conjunction with the specific array application, the values the bits (or phase steps) can be decided based on the particular scanning requirements. An array-specific phase-shifter design, will enhance the radiation performance and allow for using a lower number of bits.

Digital Wide-Band MEMS Tunable Filters - In the context of tunable filters, one can hardly imagine ways to enhance the tuning range by using analog MEMS varactors. MEMS switch-capacitors, on the other hand, can result in a considerable tuning range due to their large capacitive ratio. More precisely, if used in series with fixed MAM capacitors, they can provide controlled capacitive ratios ranging from 1.5:1 to 10:1. One possible approach is to use many symmetrical pairs of such combinations to load the resonators of an inductively-coupled filter (see Sec. 3.5.2)[1]. As each switch-capacitor load can have two values of capacitance, using N independently biased loading pairs per resonator results in 2^N states of tuning. Now, with a careful design of the capacitive ratios, each pair can represent a different value in a binary representation of the tuning factor, and a N-bit digital tuning can be obtained. As

---

[1] Since a heavy capacitive loading of the resonators results in the most miniaturization at the first resonance, such a design will not suffer from the close higher order pass-bands, as was the case for the inductively-coupled filters with only one pair of tapped capacitive loads.

the maximum capacitive ratio can be quite large, this technique may be used to obtain digital tunable filters with nearly one octave of tuning range. However, the number of digits and the accuracy of tuning is limited by the number of switch-capacitor pairs (N), which generally cannot exceed 3-5 due to size restrictions[2]. Preliminary studies in an example case show that this technique can be used to design a 4-bit tunable filter in the rage of 12-18 GHz.

Active and Agile AFA-Arrays - Some very interesting research problems can be defined in the context of the AFA arrays and in an attempt to utilize the AFA concept for more complicated functions. One of the possibilities is using negative resistance amplifiers or other types of active devices to introduce gain in the FSS and FLA structures. If amplifiers can be integrated in the AFA array, they can be used as very compact gain stages to replace the bulky grid amplifiers in high-power millimeter-wave applications [87] [82].

Another possibility, is to integrate tuning elements in the CPW layer of an AFA array. For example, using a BST film over parts of the CPW resonators can be considered for obtaining a voltage-controlled phase-delay in Type-III AFA element (see Sec.4.3). If used to create a linear phase distribution across the AFA array, this variable phase-delay can form a simple beam-steering mechanism. Such a concept is useful both for FSS and FLA applications. In the case of FLA, this can be used to achieve a single feed scanning system (vs. using a feed matrix). However, methods for biasing the BST layer have to be addressed in such structures. A similar function may be attainable using MEMS tuning elements, but integrating MEMS devices between the two wafers is not straightforward.

Phased Reflect-Arrays - AFA concepts can also be used in design of reflect-arrays, if simple image-theoretical techniques are used to symmetrically expand the

---

[2] Also an excessive use of the MEMS capacitors increases the insertion-loss of the filter.

reflect array structures. In this sense, an actual reflect-array can be formed based on half of the AFA cells (including one antenna and a modified CPW layer). Focusing reflect-arrays (FRA) can be obtained simply by adjusting the length of the CPW resonator (which can be replaced by a simple stub in this case). The advantage of using a reflective design vs. trasmittive AFA arrays is the easy access to the CPW layer which facilitates integration of active or tunable components. Particularly, MEMS tunable loads can be added to the CPW resonator to create a controllable phase-delay (in the reflected signal). Similar to agile AFA arrays, these phase delays can be used to achieve beam-steering. Such a system can be referred to as a phased reflect-array (PRA) and presents one of the simplest beam-steering solutions.

APPENDICES

APPENDIX A

Design of Resonant Feed Sections

To show the design procedure, we use the (2.16) to design a resonant section that provides an edge voltage ratio of $K = 1.6$ between the two neighboring patches. We assume that the total length of this section is fixed at 2 mm. At 60 GHz and on a 125 μm thick Teflon substrate ($\varepsilon_r = 2.2$) a 100 Ω microstrip line has a width of $W_1 = 100$ μm and $\varepsilon_{r-eff(1)} = 1.72$, and a 50 Ω line has a width of $W_2 = 375$ μm and $\varepsilon_{r-eff(2)} = 1.88$. For the total length of $l = 2$ mm and starting from the values of β_1 and β_2 corresponding to the effective dielectric constants of the 100 Ω and 50 Ω lines respectively, we may solve equations 2.16a-c numerically to obtain the values of Z_1, Z_2, l_1 and l_2. Now using a synthesis program like LineCalc [39], we may obtain the new values of W_2 and $\varepsilon_{r-eff(2)}$ and repeat the procedure until the results converge. Results of this iterative procedure are presented in Table A-1. α_1 and α_2 in this table show the simulated attenuation constants of the line sections at 60 GHz. They may be used to predict the actual voltage ratio in presence of the transmission line losses, which were neglected in the previous derivations. Replacing β_1 with the complex propagation constant $\beta_1 - j\alpha_1$ and β_2 with $\beta_1 - j\alpha_1$ in (2.15), and using the values in the last column of Table A-1, we obtain:

$$V_{j+1} = (1.600 + j0.002)V_j + (0.297 + j0.000)I_j. \tag{A-1}$$

This shows that the designed feed section provides a voltage ratio which is accurate within 2% even when the section is loaded by a terminal impedance of $\geq 10\ \Omega$.

Iteration #	0	1	2	3
Z_1 (Ω)	100	100	100	100
Z_2 (Ω)	50.0	56.6	57.2	57.2
l_1 (mm)	-	1.275	1.264	1.264
l_2 (mm)	-	0.725	0.736	0.736
W_1 (mm)	0.100	0.100	0.100	0.100
W_2 (mm)	0.375	0.308	0.302	0.302
$\varepsilon_{r-eff(1)}$	1.724	1.724	1.724	1.724
$\varepsilon_{r-eff(2)}$	1.883	1.856	1.854	1.854
α_1 (/m)	2.15	2.15	2.15	2.15
α_2 (/m)	1.85	1.88	1.88	1.88

Table A-1: Iterative design of an example resonant section.

APPENDIX B

Modelling of In-Line Components

In-line series capacitors and shunt inductors were extensively used in design of the tunable filters in the Chapter 3. This appendix presents a brief discussion on the modelling of these devices.

B-1 Interdigital Capacitors

Interdigital capacitors are one of the simplest type of in-line components, since they can be fabricated using a single-mask process. With a total width of 100-200 μm, they can easily achieve the capacitances of 10-30 fF with fingers that do not exceed a small fraction of a wavelength at K-band, and therefore present a nearly ideal realization of the lumped series capacitors. Fig B-1 shows two series interdigital capacitors in symmetrical and asymmetrical configurations, and their circuit models. Although these circuit models are defined for a zero-length section (notice that the reference planes coincide), the series transmission-line lengths generally must be included to account for the parasitic shunt capacitors, formed between the fingers and the CPW ground. In general, a resistor R can be used in parallel to C to model the losses. In most practical cases, however, the loss is negligible and the parallel resistor proves unnecessary.

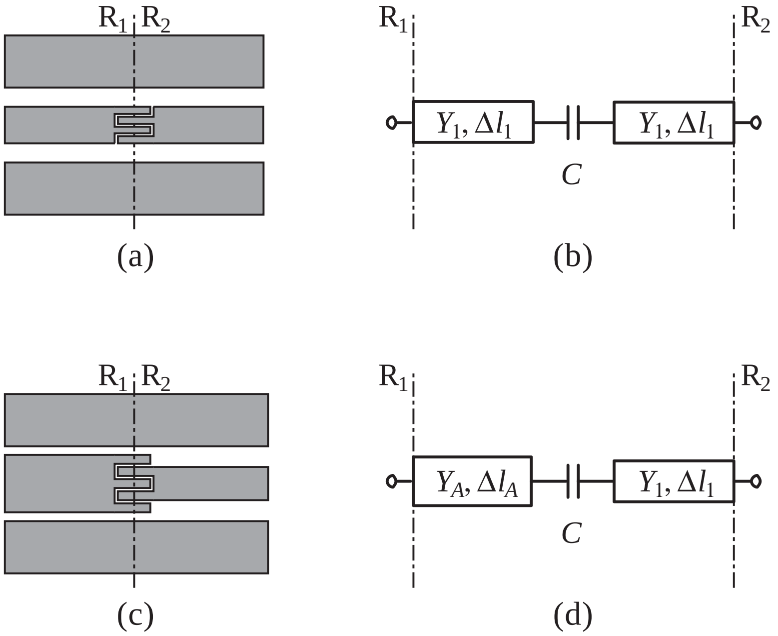

(a) (b)

(c) (d)

Figure B-1: Interdigital capacitors as series components: a,b) symmetrical capacitor in a CPW line and its circuit model, and c,d) asymmetrical capacitor and its circuit model.

Interdigital capacitors can be accurately modelled using 2.5D moment-method simulators such as Momentum [39]. The model parameters are determined by matching the amplitude and phase of the simulated/measured S-parameters of the two-port structure and that of the circuit model. To assess the accuracy of the moment-method simulations, several test structures were fabricated and measured. It was observed that the moment-method simulations can predict the value of C within 5% of the actual value. The simulation results are less accurate when it comes to the transmission line lengths (Δl_x).

B-2 Metal-Air-Metal Capacitors

Series MAM capacitors are used when larger values of series capacitance (in the range of 50-150 fF) are required. In the case of bandpass filters, they are especially useful as the input/output coupling capacitors, were they generally assume an asymmetrical geometry. The layout and circuit model of a generic series MAM capacitor is shown in Fig. B-2. A parallel-plate capacitor is created by extending the center conductor of one CPW line into a bridge-like structure which suspends over the center conductor of a second piece of CPW line. In spite of the structural differences, the circuit model is identical for the asymmetrical MAM and interdigital capacitors. The model parameters can be obtained using a similar approach, but the moment-method simulations are much less accurate in the case of MAM capacitors, for at least two reasons: 1) the numerical errors in modelling the bridge anchors, and 2) bowing of the MEMS bridge in the actual capacitors.

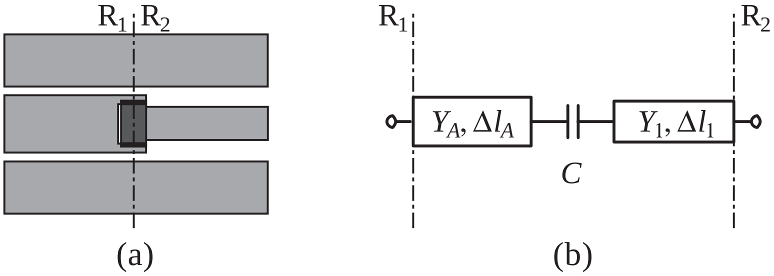

Figure B-2: A series MAM capacitor: a) layout, b) circuit model.

B-3 Shunt Inductors

An interesting component, which is especially appropriate for CPW designs, is a shunt inductor. Shunt inductors are created by connecting the center conductor and the ground plane of the CPW line using high impedance (narrow) lines [68], as shown in Fig. B-3. For the inductor values of greater than 20-30 pH, it is generally necessary to extend the high impedance lines inside the CPW ground plane (see Fig. B-3a), forming shunt short-ended CPW stubs . In the asymmetrical configuration, which is generally encountered at the input/output inverters of the inductively-coupled CPW filters (see Chapter 3), these CPW stubs can support slot-line mode and cause radiation and other anomalies in the circuit. To avoid such problems, these modes must be grounded by connecting the two halves of the CPW ground at the stub input, as shown in Fig. B-3c. Therefore, the asymmetrical design contains bridges and requires a multi-mask fabrication process. Similar to the case of series capacitors, losses can be taken into account by adding a series resistance to the inductor in the circuit model (or by using an inductor with finite Q).

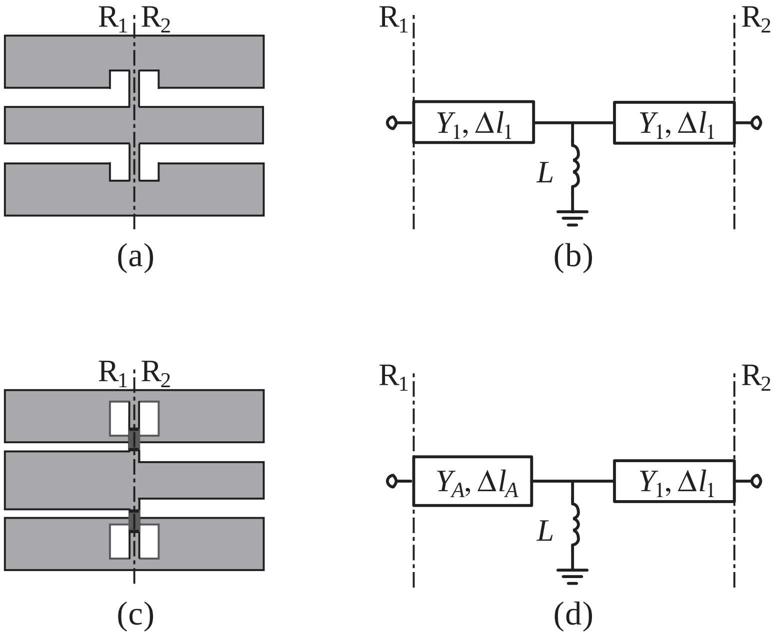

Figure B-3: Shunt inductors and their circuit model: a,b) symmetrical configuration, and c,d) asymmetrical configuration.

The commercial moment-method simulators are not very successful in modelling the shunt inductors. Table B-1 presents the simulated and measured inductor values for example symmetrical and asymmetrical test structures. Simulations are based on Momentum [39] and Sonnet [63] softwares, and in all cases predict values that are $10 - 30\%$ higher than actual. The source of the discrepancy is not clear.

	L(pH)		
	Momentum [39]	Sonnet [63]	Measurement
Symmetrical	41	37	32
Asymmetrical	157	154	138

Table B-1: Simulated and measured inductance for two test structures.

APPENDIX C

MEMS Switched-Band Filters

MEMS switched-band filters in general follow the same principle of operation as tunable filters. The MEMS varactors, however, are replaced by switchable components. MEMS switch-capacitors are the key elements in designing these components and switched-band filters, as will be shown in the following examples. The designs presented in this appendix are based on the boxed microstrip lines on a 250 μm-thick quartz substrate ($\varepsilon_r = 3.8$, $\tan\delta = 0.0001$).

C-1 Switched-Band Filter With Shunt Capacitive Loading

A capacitively-coupled microstrip filter can be designed similar to the example in Sec. 3.5.1. The basic difference is that the shunt varactor loads are replaced by a series combination of the MEMS switch-capacitors and open-ended radial stubs (acting as fixed capacitors). A possible switchable load structure is shown in Fig. C-1, along with its complete circuit model. Z_1 represents the characteristic impedance of the microstrip line, C represents the capacitance of the MEMS bridge that can assume two values of C_{up} or C_{down} (in the up and down states), and C_s is the equivalent capacitance of the open-ended stub. L, R, and R_s are generally needed to account for the bridge inductance, bridge resistance, and the radiation losses of the stub, respectively, but they can be neglected in the design stage[1].

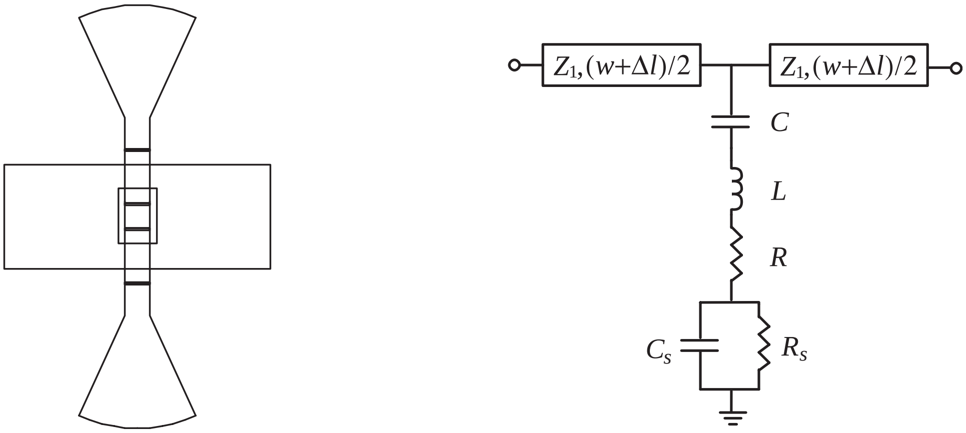

(a) (b)

Figure C-1: A MEMS switch-capacitor in shunt configuration: a) layout, and b) circuit model.

The physical layout of a capacitively coupled filter based on the microstrip resonators and the described type of loading is shown in Fig. C-2. The circuit model is as shown in Fig. 3.7, with B_p interpreted as the equivalent shunt susceptance of the loads, as calculated from model of Fig. C-1b (in the simplified version $B_p = \omega C_p = \omega(C \| C_s)$). The model parameters for a 6% filter at 35 GHz are given in Table C-1, where the Chebyshev coefficients of Table 3.1 have been used. Assuming $C_{down} \gg C_s$, the filter is designed based on the average value of $C_p = 86$ fF ($C_p = \frac{1}{2}(C_s \| C_{up} + C_s)$; $C_{up} = 184$ fF, $C_s = 105$ fF), so that the pass-bands are symmetrically located around 35 GHz for the two modes of operation. Notice that the required values of the coupling capacitors are so that they can be realized using interdigital or simple gap capacitors.

Figure C-3 shows the simulated S-parameters the switched-band filter for $C =$ 184 fF and 1 pF, corresponding to the up and down states of the MEMS switch-

---

[1] In the symmetrical configuration as shown in the Fig. C-1a and for the boxed structure, the radiation loss is generally negligible and R_s can be omitted from model.

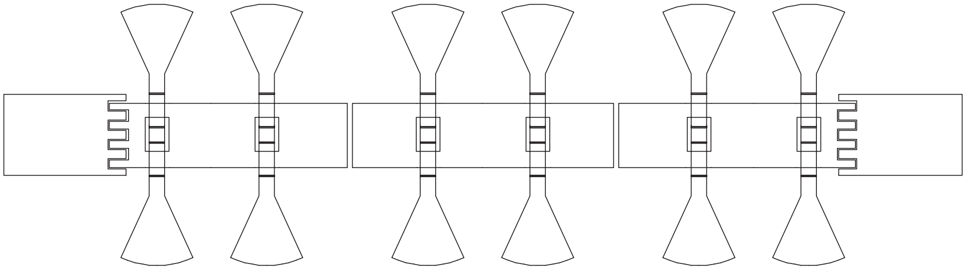

Figure C-2: Layout of the 3-pole switched-band filter using shunt MEMS switch-capacitors.

$Z_A(\Omega)$	50	$C_{0,1} = C_{3,4}$ (fF)	42
$Z_1(\Omega)$	60	$C_{1,2} = C_{2,3}$ (fF)	12
C_p (fF)	86	$\Phi_{0,1} = \Phi_{3,4}$ (deg.)	-25.4
θ_1 (deg.)	45.7	$\Phi_{1,2} = \Phi_{2,3}$ (deg.)	-8.8
θ_2 (deg.)	50.0	Φ_A (deg.)	-20.1

Table C-1: Model parameters for the capacitively-loaded switched-band filter at 35 GHz.

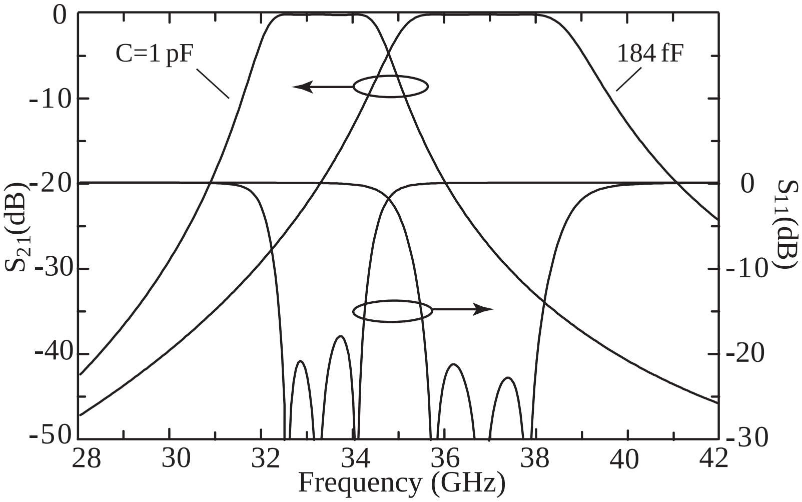

Figure C-3: Simulated S-parameters of the bandpass filter with shunt MEMS switch-capacitors.

capacitor. The actual value of C_{down} is a function of the dielectric constant and thickness of the isolator layer, as well as the area of contact, but as far as it is much greater than C_s, has no impact on the down-state response. Similar to the case of the capacitively-coupled tunable filter (see Sec. 3.5.1), fractional bandwidth decreases considerably when the filter is switched to the lower-band (from 9.3% to 6.8%). Full-wave simulations based on [39] predict similar results, with an insertion loss of better than 1 dB for both upper- and lower-band modes of operation.

C-2 Switched-Band Filter With Series Inductive Loading

In chapter 3, we mentioned that the bandwidth variations due to tuning can be minimized if alternative loading and coupling schemes are used. In Sec.3.5.2, fixed bandwidth was achieved by using inductive inverters and capacitively-loaded resonators. In the microstrip designs, shunt inductors cannot be realized, due to the lack of access to ground. But a similar solution may be sought by using the dual topology, which uses capacitive inverters and inductively-loaded resonators. A realization of the switchable inductive loading is shown in Fig. C-4. The proposed structure, which we simply refer to as the MEMS switch-inductor, is composed of the a series inductive loop, in parallel with a capacitive MEMS switch. When the MEMS switch is in the up-state, C is small ($= C_{up}$) and the inductor is in the signal path. In the down state, C is large ($= C_{down}$), and the inductor is effectively bypassed.

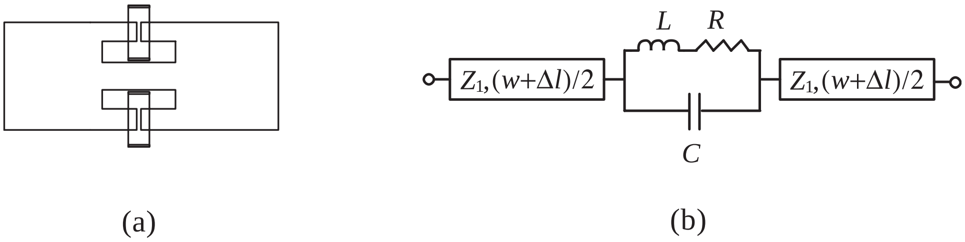

Figure C-4: A MEMS switch-inductor in series configuration: a) layout, and b) circuit model.

Figure C-5 presets the layout and circuit model of a 3-pole filter based on the capacitive coupling of the microstrip resonators with series MEMS switch-inductor loads. The series resistor in the model of the switch-inductor has been eliminated for simplicity. Assuming that in the down state the switches perfectly bypass the series inductors, the filter is designed for the upper band of operation by neglecting the inductive loads. The locations and values of the inductors are then determined so that the filter operates at the lower pass-band with the desired bandwidth, when the MEMS bridges are up. If a fixed absolute bandwidth is sought, this generally dictates different loading locations and inductor values for different resonators (resonators (1) and (3) are identical, but resonator (2) is different). The model parameters that are calculated based on this procedure are given in Table C-2. These values are for filter with the coefficients of Table 3.1, with a 6% bandwidth at 36.4 GHz, which is the center of the upper pass-band.

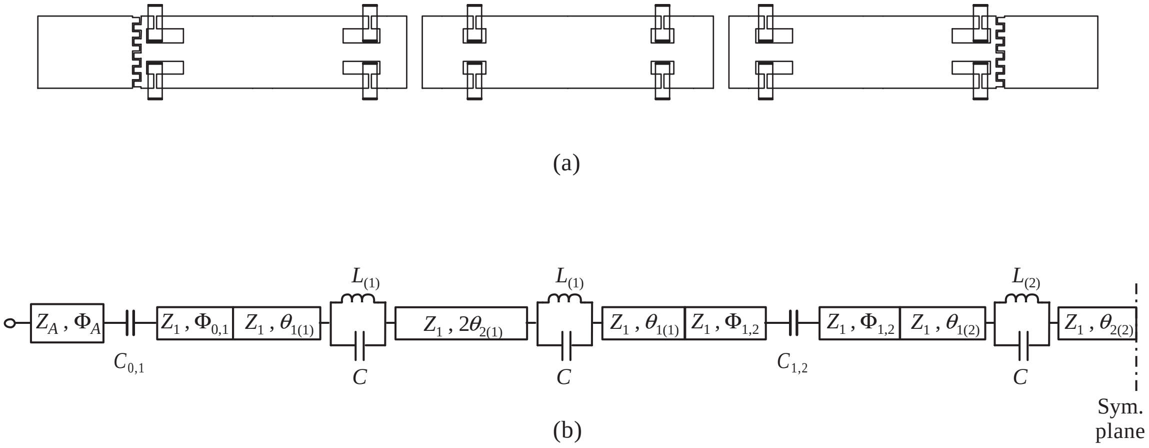

Figure C-5: 3-pole switched-band filter using series MEMS switch-inductors: a) layout, and b) circuit model.

The S-parameters of the inductively-loaded switchable filter in the upper and lower bands can be simulated using the circuit model of Fig. C-5, and $C = 1$ pF and 65 fF, respectively. In the upper band, the filter has a 2.6 GHz bandwidth centered at 37 GHz. In the lower-band, the pass-band is 2.8 GHz wide and centered at 33.4 GHz.

$Z_A(\Omega)$	50	$\theta_{2(1)}$ (deg.)	60
$Z_1(\Omega)$	50	$\theta_{2(2)}$ (deg.)	52
$L_{(1)}$ (pH)	86	$C_{0,1} = C_{3,4}$ (fF)	32
$L_{(2)}$ (pH)	58	$C_{1,2} = C_{2,3}$ (fF)	8.4
C_{up} (fF)	65	$\Phi_{0,1} = \Phi_{3,4}$ (deg.)	-18.1
$\theta_{1(1)}$ (deg.)	30	$\Phi_{1,2} = \Phi_{2,3}$ (deg.)	-5.4
$\theta_{1(2)}$ (deg.)	38	Φ_A (deg.)	-18.1

Table C-2: Model parameters for the inductively-loaded switched-band filter at 36.4 GHz.

The absolute bandwidth, which was expected to be constant, varies some 8% due to the fact that the design method neglects the effect of loading in the upper-band. However, this design presents a much better controlled bandwidth, as compared to the capacitively-loaded switchable filter.

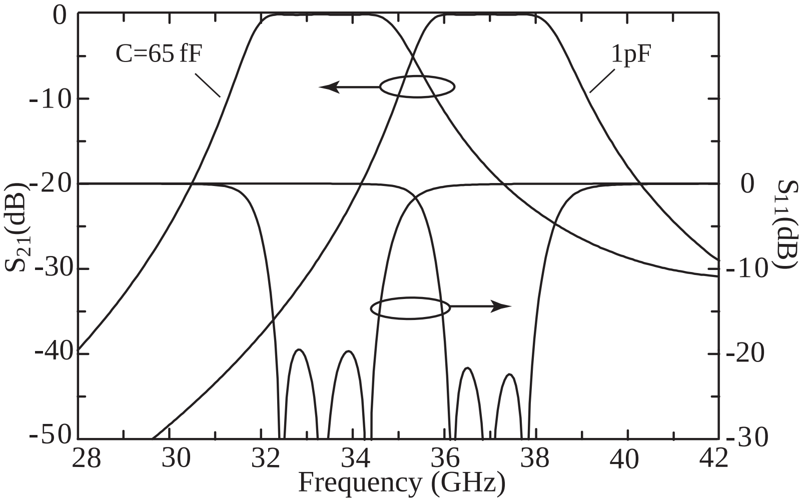

Figure C-6: Simulated S-parameters of the bandpass filter with series MEMS switch-inductors.

APPENDIX D

FLA Operation With Cosine-Type Feed Patterns

Most practical feed antennas have a broadside pattern which can be approximated with a $\cos^n$ function, as following:

$$D_f(\vartheta,\varphi) = \begin{cases} 2(n+1)\cos^n\vartheta & ,\vartheta \leq \ \pi/2 \\ 0 & ,\text{elsewhere} \end{cases} \tag{D-1}$$

Assuming lossless conditions, (D-1) also represents the gain of the feed antenna. If such a feed antenna is used to illuminate an FLA with the subtended angle ϑ_{sub}, the average gain and extrinsic spill-over efficiency can be obtained using (5.25) and (5.27), resulting:

$$\langle G_f \rangle = 2\,\frac{1-\cos^{n+1}\vartheta_{sub}}{1-\cos\vartheta_{sub}}\eta'_{SO} = 1-\cos^{n+1}\vartheta_{sub} \tag{D-2}$$

The calculated values of $G_f(0,0)$ and $\langle G_f \rangle$ are shown in Fig. D-1 for n between 0 and 60. It is observed that $\langle G_f \rangle$ approaches optimal feed gain of G_{f0}, when n becomes large. The gain of the FLA under such an illumination can be calculated from (5.24). For the FLA reported in Sec. 5.7, the measured value of focusing gain is $G_{FLA} = 25.6 - 14.7 = 10.9$ dB. An upper-bound estimation of the FLA gain can be obtained by replacing $\eta_T = 1$, as shown in Fig. D-1 (dashed line). A better estimation of the FLA gain, however, is obtained from the analysis method of Sec. 5.5 (marked line in Fig. D-1).

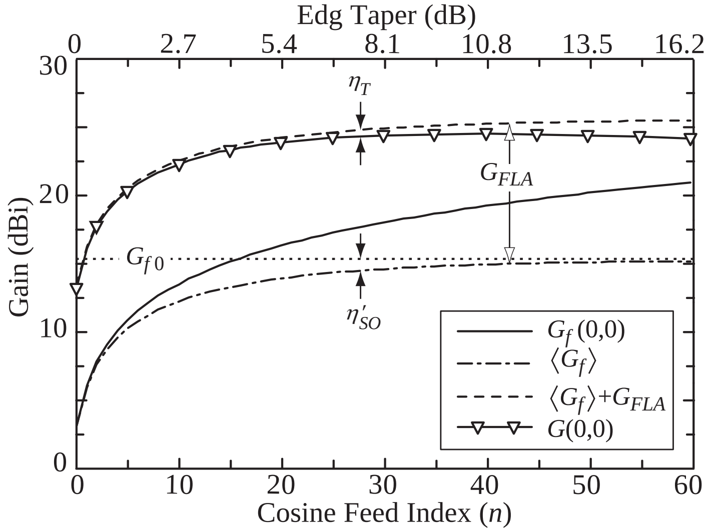

Figure D-1: Calculated gain values vs. n.

Some other interesting information are also contained in Fig. D-1. For example, the upper horizontal axis indicates the normalized value of FLA edge illumination for the given value of n (referred to as the *edge-taper*). Also, according to (5.26) and since $\eta_f = 1$ for the lossless feed, η'_{SO} is equal to the difference between the G_{f0} and $\langle G_f \rangle$ (all in dB). Similarly, the difference between the upper-bound estimated gain and the actual simulated values of $G(0,0)$ represents η_T. The overall spill-over efficiency (η_{SO}) can be calculated using (5.17) and from the complete FLA analysis. The values of η'_{SO}, η_{SO}, and η_T are plotted vs. n in Fig. D-2. It is observed that for the cosine-type feed patterns, $\eta_{SO} \cong \eta'_{SO}$. The spill-over efficiency is dominant for $n \leq 34$, while the η_T is dominant for larger values of n.

The maximum FLA gain in Fig. D-1 is 24.4 dBi, which is achieved for $n = 38$. This is only 0.4 dB less than the simulated gain under optimal illumination condition. However, the gain of the feed antenna is 18.9 dB in this case, which results in a focusing gain of only 24.4.18.9 = 5.5 dB. This is considerably lower than the optimal value of 10.9 dB, and shows that using an actual feed pattern can considerably reduce

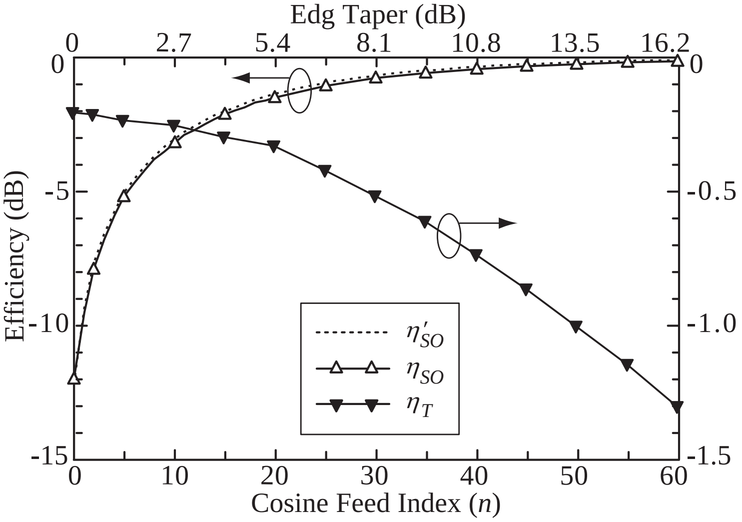

Figure D-2: Different efficiency factors vs. n.

the effectiveness of the FLA's with small aperture size and large f/D.

APPENDIX E

Gaussian Optics Characterization of FLA

In Sec. 5.6 we discussed measurement methods that can be used to characterize FLA. Especially, we described a method to extract the focusing gain of the FLA based on pattern measurements. Alternatively, FLA can be characterized as a thin lens and in terms of Gaussian optics [86].

Fig. E-1 shows FLA in a Gaussian optics measurement system. An input axial beam of the waist radius w_{01} is generated using a transmit horn antenna. The waist of the input beam is located near the phase-center of the horn and at a distance z_1 from the center of the FLA. The output is a Gaussian beam with the waist of radius w_{02} at a distance z_2 from the center of FLA. An open-ended waveguide antenna is used to probe the output radiation intensity along this axis.

This system has been used to measure the FLA described in Sec. 5.7. The transmit horn in this case is placed at a distance $z_1 \cong 120$ cm from the FLA. The normalized measured output radiation intensity along the z axis is shown in Fig. E-2. The fitted curve shows the intensity of an ideal Gaussian beam, which is given by [86]:

$$I(z) = \frac{1}{1 + (z - z_2)^2 / z_{02}^2} \tag{E-1}$$

where z_2 is the location of the beam waist and z_{02} is half of the depth of focus. The best fit between (E-1) and the measurement is obtained for $z_2 = 10.6$ cm and

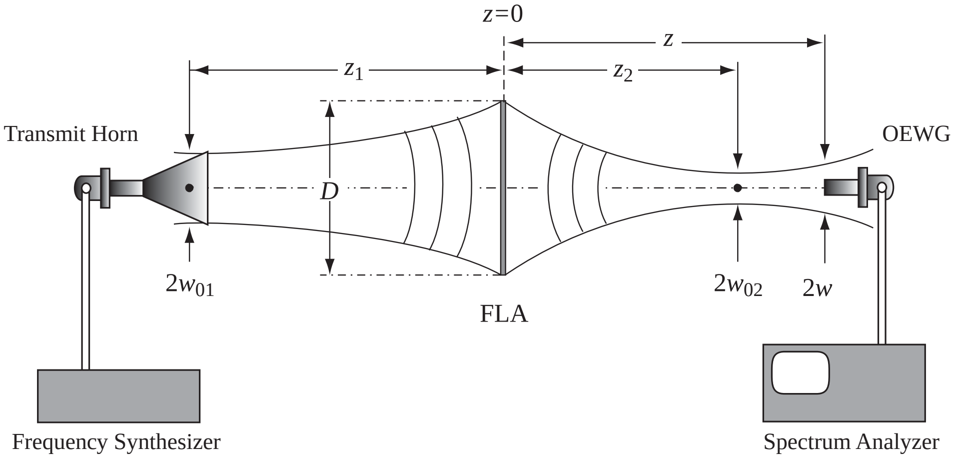

Figure E-1: FLA in a Gaussian optics measurement system.

$z_{02} = 2.15$ cm. The beam waist at the output can be calculated from:

$$w_{02} = \sqrt{\frac{z_{02}\lambda_0}{\pi}} \tag{E-2}$$

where λ_0 is the wavelength at the operation frequency (here 8.57 mm). This results in a waist radius of $w_{02} = 7.7$ mm for the output beam.

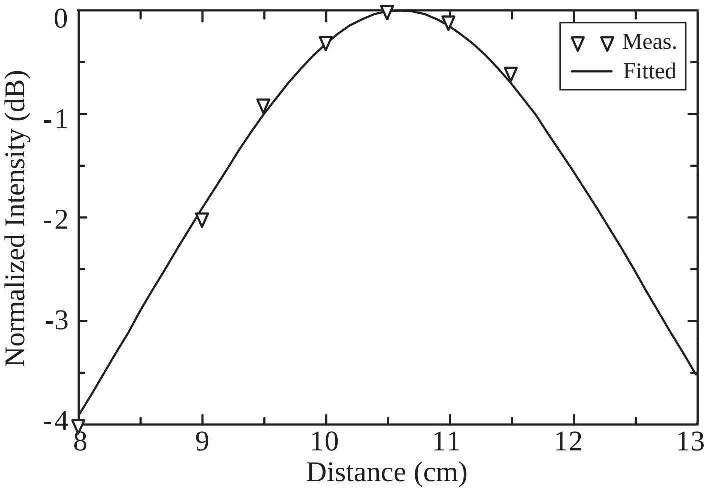

Figure E-2: Measured values of the output radiation intensity along the FLA axis.

Once the output beam is characterized experimentally, it can be used to extract more information about the FLA. The basic lens equation is written as [86]:

$$\frac{1}{f} = \frac{1}{R_1} + \frac{1}{R_2} \tag{E-3}$$

where f is the focal distance and R_1 and R_2 are the radii of the curvature of the input and output beams at $z = 0$. (E-3) can be used to determine the focal distance of the lens. These radii can be calculated from:

$$R_i = z_i \left[1 + (z_{0i}/z_i)^2\right] \qquad ; \quad i = 1, 2. \tag{E-4}$$

If the transmit horn is far enough so that $_1 >> z_{01}$, as it was the case in our experiment, $R_1 \cong z_1$ (in this case $\cong$ 120 cm). With $i = 2$, (E-4) results in $R_2 = 11.0$ cm. For these values of R_1 and R_2 (E-3) gives $f = 10.1$ cm which is very close to the design value of 10 cm.

If the lens is illuminated by plane wave (or a gaussian beam centered at $z = 0$), $R_1 = \infty$ and (E-3) predicts that $R_2 = f = 10.1$ cm. Assuming that the output beam has a waist radius of $w_2' = D/2$ at $z = 0$, its waist radius and location can be calculated from:

$$\begin{aligned} w_{02}' &= w_2 \cdot \left[1 + \left(\tfrac{\pi {w_2'}^2}{\lambda_0 f}\right)^2\right]^{-\frac{1}{2}} \\ z_{02}' &= \frac{\pi^2 w_2'^2 {w_{02}'}^2}{\lambda_0^2 f}. \end{aligned} \tag{E-5}$$

For $D = 7.8$ cm this results in $w_{02}' = 7.0$ mm and $z_{02}' = 9.8$ cm. Since the amount of focusing can be measured by the ratio of the input and output beam waist areas, after including the spill-over and structural FLA losses, the focusing gain of FLA can be calculated as:

$$G_{FLA}^{opt} = \eta_{SO} \cdot T_{FLA}(\omega_0) \cdot \frac{\pi {w_2'}^2}{\pi {w_{02}'}^2}. \tag{E-6}$$

The overall loss due to spill-over and FLA were found as 3.5 dB in Sec. 5.7 (see Table 5.2). (E-6) then results in a focusing gain of focusing gain of 10.5 dB, which is very close to what obtained from direct gain measurements (10.9 dB).

BIBLIOGRAPHY

BIBLIOGRAPHY

[1] J. S. Hayden G. M. Rebeiz, G. L. Tan, “RF MEMS phase shifters: design and applications,” *IEEE Microwave Magazine*, vol. 3, pp. 72–81, June 2002.

[2] J. S. Hayden, A. Malczewski, J. Kleber, C. L. Goldsmith, and G. M. Rebeiz, “2 and 4-bit dc to 18GHz microstrip MEMS distributed phase shifters,” in *2001 IEEE MTT-S Int. Microwave Symp. Dig.*, Phoenix, AZ, June 2001, pp. 219–222.

[3] G. L. Tan, R. E. Mihailovich, J. B. Hacker, J. F. DeNatale, and G. M. Rebeiz, “Low-loss 2- and 4-bit ttd MEMS phase shifters based on SP4T switches,” *IEEE Trans. Microwave Theory Tech.*, vol. 51, pp. 297–304, Jan. 2003.

[4] H. Nayashi, T. Nakagawa, and K. Araki, “A miniaturized MMIC analog phase shifter using two quarter-wave-length transmission lines,” *IEEE Trans. Microwave Theory Tech.*, vol. 50, pp. 150–154, Jan. 2002.

[5] W. Rotman and R. Turner, “Wide-angle microwave lens for line source applications,” *IEEE Trans. Antennas and Propagation*, vol. 11, pp. 623–632, Nov. 1963.

[6] G. M. Rebeiz and J. B. Muldavin, “RF MEMS switches and switch circuits,” *IEEE Microwave Magazine*, vol. 2, pp. 59–71, Dec. 2001.

[7] J. Rizk, G. L. Tan, J. B. Muldavin, and G. M. Rbeiz, “High-isolation W-band MEMS switches,” *IEEE Microwave and Wireless Components Letters*, vol. 11, pp. 10–12, Jan. 2001.

[8] S. Hollung, A. E. Cox, and Z. B. Popovic, “A bi-directional quasi-optical lens amplifier,” *IEEE Trans. Microwave Theory Tech.*, vol. 45, pp. 2352–2357, Dec. 1997.

[9] W. Menzel, D. Pilz, and M. Al-Tikriti, “Millimeter-wave folded reflector antennas with high gain, low loss, and low profile,” *IEEE Antennas and Propagation Magazine*, vol. 44, pp. 24–29, June 2002.

[10] D. Popovic and Z. Popovic, “Multibeam antennas with polarization and angle diversity,” *IEEE Trans. Antennas and Propagation*, vol. 50, pp. 651–657, May 2002.

[11] E. Fotheringham, S. Romisch, P. C. Smith, D. Popovic, and Z. Popovic, "A lens antenna array with adaptive optical processing," *IEEE Trans. Antennas and Propagation*, vol. 50, pp. 607–617, May 2002.

[12] B. Schoenlinner, Xidong Wu, J. P. Ebling, G. V. Eleftheriades, and G. M. Rebeiz, "Wide-scan spherical-lens antennas for automotive radars," *IEEE Trans. Microwave Theroy Tech.*, vol. 50, pp. 2166 –2175, Sept. 2002.

[13] S. Romisch, D. Popovic, N. Shino, R. Lee, and Z. Popovic, "Multi-beam discrete lens arrays with amplitude-controlled steering," in *2003 IEEE MTT-S Int. Microwave Symp. Dig.*, Philadelphia, PA, June 2003, pp. 1669–1672.

[14] K. Lim, S. Pinel, M. Davis, A. Stono, C.-H. Lee, D. Hoe, A. Obatoynbo, J. Laskar, E. M. Tantzeris, and R. Tummala, "RF-system-on-package (SOP) for wireless communications," *IEEE Microwave Magazine*, vol. 3, pp. 88–99, March 2002.

[15] M. F. Davis, S.-W. Yoon, S. Mandal, N. Bushyager, M. Maeng, K. Lim, S. Pinel, A. Sutaono, J. Lskar, M. Tentzeris, T. Nonaka, V. Sundaram, F. Liu, and R. Tummala, "RF-microwave multi-band design solutions for multilayer organic system on package integrated passives," in *2002 IEEE MTT-S Int. Microwave Symp. Dig.*, Seattle, WA, June 2002, pp. 2217–2220.

[16] S. Chakraborty, K. Lim, A. Sutono, E. Chen, S. Yoo, A. Obatoyinbo, S.-W. Yoon, M. Maeng, M. F. Davis, S. Pinel, and J. Lskar, "A 2.4-GHz radio front end in RF system-on-package technology," *IEEE Microwave Magazine*, vol. 3, pp. 94–104, June 2002.

[17] W. Diels, K. Vaesen, P. Wambacq, S. Donnay, W. De Raedt, M. Engels, and I. Bolsens, "Single-package integration of RF blocks for a 5 GHz WLAN application," *IEEE Trans. Advanced Packaging*, vol. 24, pp. 384–391, Aug. 2001.

[18] J. Ryckaert, "Multilayer thin film technology as an enabling technology RF system-in-a-package integration," in *2003 IEEE MTT-S Int. Microwave Symp.*, Philadelphia, PA, June 2003, workshop notes.

[19] C. Block, "Transition from discrete components to highly-integrated RF-solution for mobile phone and WLAN," in *2003 IEEE MTT-S Int. Microwave Symp.*, Philadelphia, PA, June 2003, workshop notes.

[20] R. Singh, M. Fakhruddin, and K. F. Poole, "The impact of single-wafer processing on semiconductor manufacturing," *IEEE Trans. Semiconductor Manufacturing*, vol. 16, pp. 96–101, May 2003.

[21] S. Pinel, S. Chakraborty, M. Roelling, R. Kunze, S. Mandal, H. Liang, C.-H. Lee, R. Li, K. Lim, G. White, M. Tentzeris, and J. Lskar, "3D integrated LTCC module using μBGA technology for compact C-band RF front-end module," in *2002 IEEE MTT-S Int. Microwave Symp. Dig.*, Seattle, WA, June 2002, pp. 1553–1556.

[22] K. Itoh, "2GHz band LTCC module for the W-CDMA terminal," in *2003 IEEE MTT-S Int. Microwave Symp.*, Philadelphia, PA, June 2003, workshop notes.

[23] M. Tentzeris, N. Bushyager, J. Lskar, G. Zheng, and J. Papapolymerou, "Analysis and design of MEMS and embedded components in silicon/LTCC packages using FDTD/MRTD for system-on-package applications," in *2003 IEEE Topical Meeting on Silicon Monolithic Integrated Circuits in RF Systems Dig.*, April 2003, pp. 138–141.

[24] G. M. Rebeiz, *RF MEMS Theory, Design, and Technology*, John Wiley and Sons, Hoboken, NJ, 2002.

[25] T. Le Nadan, J. P. Coupez, S. Toutain, and C. Person, "Optimization and miniaturization of a filter/antenna multi-function module using a composite ceramic-foam substrate," in *1999 IEEE MTT-S Int. Microwave Symp. Dig.*, June 1999, pp. 219–222.

[26] A. Abbaspour-Tamijani, Jad Rizk, and G. M. Rebeiz, "Integration of filters and microstrip antennas," in *2002 IEEE AP-S Int. Symp. Dig.*, San Antonio, TX, June 2002, pp. 874–877.

[27] D. Peroulis, S. Pacheco, K. Sarabandi, and L. Katehi, "Tunable lumped components with applications in reconfigurable MEMS filters," in *2001 IEEE MTT-S Int. Microwave Symp. Dig.*, Phoenix, AZ, June 2001, pp. 341–344.

[28] Y. Liu, A. Borgioli, A. S. Nagra, and R. A. York, "Distributed MEMS transmission lines for tunable filter applications," *Int. J. RF Microwave CAE*, vol. 11, pp. 254–260, Aug. 2001.

[29] E. Fourn, A. Pothier, C. Champeaux, P. Tristant, A. Catherinot, E. Rius C. Person P. Blondy, G. Tanne, and F. Huret, "MEMS switcable interdigital coplanar filter," *IEEE Trans. Microwave Theory Tech.*, vol. 51, pp. 320–324, Jan. 2003.

[30] R. J. Mailloux and P. R. Franchi, "Phased array antenna with array elements coupled to form a multiplicity of overlapped subarrays," *US patent No. 3938160, Int. C1 H 01 Q 3/26*, 1976.

[31] J. T. Nemit, "Network approach for reducing the number of phase shifters in a limited scan phased array," *US Patent No.3803625, Int. C1. H 01 Q 3/26,*, 1974.

[32] R. J. Mailloux, L. Zahn, A. Martinez, and G. Forbes, "Grating lobe control in limited scan arrays," *IEEE Trans. Antennas and Propagation.*, vol. 27, pp. 79–85, Jan. 1979.

[33] S. P. Skobelev, "Methods of controlling optimum phased-array antennas for limited field of view," *IEEE Trans. Antennas and Propagation*, vol. 40, pp. 39–49, April 1998.

[34] R. J. Mailloux, "A low sidelobe partially-overlapped constrained feed network for time delayed subarrays," *IEEE Trans. Antennas and Propagation*, vol. 49, pp. 280–291, Feb. 2001.

[35] N. Fourikis, *Phased Array-Based Systems and Applications*, John Wiley and Sons, New York, NY, 1997.

[36] R. L. Fante, "Sysytem study of overlapped subarrayed scanning antennas," *IEEE Trans. Antennas and Propagation*, vol. 28, pp. 668–679, Sept. 1980.

[37] R. S. Elliott, *Antenna Theory and Design, Revised Edition*, John Wiley and Sons, Hoboken, NJ, 2003.

[38] *IE3D 7.0*, Zeland Software Inc., TX, USA.

[39] *Advanced Design System 2002*, Agilent Technologies, Santa Clara, CA, USA.

[40] A. F. Sheta, K. Hettak, J. P. Coupez, C. Person, and S. Toutain, "A new semi-lumped microwave filter structure," in *1995 IEEE MTT-S Int. Microwave Symp. Dig.*, June 1995, pp. 383–386.

[41] G. L. Hey-Shipton, "Quasi-lumped element bandpass filters using dc isolated shunt inductors," in *1996 IEEE MTT-S Int. Microwave Symp. Dig.*, San Francisco, CA, June 1996, pp. 1493–1496.

[42] E. Cristal and S. Frankel, "Hairpin-line and hybrid haipin-line/half-wave parallel-coupled-line filters," *IEEE Trans. Microwave Theory Tech.*, vol. 20, pp. 719–728, Nov. 1972.

[43] J. S Hong, M. J. Lancaster, D. Jedamzik, and R. B. Greed, "8-pole superconducting quasi-elliptic filter for mobile communications application," in *1998 IEEE MTT-S Int. Microwave Symp. Dig.*, June 1998, pp. 367–370.

[44] C. K. Ong, L. Chen, J. Lu, C. Y. Tan, and B. T. G. Tan, "High-temperature superconducting bandpass spiral filter," *IEEE Microwave and Guided Wave Letters*, vol. 47, pp. 407–409, Sept. 1999.

[45] J. J. Yu, S. T. Chew, M. S. Leong, and B. L. Ooi, "New class of microstrip miniaturized filter using triangular stub," *Electronic Letters.*, vol. 37, pp. 1169–1170, Sept. 2001.

[46] J. A. Curtis and S. J. Fiedziusko, "Miniature dual mode microstrip filters," in *1991 IEEE MTT-S Int. Microwave Symp. Dig.*, June 1991, pp. 443–446.

[47] J. S. Hong and M. J. Lancaster, "Microstrip bandpass filter using degenerate modes of a novel meander loop resonator," *IEEE Microwave and Guided Wave Letters*, vol. 5, pp. 371–372, Nov. 1995.

[48] H. Yabuki, M. Sagawa, M. Matsu, and M. Makimoto, "Stripline dual-mode ring resonators and their application to microwave devices," *IEEE Trans. Microwave Theory Tech.*, vol. 44, pp. 723–729, May 1996.

[49] Z. M. Hejazi, P. S. Excell, and Z. Jiang, "Compact dual-mode filters for hts satellite communication systems," *IEEE Microwave and Guided Wave Letters*, vol. 8, pp. 275–277, Aug. 1998.

[50] G. L. Matthaei, N. O. Fenzi, R. J. Forse, and S. M. Rohlfing, "Hairpin-comb filters for hts and other narrow-band applications," *IEEE Trans. Microwave Theory Tech.*, vol. 45, pp. 1226–1231, Aug. 1997.

[51] W. J. Chappell, M. P. Little, and L. P. B. Katehi, "High isolation, planar filters using ebg substrates," *IEEE Microwave and Wireless Components Letters*, vol. 11, pp. 246–248, June 2001.

[52] X. Gong, W. J. Chappell, and L. P. B. Katehi, "Capacitive defect ebg resonators," in *2002 IEEE MTT-S Int. Microwave Symp. Dig.*, Seattle, WA, June 2002, pp. 1091–1094.

[53] A. Abbaspour-Tamijani, L. Dussopt, and G. M. Rebeiz, "A milllimeter-wave tunable filter using MEMS varactors," in *2002 European Microwave Conference Dig.*, Milan, Italy, Sept. 2002, pp. 813–815.

[54] I. C. Hunter and J. D. Rhodes, "Electronically tunable microwave bandpass filters," *IEEE Trans. Microwave Theory Tech.*, vol. 30, pp. 1354–1360, Sept. 1982.

[55] S. R. Chandler, I. C. Hunter, and J. C. Gardiner, "Active varactor tunable bandpass filter," *IEEE Microwave and Guided Wave Letters*, vol. 3, pp. 70–71, March 1993.

[56] A. R. Brown and G. M. Rebeiz, "A varactor-tuned RF filter," *IEEE Trans. Microwave Theory Tech.*, vol. 48, pp. 1157–1160, July 2000.

[57] J. B. Muldavin and G. M. Rebeiz, "High isolation MEMS shunt switches; part 1: Modeling," *IEEE Trans. Microwave Theory Tech.*, vol. 48, pp. 1054–1052, May 2000.

[58] N. S. Barker and G. M. Rebeiz, "Distributed MEMS true-time delay phase shifters and wide-band switches," *IEEE Trans. Microwave Theory Tech.*, vol. 46, pp. 1881–1890, Nov. 1998.

[59] R. E. Collin, *Fundations For Microwave Engineering, 2nd Edition*, McGraw-Hill, New York, NY, 1992.

[60] G. L. Matthaei, L. Young, and E. M. T. Jones, *Microwave Filters: Impedance-Matching Networks, and Coupling Structures.*

[61] J. G. Hong and M. J. Lancaster, *Microstrip Filters for Rf/Microwave Applications*, John Wiley and Sons, Hoboken, NJ, 2001.

[62] K. C. Gupta, Ramesh Garg, Inder Bahl, and Prakash Bhartia, *Microstrip Lines and Slotlines, 2nd Edition*, Artech House, New York, NY, 1996.

[63] *Sonnet EM Suite*, Sonnet Software Inc., Liverpool, NY.

[64] J. B. Rizk, *W-Band RF-MEMS Switches, Phase Shifters and Antennas*, Ph.D. thesis, University of Michigan, Ann Arbor, MI, USA, Ann Arbor, MI.

[65] G. L. Tan, *High-Performance RF MEMS Circuits and Phase Shifters*, Ph.D. thesis, University of Michigan, Ann Arbor, MI.

[66] G. L. and Matthaei, "Narrow-band, fixed-tuned and tunable band-pass filters with zig-zag, hairpin-comb resonators," *IEEE Trans. Microwave Theory Tech.*, vol. 51, pp. 1214–1219, April 2003.

[67] J. S. Hayden and G. M. Rebeiz, "Very low-loss distributed X-band and Ka-band MEMS phase shifters using metal-air-metal capacitors," *IEEE Trans. Microwave Theory Tech.*, vol. 51, pp. 309–314, Jan. 2003.

[68] J. K. A. Everard and K. K. M. Cheng, "High performance direct coupled bandpass filters on coplanar waveguide," *IEEE Trans. Microwave Theory Tech.*, vol. 41, pp. 1568–1573, Sept. 1993.

[69] L. Dussopt and G. M. Rebeiz, "High-Q millimeter-wave MEMS varactors: Extended tuning range and discrete-position designs," in *2002 IEEE MTT-S Int. Microwave Symp. Dig.*, Seattle, WA, June 2002, pp. 1205–1208.

[70] L. Dussopt and G. M. Rebeiz, "Intermodulation distortion and power handling in RF MEMS switches, varactors and tunable filters," *IEEE Trans. Microwave Theory Tech.*, vol. 51, pp. 1247–1256, April 2003.

[71] B. A. Munk, *Frequency Selective Surfaces*, John Wiley and Sons, Hoboken, NJ, 2000.

[72] T. K. Wu, *Frequency Selective Surfaces and Grid Arrays*, John Wiley and Sons, New York, NY, 1995.

[73] C. J. Larson, "Modified center layer metallic bipolar radome design," *Tech. Rept. ASAL-TR-78-28, Ohio State Univ. Electro Science Lab., Rept. 4346-2*, March 1978.

[74] R. Pous and D. M. Pozar, "A frequency-selective surface using aperture couples microstrip patches," *IEEE Trans. Antennas and Propagation*, vol. 39, pp. 1763–1769, Dec. 1991.

[75] *High Frequency Structure Simulator (HFSS)*, Ansoft Corporation, Pittsburg, PA.

[76] A. Abbaspour-Tamijani, L. Dussopt, and G. M. Rebeiz, "Miniature and tunable filters using MEMS capacitors," *IEEE Trans. Microwave Theory Tech.*, vol. 51, pp. 1878–1885, July 2003.

[77] W. L. Stutzman, *Antenna Theory and Design, 2nd Edition*, John Wiley and Sons, Hoboken, NJ, 1997.

[78] A. D. Margomenos, *Three Dimensional Integration and Packaging Using Silicon Micromachining*, Ph.D. thesis, University of Michigan, Ann Arbor, MI.

[79] B. C. Deckman, *Active Quasi-Optics and Measurements*, Ph.D. thesis, California Institute of Technology, Pasadena, CA.

[80] N. Gagnon, J. Shaker, P. Berini, L. Roy, and A. Petosa, "Material characterization using a quasi-optical measurement system," *IEEE Trans. Instrumentation and Measurement*, vol. 52, pp. 333–336, April 2003.

[81] M. A. Ali, S. C. Ortiz, T. Ivanov, and A. Mortazawi, "Analysis and measurement of hard-horn feeds for the excitation of quasi-optical amplifiers," *IEEE Trans. Microwave Theory Tech.*, vol. 47, pp. 479–487, April 1999.

[82] S. C. Ortiz, J. Hubert, L. Mirth, E. Schlecht, and A. Mortazawi, "A high-power Ka-band quasi-optical amplifier array," *IEEE Trans. Microwave Theory Tech.*, vol. 50, pp. 487–497, Feb. 2002.

[83] G. F. Engen and C. A. Hoer, "Thru-reflect-line: an improved technique for calibrating the dual six-port automatic network analyzer," *IEEE Trans. Microwave Theory Tech.*, vol. 987-993, pp. 27, Dec. 1979.

[84] D. T. McGrath, "Planar three-dimentional constrained lens," *IEEE Trans. Antennas and Propagation*, vol. 34, pp. 46–50, Jan. 1986.

[85] D. M. Pozar, "Flat lens antenna concept using aperture coupled microstrip patches," *Electronic Letters*, vol. 32, pp. 2109–2111, Nov. 1996.

[86] B. E. A. Saleh and M. C. Teich, *Fundamentals of Photonis*, John Wiley and Sons, Hoboken, NJ, 1991.

[87] A. B. Yakovlev, S.Oritz, M. Ozkar, A. Mortazawi, and M. Steer, "A waveguide-based aperture-coupled patch amplifier array-full-wave system analysis and experimental validation," *IEEE Trans. Microwave Theory Tech.*, vol. 48, pp. 2692–2699, Dec. 2000.